UNIVERSITY OF CALIFORNIA,
IRVINE

Monte Carlo Simulations of Noise in Superconducting and Semiconducting Qubits

DISSERTATION

submitted in partial satisfaction of the requirements
for the degree of

DOCTOR OF PHILOSOPHY

in Physics

by

Daniel Louis Mickelsen

Dissertation Committee:
Professor Clare C. Yu, Chair
Professor Ruqian Wu
Professor Ilya Krivorotov

2023

TABLE OF CONTENTS

LIST OF FIGURES

LIST OF TABLES

ACKNOWLEDGMENTS

I would like to thank my advisor Clare Yu. Without her years of guidance, this work would not have been possible, and I am grateful for the opportunity I was given to perform this research. I appreciate the discussions with Hervé Carruzzo and his valuable contributions to this thesis. Without his help, large portions of chapter 3 would not exist. I would also like to thank Professor Susan Coppersmith for bringing up the problem of $1/f$ charge noise in semiconducting qubits and for the useful discussions that ensued.

This research has been funded by: the U.S. Department of Energy, Office of Science, Basic Energy Sciences, under Award DE-FG02-05ER46237, the National Science Foundation grant PHY-1607611, the National Science Foundation through the University of Wisconsin Materials Research Science and Engineering Center Grant DMR-1720415, Google Gift 2502, DOE-BES Grant DE-FG02-05ER46237, and the Eddleman Quantum Institute.

VITA

Daniel Louis Mickelsen

EDUCATION

Doctor of Philosophy in Physics **2023**
University of California, Irvine *Irvine, Californa*

Master of Science in Physics **2015**
San Diego State University *San Diego, California*

Bachelor of Science in Physics **2012**
University of Illinois at Chicago *Chicago, Illinois*

RESEARCH EXPERIENCE

Graduate Research Assistant **2016–2023**
University of California, Irvine *Irvine, California*

Graduate Research Assistant **2012–2015**
San Diego State University *San Diego, California*

Research Assistant **2010**
University of Illinois at Chicago *Chicago, Illinois*

TEACHING EXPERIENCE

Teaching Assistant **2015–2022**
University of California, Irvine *Irvine, California*

Teaching Assistant **2012–2013**
San Diego State University *San Diego, California*

ABSTRACT OF THE DISSERTATION

Monte Carlo Simulations of Noise in Superconducting and Semiconducting Qubits

By

Daniel Louis Mickelsen

Doctor of Philosophy in Physics

University of California, Irvine, 2023

Professor Clare C. Yu, Chair

Superconducting quantum interference devices (SQUIDs) show great promise as quantum bits (qubits) but continue to be hindered by flux noise. The flux noise power spectra of SQUIDs go as $1/f^{\alpha}$, where α is the temperature-dependent noise exponent. Experiments find $0.5 \lesssim \alpha \lesssim 1$. Furthermore, experiments find that the noise power spectra versus frequency at different temperatures pivot about or cross at a common point which is different for each SQUID. To try to better understand the results and motivated by experimental evidence that magnetic moments on the surface of SQUIDs produce flux noise, we have carried out and here present the results of Monte Carlo simulations of various spin systems on 2D lattices. We find that only spin glasses produce $\alpha \sim 1$ at low temperature. We find that aliasing of the noise power spectra at high frequencies can lead to spectral pivoting if the knee is in proximity to a knee at a slightly lower frequency. We show that the pivot frequency depends on how often the magnetization is recorded and the method of how lattice sites are selected for orientation: choosing every site once or choosing sites at random. The spectral pivoting that occurs in our simulations is due to aliasing and does not explain the spectral pivoting of experiments.

Silicon quantum dot qubits show great promise but suffer from charge noise with a $1/f^{\alpha}$ spectrum, where f is frequency and $\alpha \lesssim 1$. It has recently been proposed that $1/f^{\alpha}$ noise spectra

can emerge from a few thermally activated two-level fluctuators in the presence of sub-bath temperature fluctuations associated with a two-dimensional electron gas (2DEG) [2]. We investigate this proposal by doing Monte Carlo simulations. In one set of simulations, we model a two-level fluctuator as an anisotropic Heisenberg spin with a barrier to spin re-orientations in a bath with a fluctuating temperature. In another set of simulations, the two-level fluctuator is a single Ising spin in a bath with a fluctuating temperature. We find that to obtain noise with a $1/f^{\alpha}$ spectrum with $\alpha \lesssim 1$ down to low frequencies, the duration of temperature fluctuations must be comparable to the inverse of the lowest frequency at which the noise is measured. This result is consistent with an analytic calculation in which the fluctuator is a two-state system with dynamics governed by time-dependent switching rates. In this case we find that the noise spectrum follows a Lorentzian at frequencies lower than the inverse of the average duration of the lowest switching rate. We then estimate relaxation times of thermal fluctuations by considering thermal diffusion in an electron gas in a confined geometry. We conclude that temperature fluctuations in a 2DEG sub-bath would require an unphysically long duration to be consistent with experimental measurements of $1/f$-like charge noise in quantum dots at frequencies extending well below 1 Hz.

Charge noise in quantum dots has been observed to have a $1/f$ spectrum. We propose a model in which a pair of quantum dots are coupled to a 2D bath of fluctuators that have electric dipole moments and that interact with each other, i.e., with the other fluctuators. These interactions are primarily via the elastic strain field. We use 2D nearest-neighbor Ising spin glass to represent these elastic interactions and to simulate the dynamics of the bath of electric dipole fluctuators in the presence of a ground plane representing metal gates above the oxide layer containing the fluctuators. We calculate the resulting fluctuations in the electric potential at the two quantum dots that lie below the oxide layer. We find that $1/f$ electric potential noise spectra at the quantum dots and cross correlation in the noise between the two quantum dots are in qualitative agreement with experiment.

Chapter 1

Introduction and Overview

Quantum computing has become the focus of much attention due to its potential applications. Quantum computers can be used for integer factorization for breaking RSA encryption (a common cryptographic protocol used for secure communication between two parties) [3, 4], secure communication through quantum key distribution [3, 5], simulation of quantum systems [4, 5], weather prediction [6], finance [7], and increasing the speed of machine learning problems [8, 9]. Quantum computers store information differently from classical computers. In a classical computer, the most basic unit of information is a bit which is represented as a 0 or a 1. In a quantum computer, a quantum bit (qubit) is in a linear combination of the two quantum states $|0\rangle$ and $|1\rangle$ [3]. Classical computers use multiple bits to store information. A quantum computer uses qubits that are entangled with each other [5]. The basis states $|0\rangle$ and $|1\rangle$ of a quantum bit are dependent on the physical implementation of the qubit.

Superconducting qubits (SQUIDs) have been suggested as a leading candidate to be used as physical qubits [10]. SQUIDs are superconductors that have one, two, or three Josephson junctions. At sufficiently low temperatures, electrons in superconductors form Cooper pairs of electrons [10, 11]. In SQUIDs, Cooper pairs tunnel between two superconductors separated

by a weak barrier called a Josephson junction. Another phenomenon of superconductors is that the flux through a superconducting ring is quantized. The macroscopic wavefunction is single valued, which means that the phase of the wavefunction must be an integer multiple of 2π. The phase is affected by an external magnetic field, so a circulating supercurrent develops in the superconductor to satisfy the flux quantization condition [12].

Of the superconducting qubits, the main types are flux, charge, and phase. Flux qubits are made of a superconducting loop with one or three Josephson junctions. The two basis quantum states are the up and down magnetic flux states determined by the direction of the circulating supercurrent [10, 13, 14]. In charge qubits, a small superconducting island holds Cooper pairs, and the quantum states are the number of Cooper pairs n or $n + 1$ [10, 15]. Phase qubits are made using a single Josephson junction. An anharmonic potential barrier is created by the Josephson junction and the tilt of the potential is caused by the current bias. The two quantum states used are the ground state and the first excited state of a potential well of the Josephson junction potential [10, 16].

Another good candidate for physical qubits is semiconducting quantum dots [17]. Semiconducting qubits can be made using a Si/SiGe heterostructure with electrons confined within a tiny portion of a two-dimensional electron gas (2DEG) and are manipulated using electrostatic gates [18–20]. The single-electron quantum dot uses the spin states of electrons as the two quantum states [17]. The quantum states in two-electron double dots are the singlet and triplet electron spin states [21].

Obstacles to achieving practical quantum computers are noise [22] and decoherence [7, 19]. Superconducting qubits and semiconducting qubits are made of different materials, and are expected have differing dominant microscopic sources of noise. Decoherence is the loss of quantum information to the environment which poses a problem in performing calculations with quantum computers. Although there are methods of quantum error correction that can counteract decoherence [5, 7], it is useful to understand the causes so that decoherence can

be prevented.

$1/f$ noise is characterized by noise power spectra that go as $1/f^{\alpha}$, where f is frequency and α is the noise exponent. For superconducting qubits, $1/f$ flux noise [10, 22] is a major cause of decoherence. Flux noise is caused by fluctuating magnetic moments on superconducting surfaces [23, 24]. The Dutta-Horn model is typically used in explaining $1/f$ noise. The model assumes that independent, thermally-activated processes that produce Lorentzian power spectra can lead to $1/f$ noise with a flat distribution of barrier heights. For spins, barriers may come from interactions between spins or spin anisotropy.

Charge noise is a dominant source of noise in semiconducting qubits [2, 18, 20]. If the quantum dots in these qubits are coupled to a bath of two-level fluctuators that have electric dipoles, then the resulting fluctuations can produce $1/f$ noise. Ahn *et al.* [2] put forward the idea that a small number of two-level fluctuators coupled to a quantum dot are affected by thermal fluctuations in a small region of the thermal bath [2]. Temperature fluctuations of the sub-bath produces the same results as having different barrier heights in the Dutta-Horn model of noise, leading to $1/f^{\alpha}$ charge noise.

In both superconducting qubits and semiconductor quantum dot qubits, our approach to modeling the noise sources is similar. We model these noise sources through Monte Carlo simulations of classical spins that obey detailed balance. In this thesis, we investigate spectral pivoting of the power spectra and discuss which interactions lead to noise exponents $\alpha \sim 1$ using our Monte Carlo simulations of magnetic noise in superconducting qubits in chapter 2. Spectral pivoting is where the noise power spectra at different temperatures cross at a common point. This was observed in experiment by Anton *et al.* [1]. The flux noise power spectra of a SQUID at 11 temperatures is shown in Fig. 1.1. Our simulations of noise are of magnetic moments of molecular oxygen adsorbed on the Al_2O_3 surface of a SQUID [25, 26]. Models with different nearest-neighbor exchange couplings and cases of spin anisotropy are considered. Next, in chapter 3, we discuss charge noise in quantum dot qubits

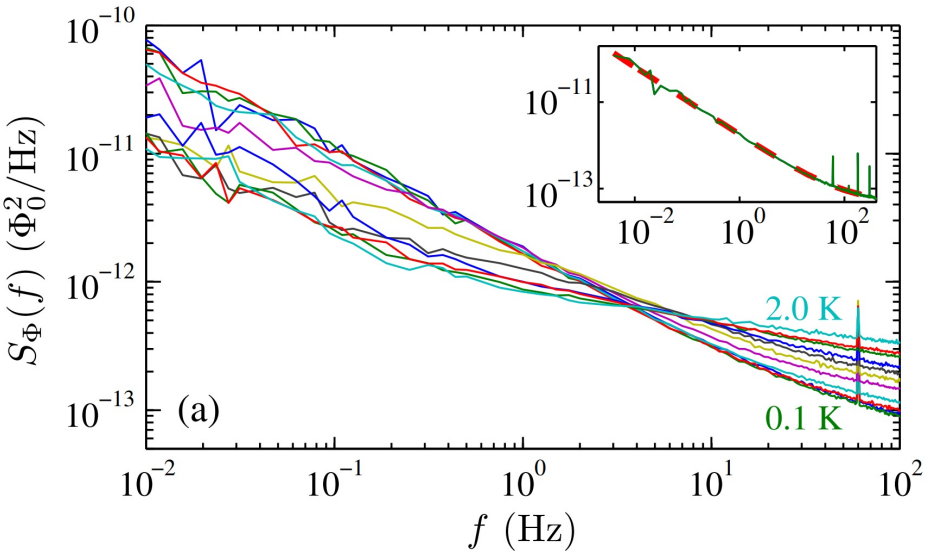

Figure 1.1: Flux noise power versus frequency of a SQUID at 11 temperatures as measured by Anton *et al.* [1].

due to temperature fluctuations [2]. We represent the single two-level fluctuator that is coupled to a quantum dot as either a Heisenberg spin or an Ising spin. The spin is subjected to temperature fluctuations, and the results are used do determine the validity of a model of $1/f$ charge noise that is due to temperature fluctuations. We later discuss our model of interacting two-level systems as a source of $1/f$ noise in semiconductor quantum dot qubits in chapter 4. We simulate two-level fluctuators in a 2D lattice with each fluctuator having an elastic and electric dipole. The dipoles interact elastically and fluctuate causing fluctuations in the electric dipoles. The electric dipoles and their image dipoles in the metal gates of the qubit produce a fluctuating dipole potential at the quantum dots resulting in $1/f$ charge noise.

Chapter 2

Monte Carlo Simulations of Magnetic Noise

2.1 Introduction

Superconducting quantum interference devices (SQUIDs) can be used as quantum bits (qubits). While SQUIDs hold great potential for quantum computing, they suffer from noise and decoherence. One of the main sources of decoherence is $1/f$ flux noise [22]. $1/f$ noise is characterized by noise power spectra that go as $1/f^{\alpha}$, where f is frequency and α is the noise exponent. The noise exponents for SQUIDs lie in the range $0.5 \lesssim \alpha \lesssim 1$ for $1\text{ K} \gtrsim T \gtrsim 20\text{ mK}$ [1, 23, 27], where the noise exponent increases as temperature decreases. Fluctuating magnetic moments were proposed as a source of flux noise in SQUIDs [23]. This is consistent with experimental evidence of surface spins on normal metals [28] and superconductors [24]. Sendelbach *et al.* measured a $1/T$ temperature-dependent flux through SQUIDs which is indicative of paramagnetic spins [24]. Fluctuations of these surface spins cause flux noise because SQUIDs are highly sensitive magnetometers.

Additional evidence for surface spins comes from density functional theory (DFT) calculations of the oxide layer on the aluminum surface of SQUIDs. Since SQUIDs are exposed to air, it is reasonable to expect oxygen to be adsorbed on the surface below approximately 40 K. O_2 is paramagnetic, and DFT calculations show that oxygen retains a magnetic moment of 1.8 μ_B after being adsorbed on the surface of sapphire (α-Al_2O_3) [25]. DFT also finds a low barrier ($\sim$ 10 mK) for spin reorientation so that spins rotate easily in the easy plane that is perpendicular to the O_2 molecular bond [25, 26]. In addition, these calculations indicate that the coupling between adsorbed oxygen molecules is ferromagnetic [25]. Monte Carlo simulations of ferromagnetically coupled O_2 on the surface of sapphire are able to produce $1/f$ noise consistent with experiment at higher temperatures [25]. Evidence of paramagnetic oxygen spins on SQUIDs come from X-ray absorption spectroscopy (XAS) and x-ray magnetic circular dichroism (XMCD) experiments that were carried out on thin films of aluminum and niobium which are typical SQUID materials [26]. The experiments [26] confirm the DFT predictions [25] that the bond axis of O_2 is tilted 55° away from the surface normal.

Surface treatments that remove or prevent oxygen adsorption on SQUIDs reduce flux noise by a factor of four or five [26]. A protective coating of nonmagnetic ammonia (NH_3) prevents the adsorption of O_2 since NH_3 has a higher binding energy to Al_2O_3. Ultraviolet irradiation of SQUIDs in an ultrahigh vacuum removes adsorbed oxygen [26]. Although flux noise is reduced with these treatments, it is not eliminated.

There is still the question as to how surface spins produce $1/f$ noise. The Dutta-Horn model of $1/f$ noise [29] is the most common explanation for $1/f$-type noise. The model assumes that independent, thermally-activated processes exist, where each process individually produces a Lorentzian power spectra. A distribution of barrier heights that is slowly varying on the order of k_BT leads to $1/f$ noise. In the case of spins, the barriers can come from interactions between spins or spin anisotropy. Theoretical models of interacting spins on the surface of

SQUIDs were indeed able to produce $1/f$ flux noise [30–32].

While it is well established that surface spins are a source of $1/f$ flux noise, there are still mysteries associated with this noise. For example, why is the noise exponent close to 1? While Ising spin glass models yield $\alpha \lesssim 1$ [32], ferromagnetic spin system simulations find $\alpha > 1$ at low temperatures [25].

Another puzzle comes from experiments using Nb SQUIDs where the noise power spectra as a function of frequency at different temperatures pivot or cross in the vicinity of a single "pivot" frequency [1]. For SQUIDs with different geometries, the power spectra for each device still pivoted. The pivot frequency was different for each SQUID, and there was no clear relation between geometry and pivot frequency. Other experiments involving SQUIDs of various materials also found spectral pivoting [27].

Several models have been proposed to explain spectral pivoting. Spin diffusion can explain pivoting if the system is close to a phase transition where the diffusion coefficient is dependent on temperature [33]. The result is a range of frequencies where power spectra cross as in experiment. Monte Carlo simulations of Heisenberg spins in a cluster model can also produce spectral pivoting [34]. This model bases the probability of spin flips on changes in free energy instead of internal energy as in the standard Monte Carlo method. This has the effect that lower entropy spin configurations are more favored. This model produces $1/f^\alpha$ power spectra at low frequency and $1/f^2$ power spectra at high frequency. The power spectra do not intrinsically pivot. To get crossing, the $1/f^\alpha$ parts of the power spectra are extended via extrapolation into the high-frequency range.

In an effort to understand spectral pivoting and what types of interactions lead to the noise exponent $\alpha \sim 1$, we performed Monte Carlo simulations of spins on 2D lattices since both DFT simulations [25] and experiments [26] indicate spins can produce flux noise. Since oxygen spins have an easy-plane anisotropy perpendicular to the O_2 bond [25], we test

various interacting spin models with different anisotropies.

Although we find that spectral pivoting can occur in Monte Carlo simulations of classical XY and Heisenberg spins, the pivoting in our simulations is an artifact of the simulations. In plots of noise power versus frequency, a high frequency pivot occurs because the low-frequency knees are close in frequency to the high-frequency aliasing of the power spectra, and thus the simulations do not explain the experimentally observed pivoting.

In addition to trying to better understand spectral pivoting, we also use this work to explain some of the challenges and pitfalls of Monte Carlo simulations and what happens when there are deviations from the standard procedure. The chapter is structured in the following manner. In Sec. 2.2, we describe the Hamiltonians of the spin models, how the simulations are performed/equilibrated, and how the noise power is analyzed. In Sec. 2.3, we present our results on noise exponents, noise amplitudes, and why pivoting occurs in our simulations.

2.2 Method

2.2.1 Spin Models

The Ising, XY, and Heisenberg Hamiltonians of the 2D spin systems are given by

$$H_{\text{Ising}} = -\sum_{\langle i,j \rangle} J_{ij} s_i \cdot s_j \tag{2.1}$$

$$H_{\text{XY}} = -\sum_{\langle i,j \rangle} J_{ij} \mathbf{s}_i \cdot \mathbf{s}_j \tag{2.2}$$

$$H_{\text{Heis.}} = -\sum_{\langle i,j \rangle} J_{ij} \mathbf{s}_i \cdot \mathbf{s}_j - A \sum_i (\mathbf{n}_i \cdot \mathbf{s}_i)^2, \tag{2.3}$$

where $\mathbf{s}_i$ and $\mathbf{s}_j$ are classical spins of length 1 on nearest-neighbor sites i and j, respectively. J_{ij} is the spin exchange coupling. A positive value for J_{ij} indicates a ferromagnetic interaction. The second term in Eq. (3.1) is a spin anisotropy term. For each site i, there is a local anisotropy axis $\mathbf{n}_i$. To model the disorder of the SQUID surface, $\mathbf{n}_i$ points in a direction that varies randomly from site to site. The random-axis anisotropic model was proposed by Harris to describe magnetism in an amorphous material [35].

If the anisotropy A is positive, then $\mathbf{n}_i$ is the easy axis for spins; if the anisotropy A is negative, then $\mathbf{n}_i$ is normal to the easy plane for spin orientation.

Six spin model interactions were simulated: noninteracting spins ($J_{ij} = 0$), ferromagnet ($J_{ij} = 1$), Poisson ferromagnet ($\langle J_{ij} \rangle = 1$, $\sigma^2_{J_{ij}} = 0.2$), antiferromagnet ($J_{ij} = -1$), spin glass ($\langle J_{ij} \rangle = 0, \sigma_{J_{ij}} = 1$), and spin glass ferromagnet ($\langle J_{ij} \rangle = 0.5, \sigma_{J_{ij}} = 1$). For the Poisson ferromagnet, the couplings J_{ij} are chosen in the following way [25]. First random integers C_{ij} are drawn from a Poisson distribution with a mean of 5. Then the couplings are given by J_{ij} = 0.2 C_{ij} so that for the Poisson ferromagnet, $\langle J_{ij} \rangle = 1$ and $\sigma^2_{J_{ij}} = 0.2$. The temperature for this system is measured in units of $\langle J_{ij} \rangle$. For the spin glass and spin glass ferromagnet, J_{ij} is chosen from a Gaussian distribution with a variance $\sigma^2_{J_{ij}}$ and the temperature is measured in units of $\sigma_{J_{ij}}$. The interactions and the corresponding simulated spin models are summarized in Table 2.1.

Interaction	Spin Models
Noninteracting $J_{ij} = 0$	Heisenberg, $A = -1$
Spin Glass $\langle J_{ij} \rangle = 0$, $\sigma_{J_{ij}} = 1$	Heisenberg, $A = 0$ Heisenberg, $A = -10$ XY Ising
Antiferromagnet $J_{ij} = -1$	Heisenberg, $A = 0$ Heisenberg, $A = -10$ XY
Poisson Ferromagnet $\langle J_{ij} \rangle = 1$, $\sigma^2_{J_{ij}} = 0.2$	Heisenberg, $A = 0$ Heisenberg, $A = -10$ XY
Ferromagnet $J_{ij} = 1$	Heisenberg, $A = 0$ Heisenberg, $A = -10$ XY
Spin Glass Ferromagnet $\langle J_{ij} \rangle = 0.5$, $\sigma_{J_{ij}} = 1$	Heisenberg, $A = 0$ Heisenberg, $A = -10$ XY

Table 2.1: All six types of spin exchange couplings J_{ij} and the corresponding spins models that were simulated.

2.2.2 Simulation Details

We perform simulations with spins occupying every site of a 16 x 16 square lattice. The system is initialized with randomly oriented spins. For anisotropic systems, each run has a unique, but random, set of anisotropic axes. A spin is allowed to reorient itself according to the Metropolis algorithm [36]. In this algorithm, a trial move consists of first choosing a spin on the lattice at random. The initial energy of this site E_i is calculated from the local field produced by its nearest neighbors and the local anisotropy. A new orientation of the spin is chosen from a random distribution for the Heisenberg and XY systems. For the Heisenberg systems, the distribution is random on the unit sphere (the distribution is uniform in ϕ and $\cos\theta$). For XY systems, the distribution is random on the unit circle (uniform distribution in ϕ). In the case of Ising systems, the spin is flipped. The final energy E_f of this site with the new spin orientation is calculated. If the final energy is less than the initial energy, then the new spin orientation is accepted. However if the final energy is greater than the initial energy, then the flip is accepted with probability $\exp[-(E_f - E_i)/(k_B T)]$. A random number is generated from a uniform distribution between 0 and 1; if it is less than the Boltzmann factor, then the new orientation is accepted. This process continues for the remaining sites within the lattice. The time it takes for one sweep through the lattice is one Monte Carlo step (MCS).

The system is equilibrated as described in Appendix B.1.2. After equilibration, the total magnetic moment of the lattice is recorded at every Monte Carlo step. The system is cooled from its initial random spin configuration at $T = 10$ to $T = 0.5$.

2.2.3 Site Selection

For every sweep through the lattice of N spins, N spins are offered the chance for reorientation, but only M spins are at different sites. There are two typical methods of selecting

sites.

The "every-site method" involves giving each site in the lattice one opportunity to reorient, i.e., $M = N$. This is the method used in this work. In the "random-site method," M sites are chosen for reorientation at random. With this method, it is possible to select several sites more than once and some not at all.

We would expect simulations of magnetic noise to produce white noise power spectra at high temperatures. For the "every-site method," this is true. The power spectrum of Heisenberg spins in the high-temperature limit using the "random-site method" goes as $1/f$, and the $1/f$ noise power spectra is entirely due to the site selection method. For a given model, the power spectra at different temperatures with the "random-site method" pivot at a lower frequency compared to the "every-site method."

2.2.4 Time Steps

One time step in a standard Monte Carlo simulation is one Monte Carlo step (MCS). To simulate a slower recording rate, the total magnetic moment time series can be recorded after several MCS. A comparison of recording every time step and every 10 time steps is shown in Fig. 2.1. Although the maximum frequency of the power spectra when recording every 10 time steps is smaller than for recording every time step, the total noise power for both cases is equal. At a given temperature, the total noise power is equal to the variance of the total magnetic moment time series which is dimensionless. This means that the noise power $S_x(f)$ has units of MCS. It is also possible to record the time series more often than one MCS. In this case, the total magnetic moment would be recorded before all spins are given an opportunity to reorient. The resulting noise spectra would extend to frequencies higher than 0.5 MCS^{-1}. Recording every 10 time steps causes the aliasing to occur at a lower frequency, but the location of the low-frequency knee remains unchanged. The effect is that

the pivoting frequency is decreased. Unless otherwise noted, the time steps are recorded at 1 MCS intervals.

2.2.5 Noise Power

The time series of each component of the total magnetic moment is given by $m_a(t_j)$, where $a = x, y, z$. The deviation from the average is $\delta m_a(t_j) = m_a(t_j) - \overline{m_a(t_j)}$. The noise power spectral density can be determined from the Fourier transform of the autocorrelation function of the time series. The autocorrelation is given by

$$C_a(t_k) = \frac{1}{N_\tau} \sum_{j=0}^{N_\tau - 1} \delta m_a(t_j) \delta m_a^*(t_j - t_k), \tag{2.4}$$

where $\delta m_a^*(t_j - t_k)$ is the complex conjugate of $\delta m_a(t_j - t_k)$. For a discrete time series $m_a(t_j)$ of length N_τ, the discrete inverse Fourier transform is given by

$$\delta m_a(t_j) = \frac{1}{N_\tau} \sum_{k=0}^{N_\tau - 1} \tilde{m}_a(f_k) e^{2\pi i f_k t_j / N_\tau}, \tag{2.5}$$

where $\tilde{m}_a(f_k)$ is the Fourier transform of the time series. Using Eq. (3.3), the autocorrelation function becomes

$$C_a(t_k) = \frac{1}{N_\tau^3} \sum_{j=0}^{N_\tau - 1} \left[\left(\sum_{l=0}^{N_\tau - 1} \tilde{m}_a(f_l) e^{2\pi i f_l t_j / N_\tau} \right) \times \left(\sum_{n=0}^{N_\tau - 1} \tilde{m}_a^*(f_n) e^{-2\pi i f_n (t_j - t_k)/N_\tau} \right) \right]. \tag{2.6}$$

This can be simplified to

$$C_a(t_k) = \frac{1}{N_\tau^2} \sum_{n=0}^{N_\tau - 1} |\tilde{m}_a(f_n)|^2 e^{2\pi i f_n t_k / N_\tau}. \tag{2.7}$$

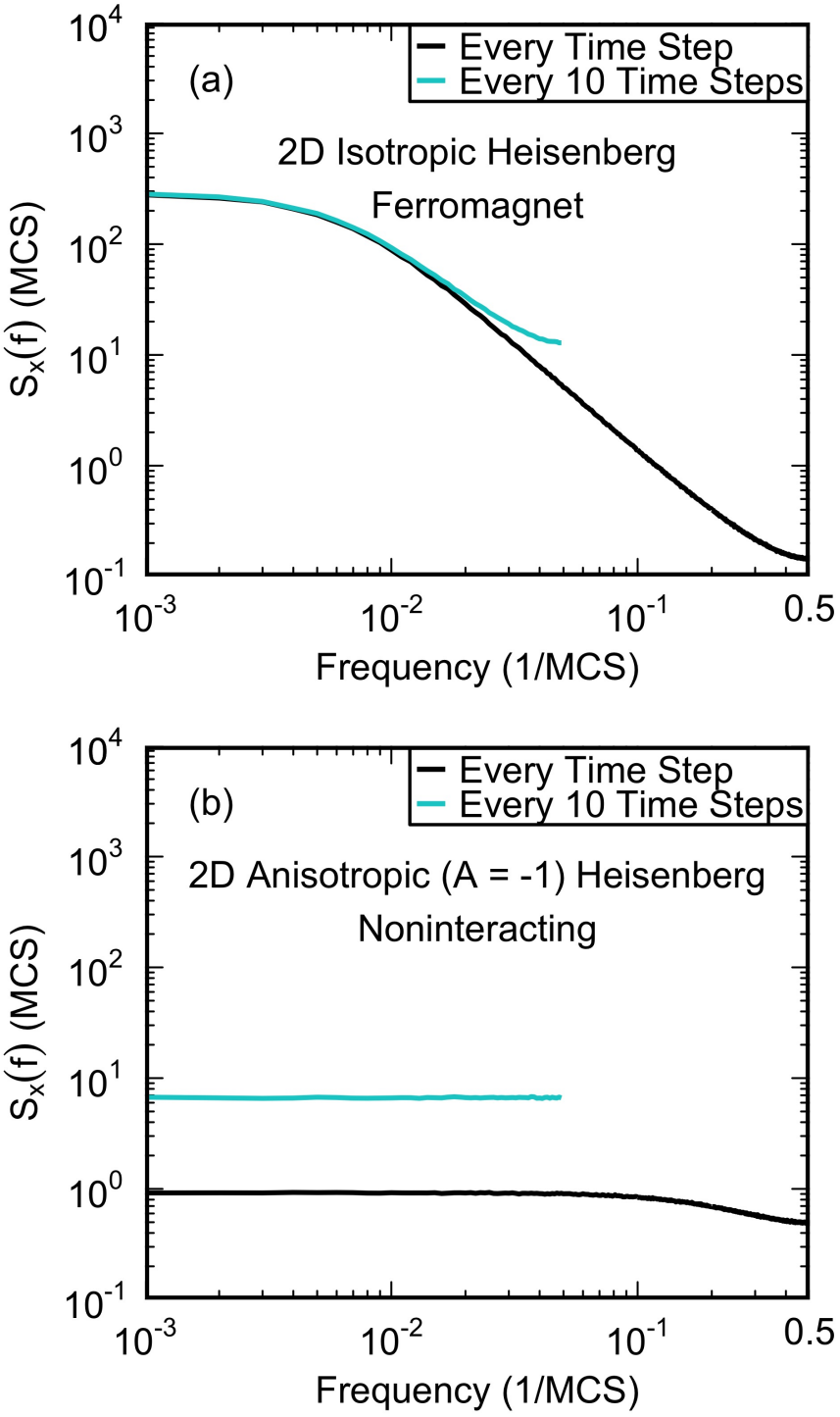

Figure 2.1: Noise power $S_x(f)$ of the x-component of the total magnetic moment versus frequency. Noise power spectra averaged over 10 segments for the 2D (a) isotropic ($A = 0$) Heisenberg ferromagnet ($J_{ij} = 1$) and (b) noninteracting ($J_{ij} = 0$), anisotropic ($A = -1$) Heisenberg models from recording the total magnetic moment at every time step and every ten time steps at $T = 1$. The units of noise power are MCS, because the total noise power is dimensionless.

Taking the Fourier transform of Eq. (3.5) gives the periodogram estimate [37] for computing the noise power $S_a(f_k)$ for the axes $a = x, y, z$:

$$S_a(f_k) = \frac{1}{N_\tau}\frac{1}{N}|\tilde{m}_a(f_k)|^2, \tag{2.8}$$

where the power spectra is divided by N so that $S_a(f_k)$ is the noise power per site for spin component a. The power spectra are normalized so that at a given temperature, the total noise power is equal to the variance of the total magnetic moment time series divided by the number of sites.

The Fourier transform $\tilde{m}_a(f_k)$ is computed using the C subroutine library FFTW [38]. At a given temperature, the time series $\delta m_a(t_j)$ for a given run is split into either 10 or 100 segments (blocks) of equal length. The power spectrum is found for each segment and is averaged over these segments to give a smoother power spectrum. At each temperature, the spectra are averaged over 200 independent runs. The power spectra used in all plots shown in this chapter are averaged over 100 segments.

2.3 Results

2.3.1 Low-Frequency Knee

At lower frequencies of the power spectra, there are "knees" where the power spectra transition from A^2/f^α to white noise at low frequency as shown in Fig. 2.2. The frequency of the knee decreases as the temperature decreases.

The low-frequency knee is due to finite size effects of the lattice [39]. The correlation length increases as the temperature approaches the transition temperature T_c associated with the relevant order parameter. The relaxation time increases as the correlation length increases,

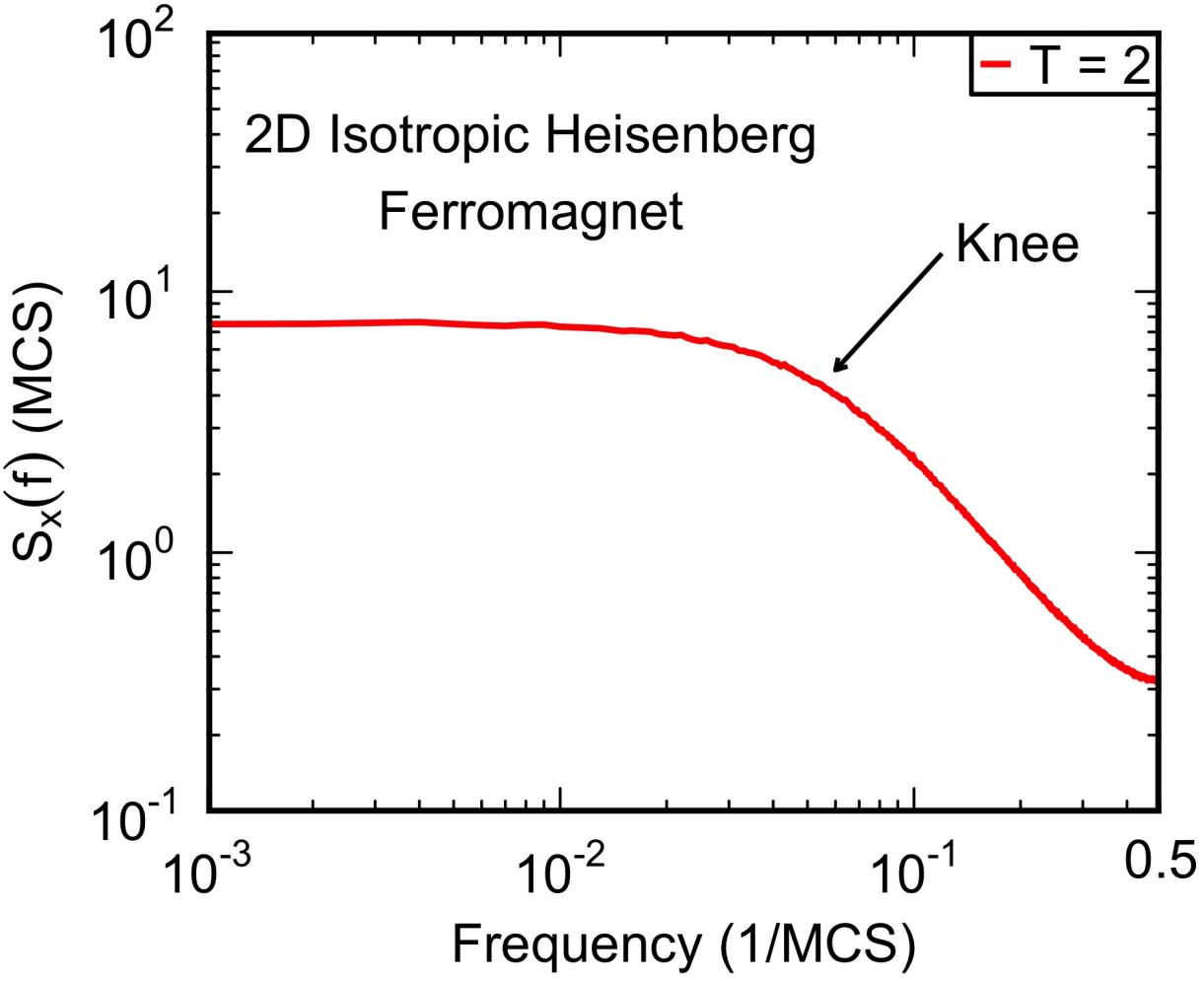

Figure 2.2: Noise power $S_x(f)$ of the x-component of the total magnetic moment of a 2D isotropic ($A = 0$) Heisenberg ferromagnet (J_{ij}=1) versus frequency. The low-frequency knee of the power spectrum averaged over 100 segments is shown for $T = 2$.

so the system takes longer to equilibrate. In previous simulations of the ferromagnetic Ising model and 5-state Potts model, it was found that the knee frequency is proportional to the system's relaxation rate τ^{-1} [39]. This means that as the temperature decreases and approaches T_c, the knee frequency decreases. Since the relaxation time increases with system size, we expect the knee frequency to decrease with system size [39]. One should look at the noise in the relevant order parameter to see the knee frequency decrease. The order parameters are magnetization for the ferromagnetic systems, staggered magnetization for the antiferromagnetic systems, and the spin glass order parameter q for spin glass systems. We investigate this below.

According to the Mermin-Wagner-Hohenberg theorem [40, 41], two-dimensional Heisenberg spin systems should not undergo a phase transition. The order parameters of the ferromagnet, antiferromagnet, and spin glass systems show that Heisenberg systems exhibit ordering at a positive T_c. This discrepancy is because the Mermin-Wagner-Hohenberg theorem holds in the thermodynamic limit, while these simulations are for finite lattices. Simulations show that as the system size increases, the value of T_c decreases toward zero. This system size dependence is shown in Fig. 2.3. As the system size increases, the peaks in the magnetic susceptibility occur at lower temperatures.

2.3.2 Aliasing

At higher frequencies near 0.5 MCS^{-1}, there is an upturn of the noise power due to aliasing that is shown in Fig. 2.4. The aliasing is due to the periodicity of the factor $e^{-2\pi ift}$ used in the Fourier transform [37]. When calculating the discrete Fourier transform, frequency components of the power spectra that are greater than 0.5 MCS^{-1} are translated into the range 0 $\text{MCS}^{-1} < f < 0.5$ MCS^{-1} [37]. As we explain later in this section, under certain conditions, this aliasing can cause spectral pivoting where the power spectra at different

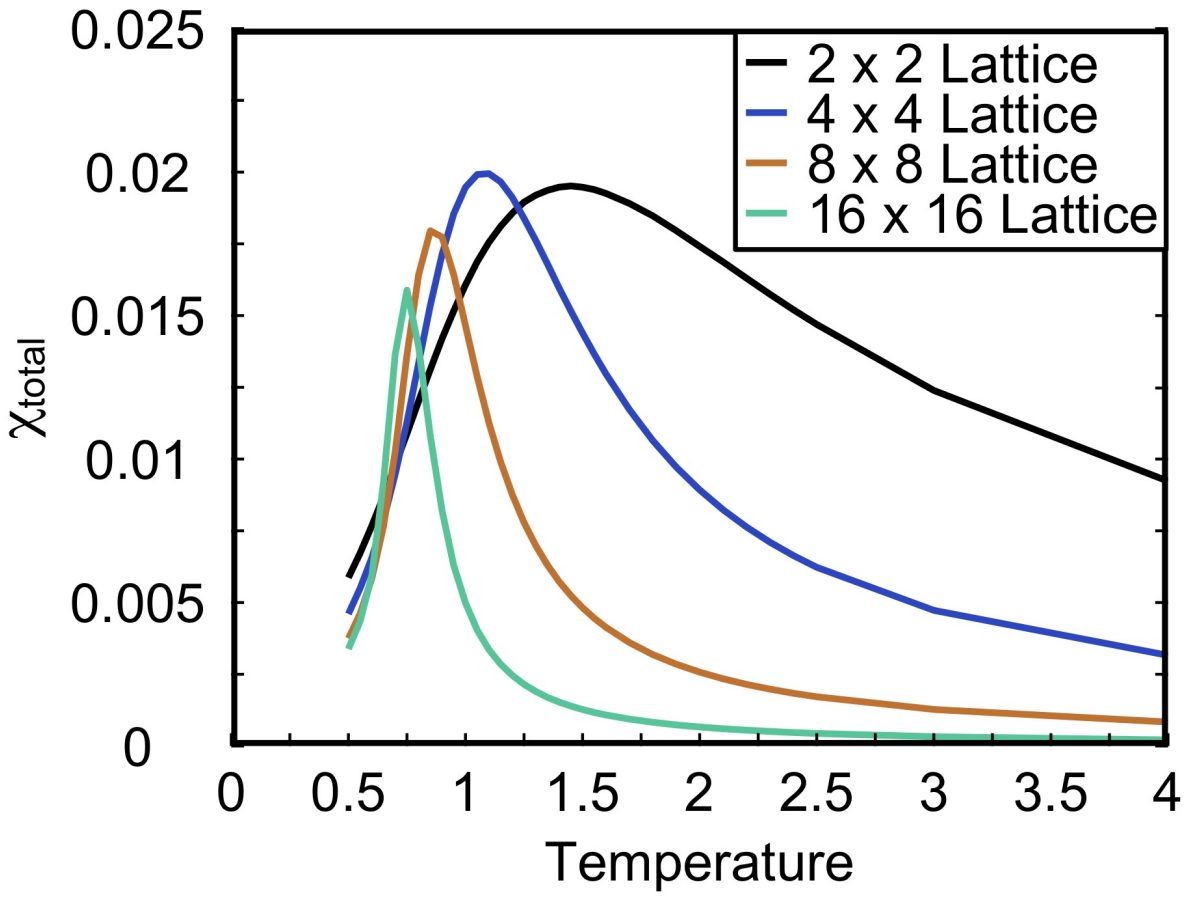

Figure 2.3: Magnetic susceptibility of the total magnetic moment per site versus temperature for the 2D Heisenberg Ferromagnet as a function of system size.

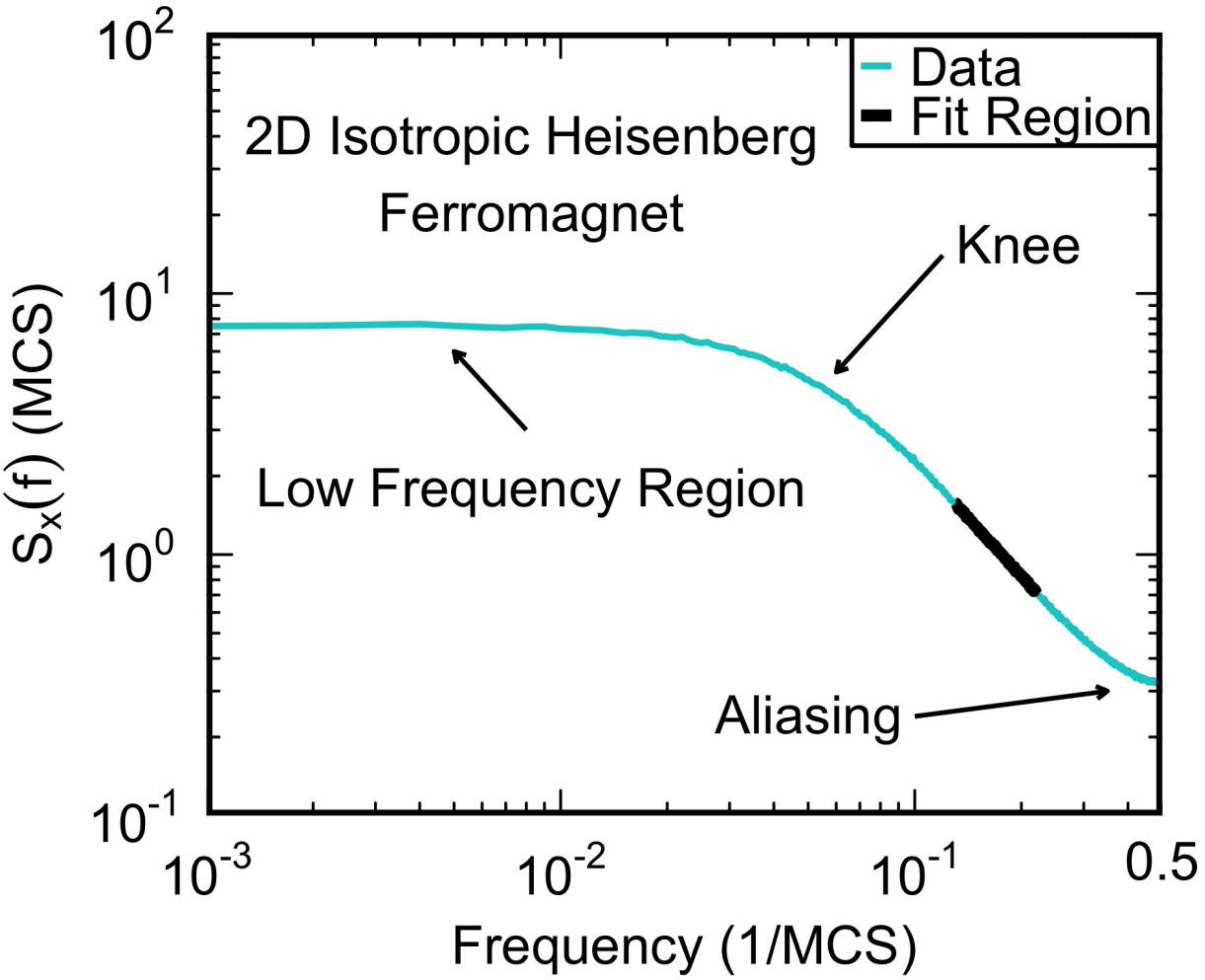

Figure 2.4: Noise power $S_x(f)$ of the x-component of the total magnetic moment of a 2D isotropic ($A = 0$) Heisenberg ferromagnet (J_{ij}=1) versus frequency. Labeled regions of the power spectrum averaged over 100 segments at $T = 2$.

temperatures cross within a narrow range of frequency.

2.3.3 Noise Exponents

To determine the noise amplitude (A^2) and the noise exponent (α), the function A^2/f^α is fit to the region of the power spectra that is linear on a log-log plot and that lies between the low-frequency knee and high-frequency upturn due to aliasing as shown in Fig. 2.4. More

details about this fitting process can be found in Appendix A.1. In performing fits, A^2/f^α is fit to the 10-averaged power spectra, so the fits are linear on log-log plots. Each x, y, and z component of the spin results in a power spectrum, and the amplitudes and exponents are determined for each component. The noise amplitudes and exponents as a function of temperature are shown in Figs. 2.5 and 2.6, respectively. In Fig. 2.6, the shaded region indicates the experimental range of noise exponents where $0.5 \leq \alpha \leq 1$ and $1 \leq T \leq 2$. (The lower bound of $T \geq 1$ is set by the energy scale of the exchange constant J_{ij}.) From the plot of noise exponents, we can see that the spin glass systems are the most consistent with experiment.

2.3.4 Pivoting

If the knee and aliasing upturn are close in frequency, then the two regions around these features overlap, and the frequency range of the power law fit is reduced. This effect is shown in Fig. 2.7 for the isotropic Heisenberg ferromagnet at $T = 10$.

Another effect of the aliasing upturn being close to the knee is that the power spectra at different temperature pivot about a common frequency as seen in Figs. 2.8 and 2.9. In Fig. 2.8, the noise power as a function of frequency is shown for different temperatures for the isotropic ferromagnetic, isotropic antiferromagnetic, isotropic spin glass, and noninteracting anisotropic ($A = -1$) Heisenberg spin models. Since the power spectra for the antiferromagnetic spin system do not cross at a common frequency, they do not pivot. The power spectra for the isotropic ferromagnetic, isotropic spin glass, and noninteracting, anisotropic ($A = -1$) systems pivot at high temperature. To examine this further, in Fig. 2.9, the noise power as a function of frequency is shown for the Heisenberg ferromagnet for $0.5 \leq T \leq 10$. Over this large range of temperature, the power spectra does not pivot. The inset of Fig. 2.9 shows pivoting for the high-temperature range $4 \leq T \leq 10$. Fig. 2.10 shows the pivoting

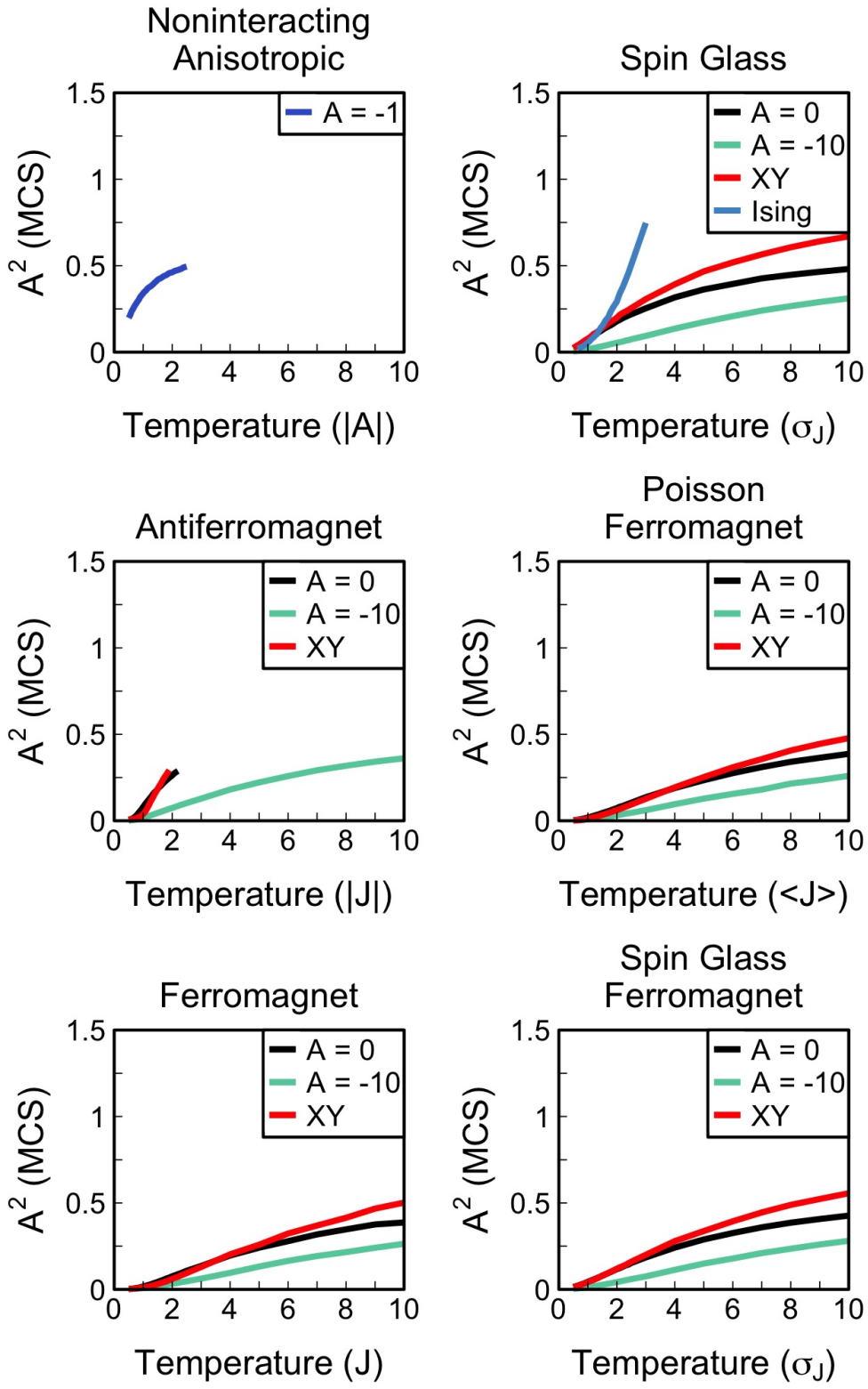

Figure 2.5: Noise amplitude averaged over spin components as a function of temperature for $(0.5 \leq T \leq 10)$.

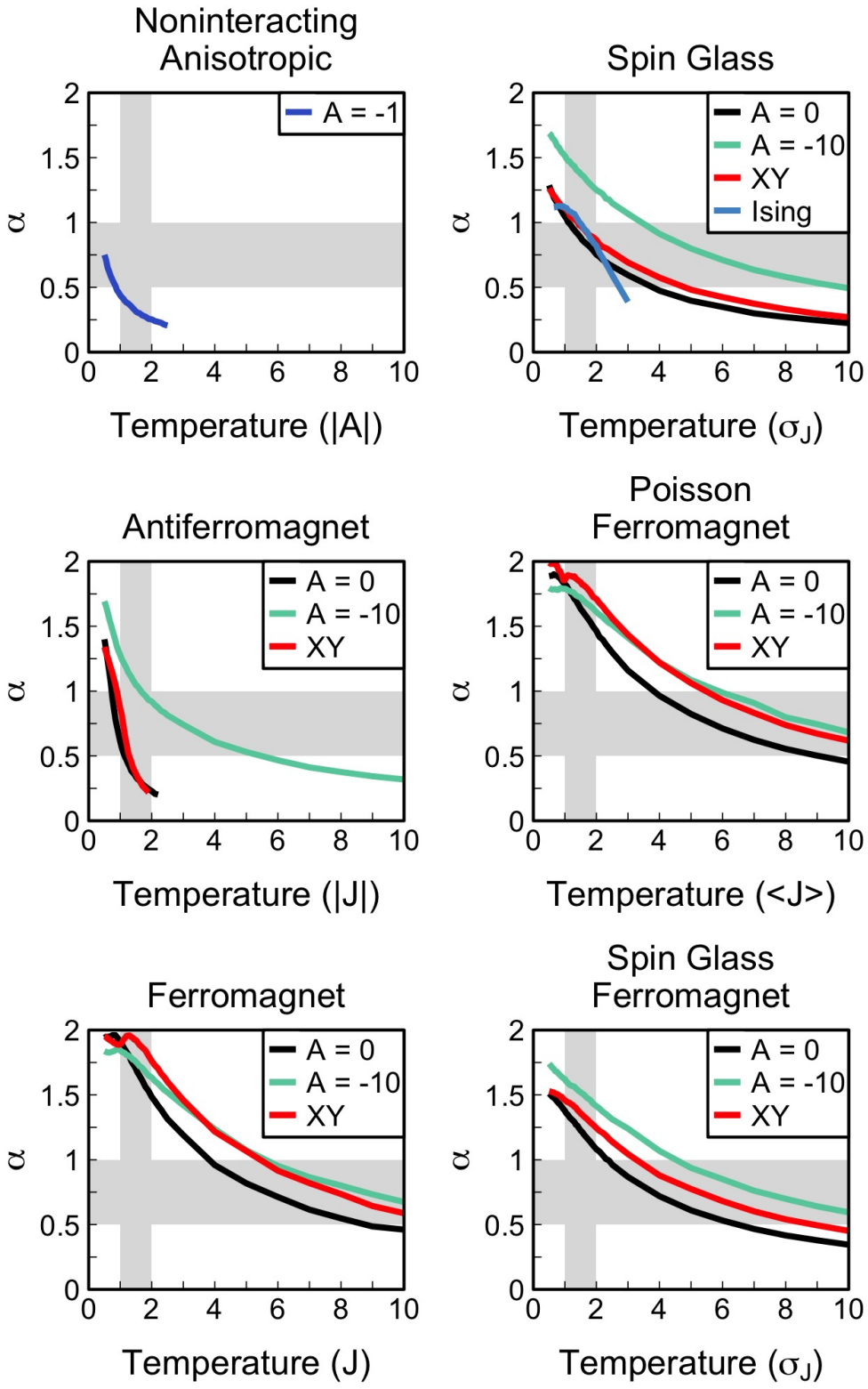

Figure 2.6: Noise exponents averaged over spin components as a function of temperature for ($0.5 \leq T \leq 10$). The shaded region indicates the experimental range of $0.5 \leq \alpha \leq 1$ and $1 \leq T \leq 2$.

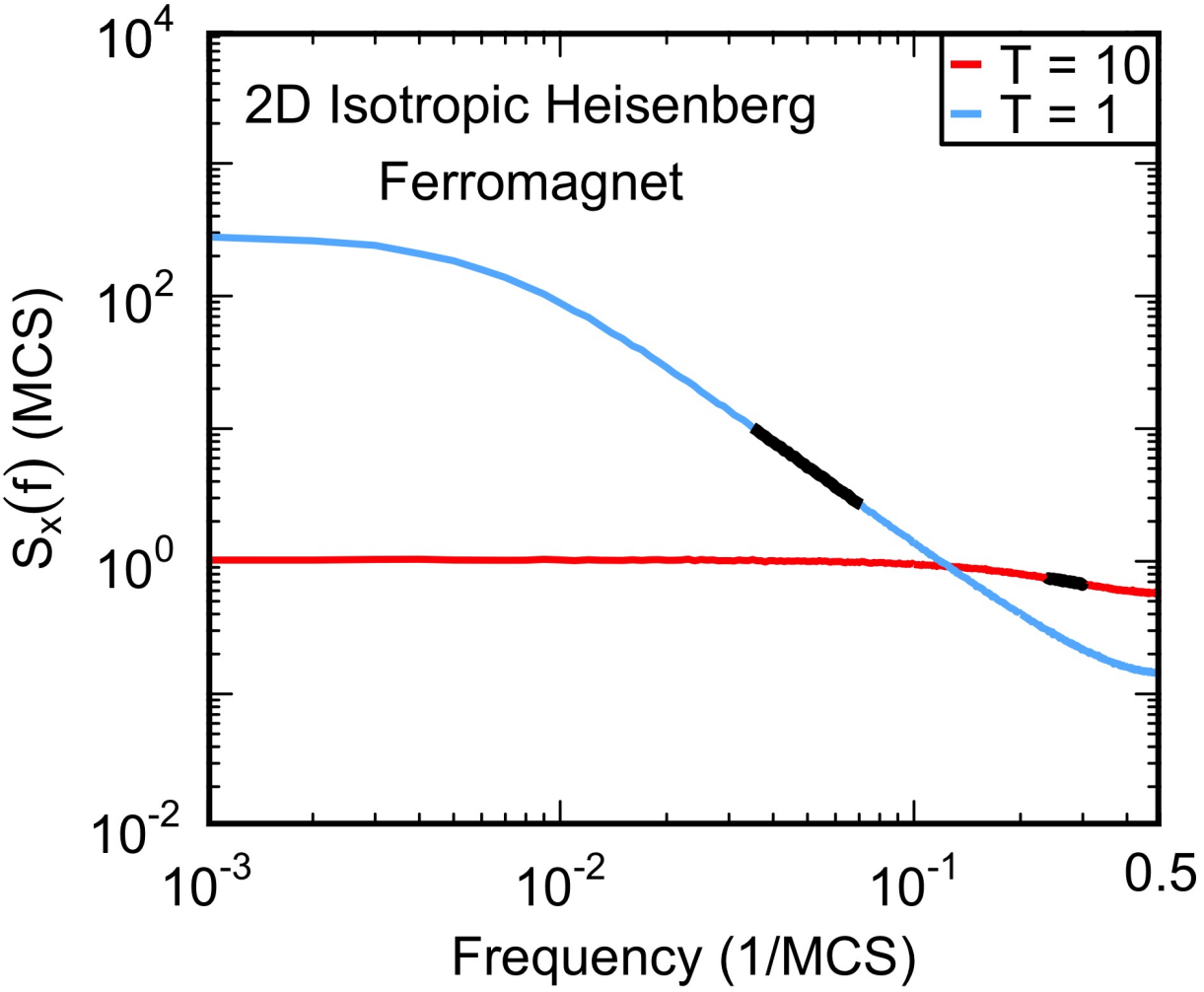

Figure 2.7: Noise power $S_x(f)$ of the x-component of the total magnetic moment of a 2D isotropic ($A = 0$) Heisenberg ferromagnet ($J_{ij} = 1$) versus frequency. Black lines indicate the frequency fit range of the noise power spectra averaged over 100 segments at $T = 10$ and $T = 1$.

of the power spectra for the 2D Ising spin glass for $1.7 \leq T \leq 2.3$. The anomalous high-temperature pivoting of power spectra for $4 \leq T \leq 10$ is presented in Appendix A.2 for the 2D Ising spin glass.

Spectral pivoting occurs for all systems tested except for the Heisenberg antiferromagnets with $A = 0$ and $A = -1$ as well as the XY antiferromagnet (see Fig. 2.8). Spectral pivoting is most evident at high temperatures well above the magnetic transition temperature T_c. This is consistent with experiments on flux noise where there is no conclusive evidence for a magnetic phase transition, indicating that the experimentally observed pivoting occurs at temperatures above any magnetic phase transition.

For our simulated spin systems that exhibit pivoting, as their temperature decreases, the spins change their orientations more slowly; the low-frequency noise power increases, and the noise power at high frequencies decreases. Note that the total noise power i.e. the integrated area under spectral density curve, is the same for all temperatures for the noninteracting Heisenberg model with anisotropy $A = -1$ and spin glass models with $T_c = 0$ is zero. As a result, increasing noise power at low frequencies means decreasing noise power at high frequencies.

We find that that the crossing frequency of the power spectra has a weak temperature dependence of the form $f_c = B \cdot T + f_0$. For noninteracting Heisenberg spins with anisotropy $A = -1$, $B = 0.023$ and $f_0 = -0.16$ for $0.5 \leq T \leq 2.5$. For comparison, $B = 0.11$ and $f_0 = -0.12$ for the isotropic Heisenberg ferromagnet for $1.25 \leq T \leq 2.5$. Spectral pivoting is an artifact that occurs at high temperature where the knee and aliasing regions are close to each other as seen in the inset of Fig. 2.9. At low temperatures where the knee and aliasing are not close, we do not see pivoting which can be seen in Fig. 2.9.

By changing a few simulation parameters, the pivoting can be affected. The pivoting of the power spectra of the Heisenberg ferromagnet when recording the magnetic moment at every time step using the "every-site method" is shown in Fig. 2.11(a). Using the method of randomly selecting sites for reorientation outlined in Sec. 2.2.3 results in a lower crossing frequency by lowering the frequency where aliasing occurs as shown in Fig. 2.11(b). Recording the magnetic moment time series every ten time steps as described in Sec. 2.2.4 also

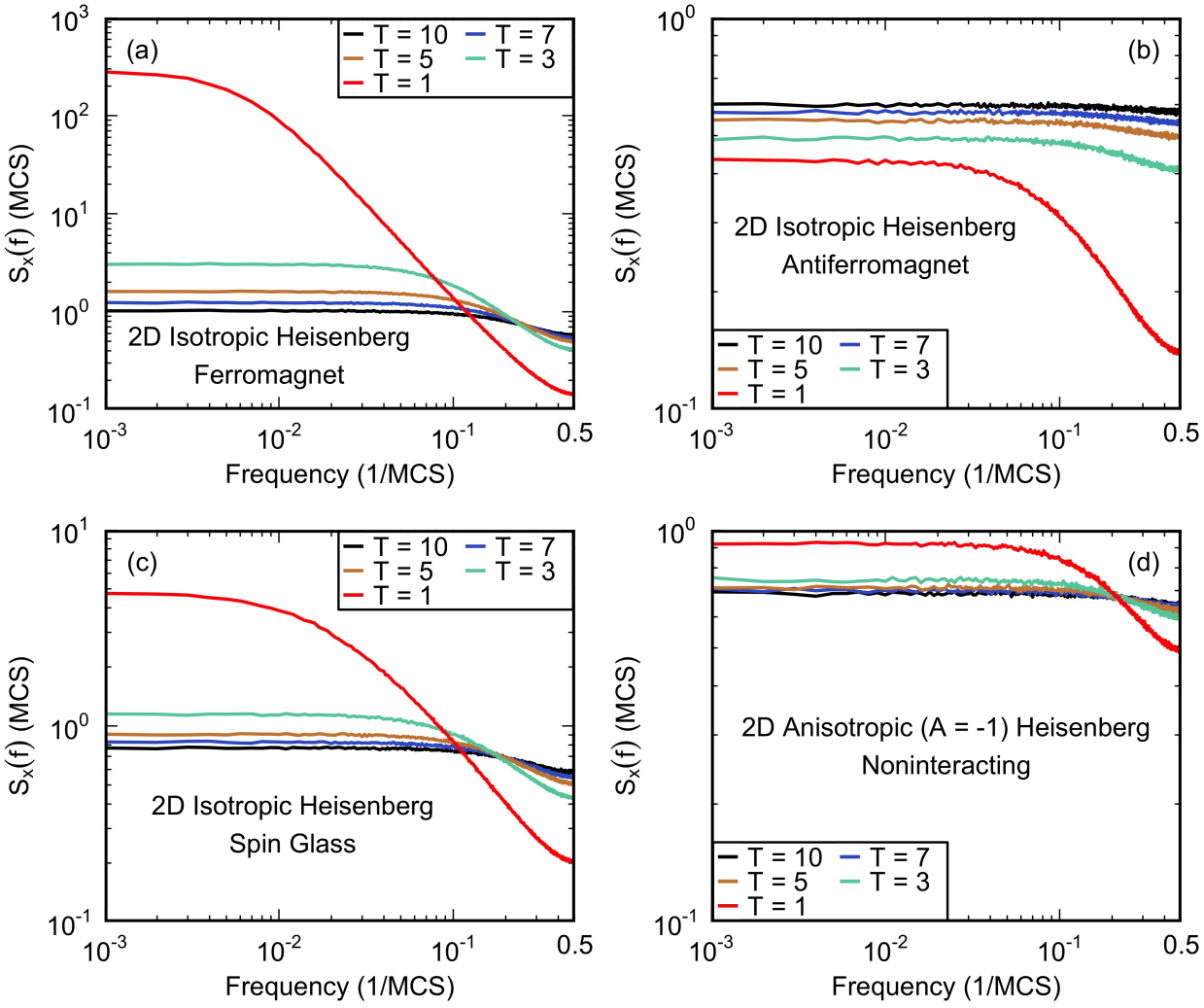

Figure 2.8: Noise power $S_x(f)$ of the x-component of the total magnetic moment versus frequency. Spectral pivoting of power spectra averaged over 100 segments of the 2D (a) isotropic ($A = 0$) ferromagnetic ($J_{ij} = 1$), (b) isotropic ($A = 0$) antiferromagnetic ($J_{ij} = -1$), (c) isotropic ($A = 0$) spin glass ($\langle J_{ij} \rangle = 0, \sigma_{J_{ij}} = 1$), and (d) noninteracting ($J_{ij} = 0$) anisotropic ($A = -1$) Heisenberg models for $1 \leq T \leq 10$.

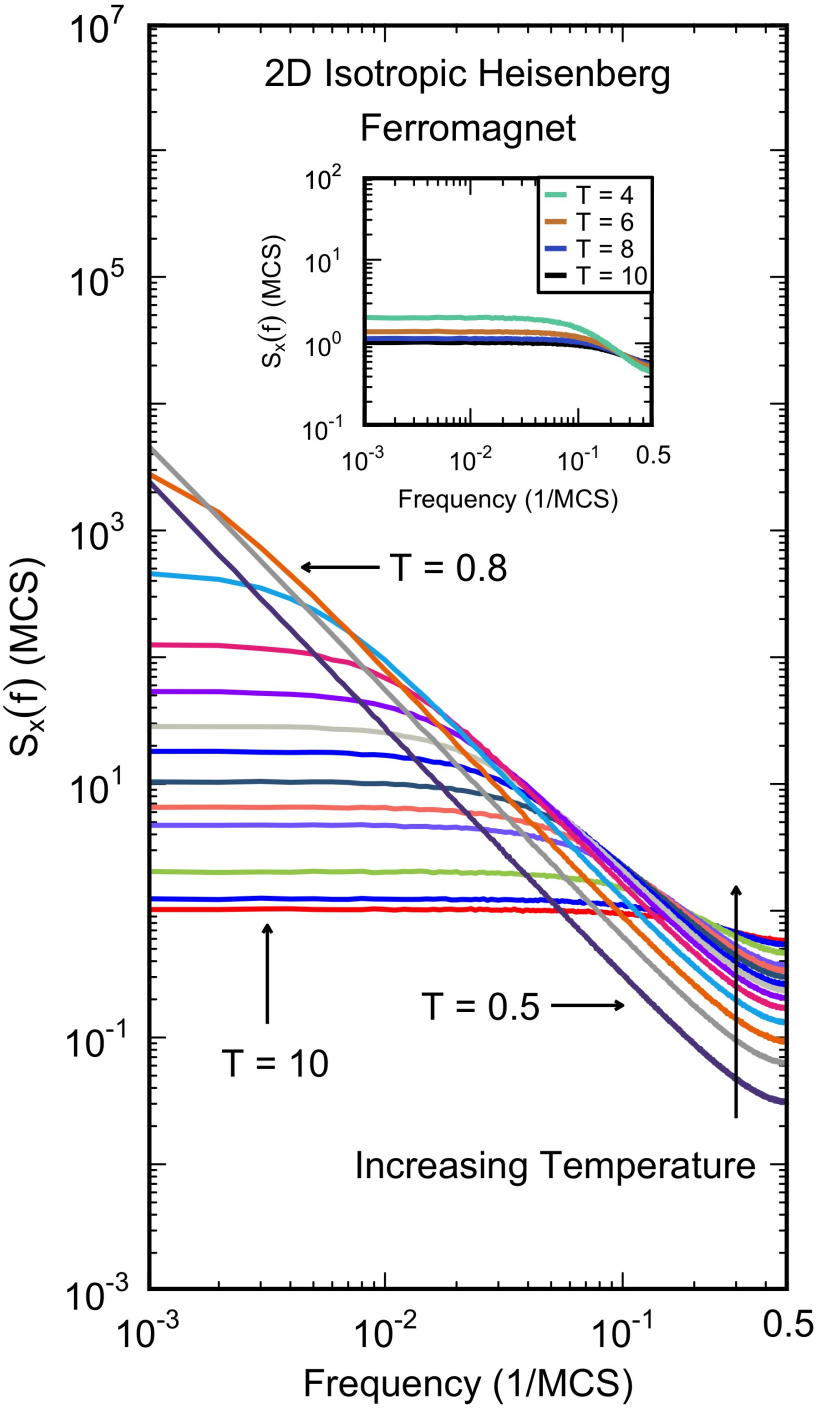

Figure 2.9: Noise power $S_x(f)$ of the x-component of the total magnetic moment of a 2D isotropic ($A = 0$) Heisenberg ferromagnet ($J_{ij} = 0$) versus frequency. Spectral pivoting of the power spectra averaged over 100 segments for $0.5 \leq T \leq 10$. The inset shows the power spectra averaged over 100 segments for $4 \leq T \leq 10$.

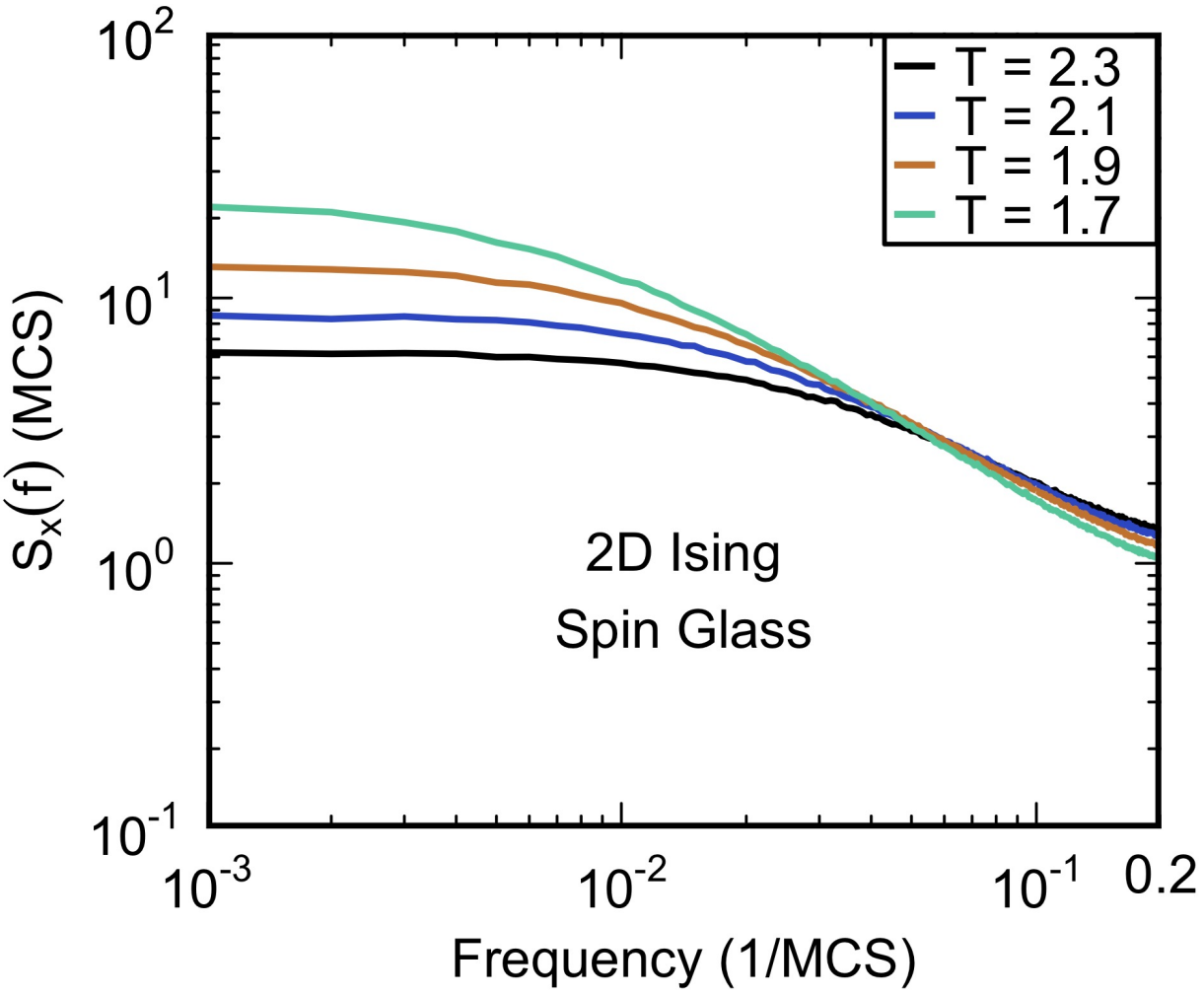

Figure 2.10: Noise power $S(f)$ of the total magnetic moment of a 2D Ising spin glass ($\langle J_{ij} \rangle = 0, \sigma_{J_{ij}} = 1$) versus frequency. Spectral pivoting of power spectra averaged over 100 segments for $1.7 \leq T \leq 2.3$.

lowers the crossing frequency compared to recording the magnetic moment time series at every time step as shown in Fig. 2.11(c).

2.3.5 Mean-Square Flux Noise

The mean-square flux noise is given by

$$\langle \Phi^2 \rangle = \int_{f_1}^{f_2} S_\Phi(f) df. \tag{2.9}$$

In experiments by Anton *et al.*, the mean-square flux noise in SQUIDs was found to increase with increasing temperature with $f_1 = 10^{-4}$ Hz and $f_2 = 10^9$ Hz [1]. In our simulations, the mean-square flux noise is equivalent to the total noise power with $f_1 = 0$ MCS^{-1} and $f_2 = 0.5$ MCS^{-1}. The total noise power is calculated for the isotropic ferromagnetic, noninteracting anisotropic, and isotropic antiferromagnetic Heisenberg systems for $0.5 \leq T \leq 10$. The total noise power as a function of temperature is shown in Fig. 2.12. We find that the results of Anton *et al.* are consistent with the results of our simulations for antiferromagnetic interactions but not other types of interactions.

2.4 Summary

Monte Carlo simulations of various spin models with nearest-neighbor exchange were carried out on 2D lattices to determine which interactions yield $\alpha \sim 1$ at low temperatures as well as to find cases of spectral pivoting. We find that the spin glass systems produce noise exponents that best match experiment [1, 23, 27]. In simulations, pivoting at high frequencies occurs as a result of the proximity of a low frequency knee and the aliasing of the noise power spectra. In experiments, aliasing can be avoided by using low-pass filters [12]. This work does not explain pivoting seen in experiments but it can explain the pivoting

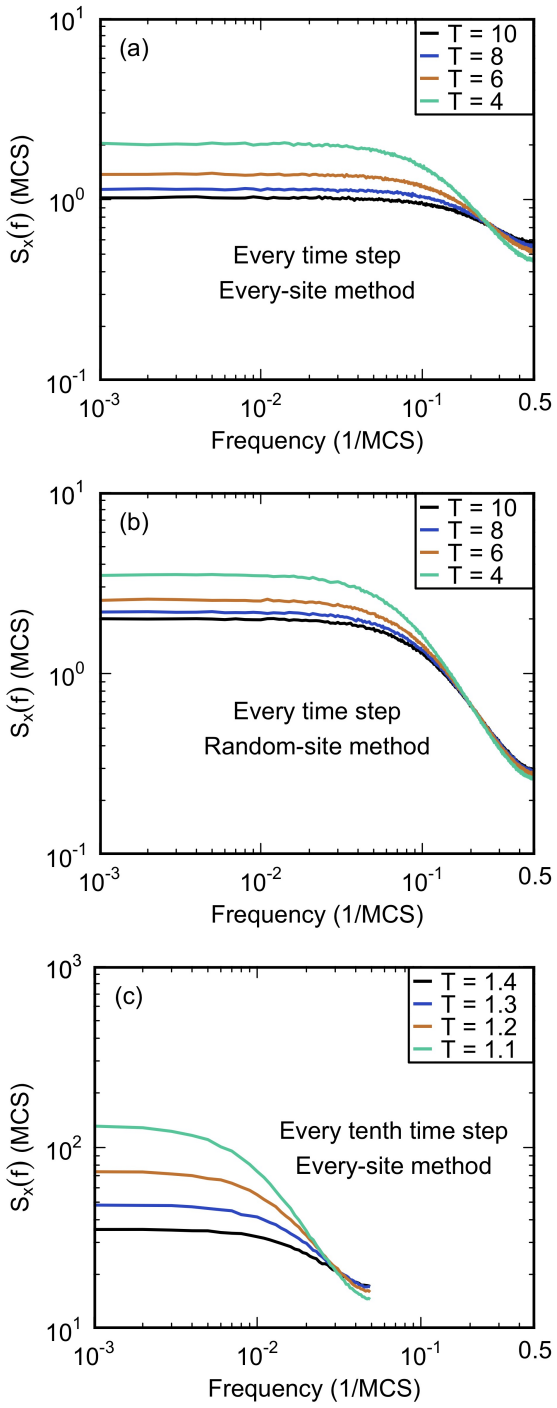

Figure 2.11: Noise power $S_x(f)$ of the x-component of the total magnetic moment of a 2D isotropic ($A = 0$) Heisenberg ferromagnet ($J_{ij} = 1$) versus frequency. Spectral pivoting of the x-component of the power spectra averaged over 100 segments resulting from recording the magnetic moment time series (a) at every time step using the "every-site method," (b) at every time step using the "random-site method," and (c) at every tenth time step using the "every-site method."

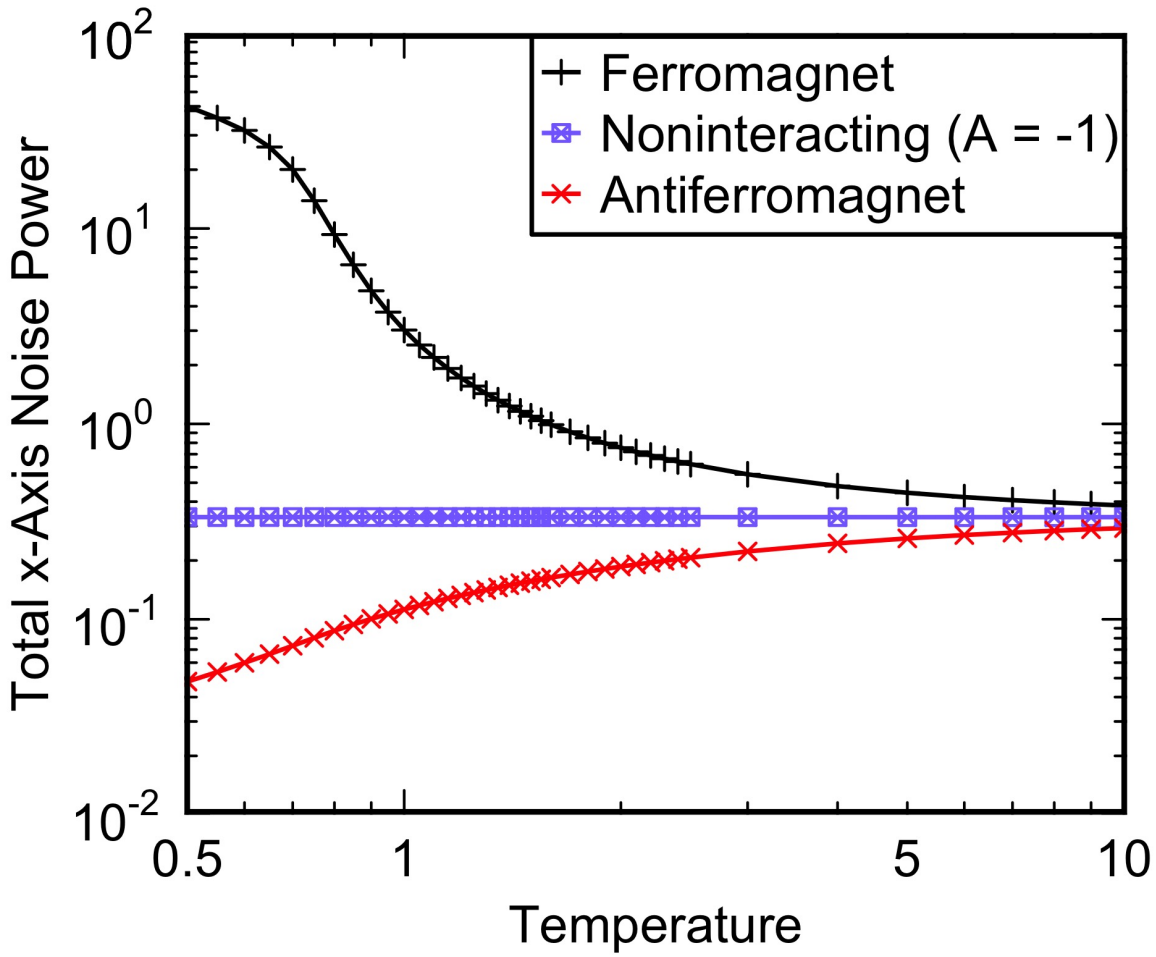

Figure 2.12: Total noise power ($\int_{0\ \mathrm{MCS}^{-1}}^{0.5\ \mathrm{MCS}^{-1}} S_x(f)df$) of the total magnetic moment versus temperature of the 2D isotropic ($A = 0$) ferromagnetic ($J_{ij} = 1$), noninteracting ($J_{ij} = 0$) anisotropic ($A = -1$), and isotropic ($A = 0$) antiferromagnetic ($J_{ij} = -1$) Heisenberg models for $0.5 \leq T \leq 10$.

we see in some simulations. We note that in our simulations pivoting is most evident at temperatures high compared with the magnetic transition temperature. Presumably this is consistent with experiments where there is no consistent evidence of a magnetic transition. This work also does not explain why the mean-square flux noise increases with temperature in the experiment by Anton *et al.* [1]. We find that this is characteristic of antiferromagnetic interactions between spins, for which there is no other experimental evidence.

Chapter 3

Effects of Temperature Fluctuations on Charge Noise in Quantum Dot Qubits

3.1 Introduction

Decoherence arising from charge noise presents a challenge to the use of silicon quantum dots (QDs) as quantum bits. The charge noise spectrum in Si/SiGe quantum dots goes as $1/f^{\alpha}$ with $\alpha \lesssim 1$ over many decades in frequency [42, 43], where f is the frequency and α is the noise exponent.

Charge noise in quantum dots arises due to coupling to two-level fluctuators (TLFs). Experiments have shown that each quantum dot is coupled to a small number of fluctuators [2, 44]. While initial experiments indicated that the noise in neighboring quantum dots is not correlated [18], more direct subsequent experiments did find correlations [45]. With only a few two-level fluctuators, a Lorentzian power spectra is expected, but instead, noise with a

$1/f^\alpha$ power spectrum is observed with $\alpha \lesssim 1$. Typically, $1/f$-like noise is produced by an ensemble of two-level fluctuators with a broad distribution of relaxation rates [29, 46].

Ahn *et al.* [2] have suggested that the quantum dots are coupled to a small number of two-level fluctuators that are each in turn coupled to a microscopic subsection of the larger thermal bath that they take to be the 2D electron gas (2DEG) in which the quantum dots are embedded. They propose that temperature fluctuations in the sub-bath cause the noise to have a $1/f^\alpha$ spectrum over several decades of frequency with $\alpha \sim 1$. They calculate the noise power spectral density by performing a quenched average over a distribution of temperatures and show that this average yields a $1/f^\alpha$ noise spectrum even for small numbers of fluctuators. However, they did not specify the conditions under which the quenched average is justified. (By "quenched average", we mean an average over a distribution of temperatures where each temperature is infinitely long lived.)

Here, we represent the fluctuator in two ways. The first way is as a single Heisenberg spin in an anisotropic potential subjected to temperature fluctuations. The second way is as a single Ising spin with thermally activated flips subjected to temperature fluctuations. Using Monte Carlo simulations of this spin, we find that a $1/f$ magnetic noise spectrum requires very slow temperature fluctuations, with each temperature being extremely long-lived. To confirm this result, we perform several analytical calculations. In one calculation, the fluctuator is a two-state system in a double well potential subject to periodic temperature oscillations; we show that the noise spectrum is Lorentzian at frequencies lower than the oscillation frequency. In the other calculation, the fluctuator is a two-state system that has a time dependent switching rate. We consider the case where the switching rate is a sequence of constant, but random, rates. Each rate has an average duration t_o and corresponds to a certain temperature. Changing the rate corresponds to changing the temperatures. We find that t_o must be very long in order to achieve $1/f$ noise at low frequencies. We use our result to reproduce the results of Ahn *et al.* where t_o is infinite and show what happens when the

temperature fluctuations have a finite lifetime. We then estimate the longest possible time scale of temperature fluctuations based on thermal diffusion in the confined geometry of the device and conclude that the temperature fluctuations in a sub-bath of the 2DEG cannot live long enough to account for the observed $1/f$ noise.

3.2 Monte Carlo Simulation of a Single Heisenberg Spin

3.2.1 Spin Model

In the model of Ahn *et al.* a thermally activated two-level fluctuator (TLF) [2] is coupled to a quantum dot, with fluctuations in the TLF leading to charge noise in the quantum dot. The thermally activated time for the fluctuator to switch is given by $\tau \exp(U/T)$ where U is barrier height and τ^{-1} is the attempt frequency. While a single TLF with a characteristic temperature-dependent relaxation rate produces a Lorentzian noise power spectrum, if the TLF is coupled to a microscopic subsection of the larger thermal bath, as Ahn *et al.* propose [2], then fluctuations in the sub-bath temperature have the potential to give rise to multiple relaxation rates associated with a single TLF resulting in a $1/f$ noise power spectrum. Here, we wish to elucidate how the noise spectrum depends on the nature of the time variation of the temperature fluctuations of the bath.

To test the model of Ahn *et al.*, we represent the thermally activated TLF by a Heisenberg spin with easy z-axis anisotropy. The barrier in the xy plane gives two energy minima along the $\pm$ z-axis. This energy barrier for the spin is shown in the inset of Figure 3.1. The

Heisenberg Hamiltonian is given by

$$H = -(S_z)^2 = -\cos^2\theta, \tag{3.1}$$

where S_z is the z component of a classical spin of length 1; θ is the polar angle between the z-axis and the spin direction.

3.2.2 Simulation Details

In our simulations with a single Heisenberg spin, we initialize the spin with a random orientation at high temperature. The spin is subsequently reoriented according to the Metropolis algorithm [36, 47]. Standard Monte Carlo dynamics at temperature T_j are used: given a configuration, its energy E_i is calculated; a new configuration is chosen and its energy E_f calculated; if $E_f < E_i$, then the new configuration is accepted, while if $E_f > E_i$, then the new configuration is accepted with probability $\exp[-(E_f - E_i)/(k_B T_j)]$. The energy of the spin is independent of the azimuthal angle, so the azimuthal component is chosen at random to be between 0 and 2π. The polar angle is restricted to change from its previous value by at most $\frac{\pi}{10}$ so that the spin must go over an energy barrier to make a transition between the two potential wells. The time it takes for one reorientation of the spin is one Monte Carlo step (MCS).

The system is run with the average temperature $T = 0.5$. Temperature fluctuations are implemented by first setting the system temperature to T_1 which is chosen from a normal distribution with average T and standard deviation 0.3T to emulate the temperature distribution of Ahn *et al* [2]. The temperature remains at T_1 for a time $t_{\text{fluctuation,1}}$ which is chosen from a flat distribution between $t_{\text{fluctuation,min}}$ and $t_{\text{fluctuation,max}}$. Next, another temperature T_2 is chosen, and it lasts for a time $t_{\text{fluctuation,2}}$. This process of choosing fluctuation temperatures occurs a total of N times such that $\sum_{j=1}^{j=N} t_{\text{fluctuation},j} = t_{\text{total}}$. In all simulations,

$t_{\text{total}} = 10^7$ MCS. Due to the random variation of $t_{\text{fluctuation}}$, N may vary with temperature. During this process, the magnetization is recorded. The simulations start with random spin configurations.

3.2.3 Noise Power

The discrete time series of the magnetization is given by $m_a(t_j)$, where the axes $a = x, y, z$. The deviation from the average is $\delta m_a(t_j) = m_a(t_j) - \overline{m_a(t_j)}$ and t_{total} is the length of the time series. The noise power spectral density can be determined from the Fourier transform of the autocorrelation function of the time series. The autocorrelation is given by

$$C_a(t_k) = \frac{1}{t_{\text{total}}} \sum_{j=0}^{t_{\text{total}}-1} \delta m(t_j) \delta m^*(t_{j-k}), \tag{3.2}$$

where $\delta m_a^*(t_{j-k})$ is the complex conjugate of $\delta m_a(t_{j-k})$. $\delta m_a(t_j)$ can be expanded in a Fourier series given by

$$\delta m_a(t_j) = \frac{1}{t_{\text{total}}} \sum_{k=0}^{t_{\text{total}}-1} \tilde{m}_a(f_k) e^{2\pi i f_k t_j / t_{\text{total}}}, \tag{3.3}$$

where $\tilde{m}_a(f_k)$ are the Fourier coefficients of the time series. Using Eq. (3.3), the autocorrelation becomes

$$C_a(t_k) = \frac{1}{t_{\text{total}}^3} \sum_{j=0}^{t_{\text{total}}-1} \left[\left(\sum_{l=0}^{t_{\text{total}}-1} \tilde{m}_a(f_l) e^{2\pi i f_l t_j / t_{\text{total}}} \right) \times \left(\sum_{n=0}^{t_{\text{total}}-1} \tilde{m}_a^*(f_n) e^{-2\pi i f_n (t_j - t_k)/t_{\text{total}}} \right) \right]. \tag{3.4}$$

This can be simplified to

$$C_a(t_k) = \frac{1}{t_{\text{total}}^2} \sum_{n=0}^{t_{\text{total}}-1} |\tilde{m}_a(f_n)|^2 e^{2\pi i f_n t_k / t_{\text{total}}}. \tag{3.5}$$

Taking the Fourier transform of Eq. (3.5) gives the periodogram estimate [37] for computing the noise power $S_a(f_k)$ for the axes $a = x, y, z$:

$$S_a(f_k) = \frac{1}{t_{\text{total}}} |\tilde{m}_a(f_k)|^2. \tag{3.6}$$

The Fourier transform is computed using the C subroutine library FFTW [38].

3.2.4 Heisenberg Simulation Results

We performed four sets of runs with different fluctuation times: 500 MCS $\leq t_{\text{fluctuation}} \leq$ 200,000 MCS, 50 MCS $\leq t_{\text{fluctuation}} \leq$ 20,000 MCS, $t_{\text{fluctuation}} =$ 100,000 MCS, and $t_{\text{fluctuation}} =$ 10,000 MCS. We record the magnetization of the Heisenberg spin as a function of time for 10^7 MCS. Each system is run 200 times, and the power spectra is averaged over the 200 runs. The power spectra of the four sets of runs, where the temperature fluctuates around $T = 0.5$, are shown in Figure 3.1.

We compare these power spectra to the one of Ahn *et al.* [2]. In our simulations, there is a low-frequency knee where the power spectra transitions from white noise at low frequency to $1/f$ noise at higher frequencies. The frequency of this knee is proportional to $t^{-1}_{\text{fluctuation,max}}$, where $t_{\text{fluctuation,max}}$ ranges from 10,000 MCS to 200,000 MCS. The result that the system needs to have a long $t_{\text{fluctuation,max}}$ in order to have $1/f$ noise at low frequencies is supported by our power spectra where a larger $t_{\text{fluctuation}}$ results in a lower frequency knee. This knee is not present in the power spectrum of Ahn *et al.* who find a power spectra that goes as $1/f^{0.8}$ at low frequency. This is because their calculation was a quenched average over an ensemble of TLFs, each remaining at a different temperature forever.

Although the results of Heisenberg spin model indicate that the temperature fluctuations need to be long-lived, the computation time needed to produce cleaner power spectra similar

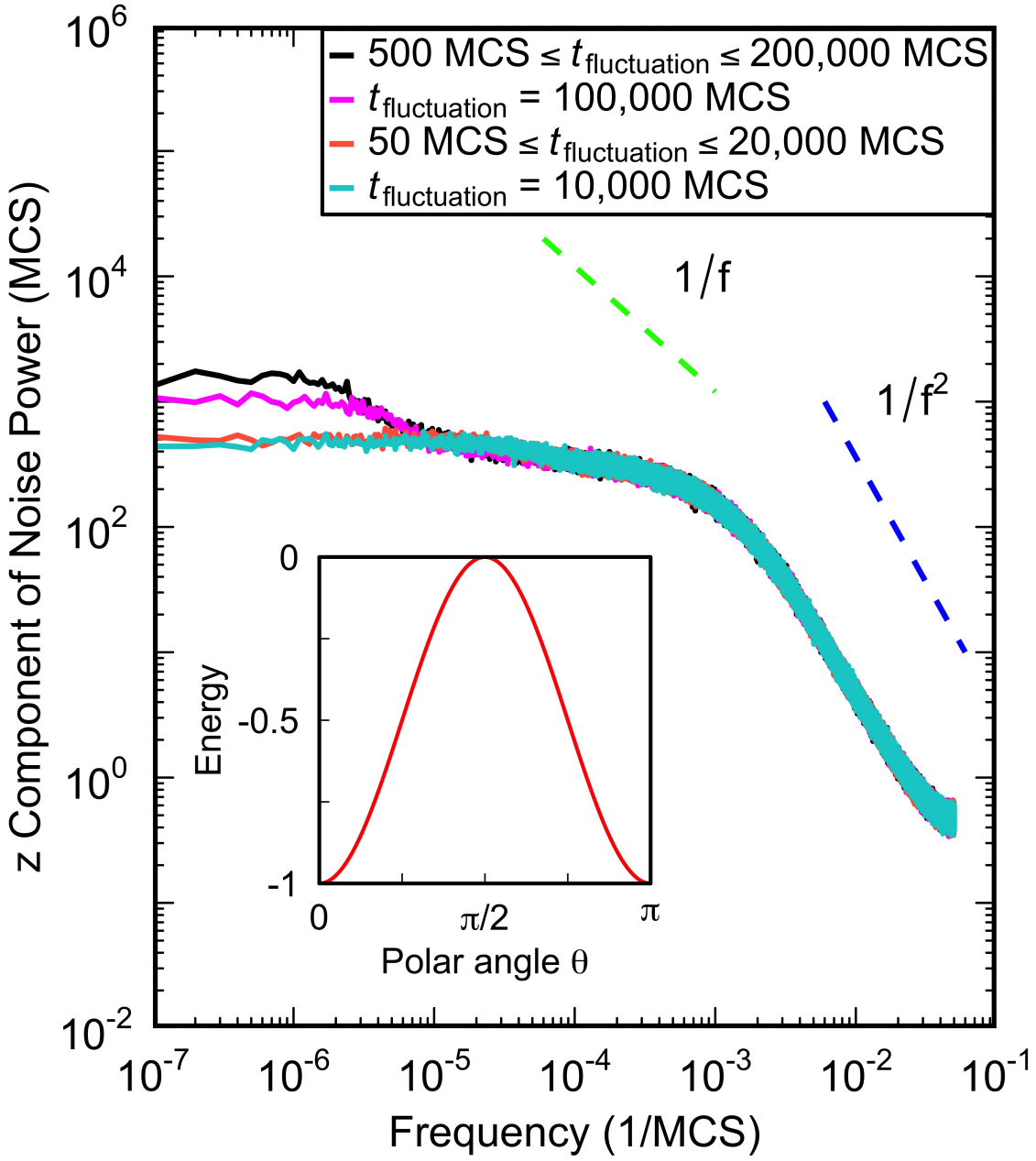

Figure 3.1: z component of the noise power spectrum at $T = 0.5$ averaged over 200 runs for an easy z-axis Heisenberg spin with two flat distributions of $t_{\text{fluctuation}}$ (500 MCS $\leq t_{\text{fluctuation}} \leq 200,000$ MCS and 50 MCS $\leq t_{\text{fluctuation}} \leq 20,000$ MCS) and two fixed $t_{\text{fluctuation}}$ (100,000 MCS and 10,000 MCS). For reference, lines of $1/f$ and $1/f^2$ are shown. Inset: The energy of a spin as a function of θ, the angle between the spin direction and the z-axis. For each power spectrum, the knee where the power spectra transitions from white noise at low frequency to $1/f^{\alpha}$ at a frequency approximately equal to the $t^{-1}_{\text{fluctuation,max}}$ for the respective set of runs. In the intermediate region, $S(f) \sim 1/f^{0.16}$, and in the high-frequency region, $S(f) \sim 1/f^{1.85}$. Thus, the intermediate region is cut off at low frequencies at a frequency scale $\propto t^{-1}_{\text{fluctuation,max}}$.

to that of Ahn *et al.* would be excessive. Instead, we perform Monte Carlo simulations of a single Ising spin subjected to temperature fluctuations.

3.3 Monte Carlo Simulation of a Single Ising Spin

As another test of the model by Ahn *et al.*, we present Monte Carlo simulations constructed by Hervé Carruzzo. The thermally activated TLF is represented by a single Ising spin which flips between $S_z = -1$ and $S_z = +1$ with a probability $P_i = e^{-U/T_i}$ where $U = 1$ and T_i is the temperature during the ith time interval, and time is measured in units of τ. Since the temperature depends on time, there is a sequence of different temperatures that are drawn from a Gaussian distribution that is truncated to exclude negative temperatures [2]:

$$f(T_i, T_{\text{avg}}, \sigma_{\text{sb}}) = \xi \frac{e^{-(T_i - T_{\text{avg}})^2/2\sigma_{\text{sb}}^2}}{\sqrt{\pi/2}\sigma_{\text{sb}}}, \tag{3.7}$$

where T_{avg} is the average sub-bath temperature, σ_{sb}^2 the variance, and ξ is a normalization factor that accounts for the truncation of the Gaussian. This distribution is the one used by Ahn *et al.* [2]. Following Ahn *et al.*, we set $T_{\text{avg}} = 1$ and $\sigma_{\text{sb}} = 0.3$. In this case $\xi \sim 1$.

The spin is reoriented according to standard Monte Carlo dynamics. A random number between zero and 1 is generated from a uniform distribution and if it is less than or equal to P_i, the spin flips. The duration Δ_i of the ith temperature is drawn from an exponential distribution:

$$P_d(\Delta) = \frac{1}{t_o} e^{-\Delta/t_o}, \tag{3.8}$$

where t_o is the characteristic duration of a given temperature. The length of each run is 6×10^8 time steps. Noise power spectra are calculated during the runs at 30 frequencies evenly spaced on a logarithmic scale.

The low frequency noise spectrum is dominated by low temperatures that are in the tail of the distribution and are, therefore, not often sampled by random draws. Therefore, we divide the temperature range from $T = 0.03$ to $T = 2.0$ into 300 equal increments and start one run from each of these 300 temperatures. After the initial temperature of a run is finished, i.e., after Δ_1 steps, the subsequent temperatures in that run are chosen randomly from the Gaussian distribution. The noise spectrum from the resulting time series is given a Gaussian weight corresponding to the initial temperature and Eq. (3.7). This is how we average over the 300 noise spectra. 13 sets of 300 runs were performed. The results are shown in Fig. 3.2 for $t_o = 10^5,\ 10^6,\ 10^{12}$. All the spectra are normalized so that the total noise power is unity. One can see that as t_o increases, the knee moves to lower frequencies indicating that slow, long-lived temperature fluctuations are needed to observe $1/f$ noise at low frequencies.

We can compare these power spectra to the one of Ahn *et al.* [2]. Ahn *et al.* had infinitely long-lived temperature fluctuations and so their results should be compared to our case of $t_o = 10^{12}$. For shorter t_o, one can see that there is a low-frequency knee where the power spectra crosses over from white noise at low frequency to $1/f$ noise at higher frequencies. The frequency at which this knee occurs is proportional to $1/t_o$. Our contention that the temperature fluctuations must be slow in order for the noise to have a $1/f$ spectrum at low frequencies is supported by our power spectra, where increasing t_o lowers the frequency of the knee. As was found in our simulations of Heisenberg spin in section 3.2.4, the knee in our Ising simulations is not present in the power spectrum of Ahn *et al.*

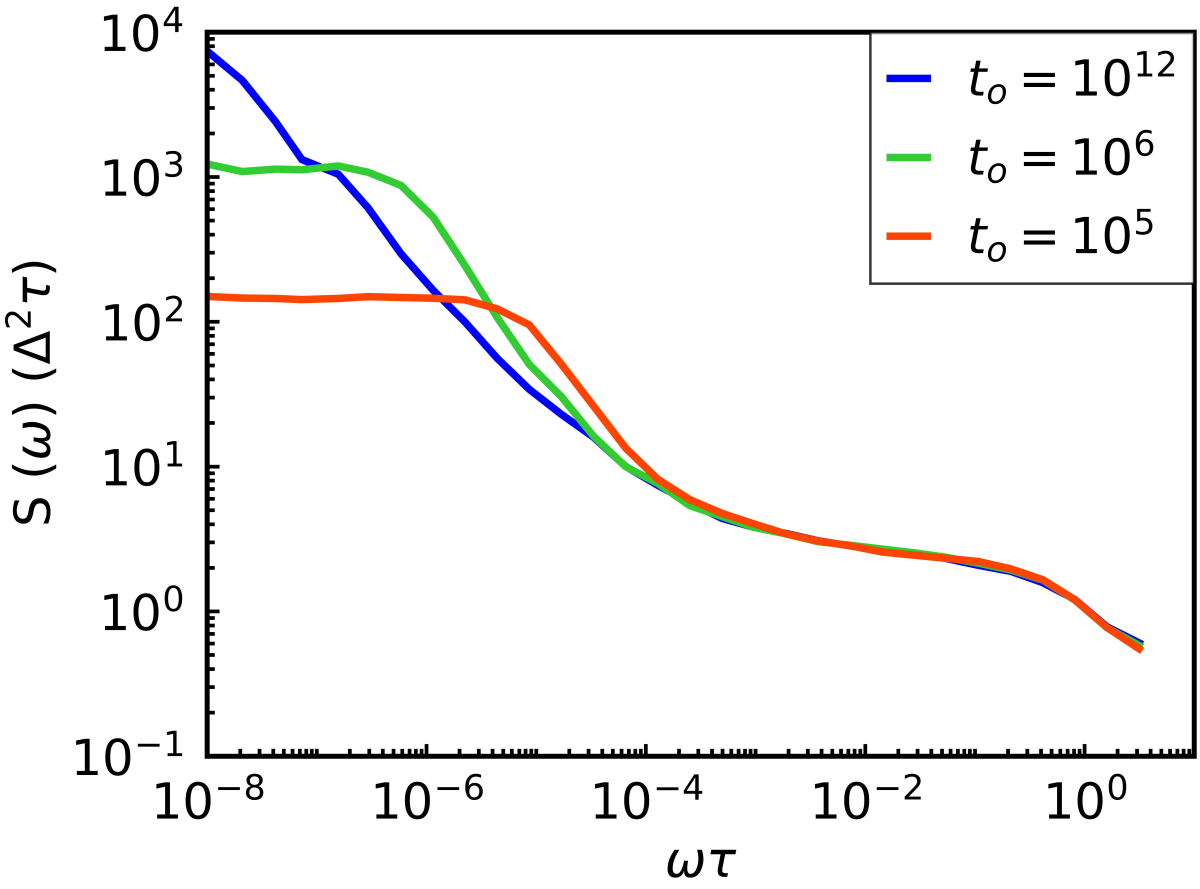

Figure 3.2: Plot of the spectral power densities of the noise, $S(\omega)$ versus angular frequency ω for an Ising spin in the presence of temperature fluctuations with average duration $t_o = 10^5$ (red), 10^6 (green), and 10^{12} (blue) (as defined in Eq. (3.8)). The noise spectra are averaged over 13 sets of 300 runs. Each run consists of 6×10^8 Monte Carlo Steps (MCS). All times are measured in units of τ, the inverse of the fluctuator's attempt frequency.

3.4 Low-Frequency Noise Spectrum of a Two-State Fluctuator Subjected to Temperature Oscillations

To confirm the conclusion from our simulation results that the rise in the power spectrum cuts off at frequencies lower than those of the flucuations of the bath, we calculate the noise spectrum of a two-state system in a double well potential subjected to periodic temperature oscillations. Our goal is to see if the spectrum is Lorentzian at frequencies lower than the drive frequency, which would be consistent with our assertion that $1/f$ noise at a given frequency is produced by fluctuations at comparable frequencies.

We follow the calculation of [48] which we briefly review. We imagine a particle in a double well potential with energy asymmetry ε. The particle has two position states: $x_+ = 1$ and $x_- = -1$. The corresponding probability of being in the $+1$ (or -1) state is n_+ (or n_-), and the transition rate out of that state is $W_+(t)$ (or $W_-(t)$) where in our case, the time dependence arises because of temperature oscillations with period $T_s = 2\pi/\omega_s$. (We assume that the relaxation time associated with equilibrating within one well is much shorter than the period T_s of driving.) We assume that the transition rates are periodic with period T_s. The probability that the system in state in state $x_\pm$ makes a transition to $x_\mp$ in a time interval dt is $W_\pm(t)dt$. Thus, the rate equation for the population $n_+(t)$ is

$$\begin{aligned} \frac{dn_+(t)}{dt} &= W_-(t)n_-(t) - W_+(t)n_+(t) \\ &= W_-(t) - W(t)n_+(t), \end{aligned} \tag{3.9}$$

where we used $n_+(t) + n_-(t) = 1$ and $W(t) \equiv W_+(t) + W_-(t)$. It is straightforward to solve this first order differential equation using an integrating factor [48, 49]. The power spectrum $S(\omega)$ is the Fourier transform of the correlation function $C(\tau) = \langle x(t)x(t+\tau)\rangle$, where $\langle \dots \rangle$

denotes a time average. McNamara and Wiesenfeld [49] showed that this can be written as

$$C(\tau) = \langle n_+(t+\tau|+,t)n_+(t) - n_+(t+\tau|-,t)n_-(t) - \\ n_-(t+\tau|+,t)n_+(t) + n_-(t+\tau|-,t)n_-(t)\rangle, \tag{3.10}$$

where $n_+(t_2|\pm,t)$ is the probability that the system is in the $x = 1$ state at time t_2 given that it was in state $x = \pm 1$ at time t, and

$$n_+(t) = \lim_{(t-t_0)\to\infty} n_+(t|x_0,t_0). \tag{3.11}$$

To understand the terms in Eq. (3.10), consider, for example, $n_+(t+\tau|-,t)n_-(t)$; it represents the case that at time t the particle is at $x = -1$, and at time $t+\tau$ it is at $x = +1$.

Löfstedt and Coppersmith [48] showed that the temporal correlation function could be written as a sum of a signal term $C_S(\tau)$ and a noise term $C_N(\tau)$, i.e., $C(\tau) = C_S(\tau) + C_N(\tau)$. $C_S(\tau)$ is periodic, $C_N(\tau + T_s) = C_N(\tau)$ and is given by

$$C_S(\tau) = \langle [1 - 2n_+(t+\tau)]\,[1 - 2n_+(t)]\rangle. \tag{3.12}$$

By defining

$$\delta n_+(t+\tau|x_0,t) = n_+(t+\tau|x_0,t) - n_+(t+\tau), \tag{3.13}$$

one can write the noise term as

$$C_N(\tau) = 2\langle [\delta n_+\,(t+\tau|+,t) + \delta n_+\,(t+\tau|-,t)]\,n_+(t) - \delta n_+\,(t+\tau|-,t)\rangle. \tag{3.14}$$

It is shown in [48] that

$$\begin{aligned} C_N(\tau) &= \frac{4}{T_s} e^{-\langle W\rangle \tau} \int_0^{T_s} h(t, t+\tau) n_+(t) \left(1 - n_+(t)\right) dt \\ &= e^{-\langle W\rangle \tau} \chi_N(\tau), \end{aligned} \tag{3.15}$$

where $\langle W \rangle$ is the time average of the sum of the rates,

$$\langle W \rangle = \frac{1}{T_s} \int_0^{T_s} \left(W_+(t) + W_-(t)\right) dt, \tag{3.16}$$

and $h(t_1, t_2)$ is given by

$$h(t_1, t_2) = \exp\left[- \int_{t_1}^{t_2} \left(W(t') - \langle W \rangle\right) dt' \right]. \tag{3.17}$$

Note that $\chi_N(\tau)$ in Eq. (3.15) is periodic, i.e., $\chi_N(\tau) = \chi_N(\tau + T_s)$.

By Fourier transforming $C_N(\tau)$ in Eq. (3.15), we can obtain the noise spectrum of a two state fluctuator subjected to periodic temperature oscillations $T(t) = T_0 + \delta T \cos(\omega_s t)$ where δT is the temperature fluctuation amplitude and we set the mean temperature $T_0 = 1$. Just as for our Heisenberg spin (see inset of Fig. 1), we assume that the double well potential is symmetric, i.e., the asymmetry $\varepsilon = 0$. As a result, the occupation probabilities will be $n_+(t) = n_-(t) = 0.5$. In addition, the transition rates are activated: transition rates $W_+(t) = W_-(t) = W_\pm(t) = \omega_o e^{-U/T(t)}$, where we set the barrier energy $U = 1$ and the attempt frequency $\omega_o = 1$.

The form of the transition rates require a nonperturbative numerical calculation. We begin by expanding the rates in a Fourier series:

$$W_\pm(t) = \omega_s \left(W_{\pm,0} + W_{\pm,1} \cos(\omega_s t) + W_{\pm,2} \cos(2\omega_s t) + \dots\right), \tag{3.18}$$

	$n=0$	$n=1$	$n=2$	$n=3$
$W_{\pm,n}$	4.38	1.36	-0.100	0.00443
A_n	0	1.48	-1.21	0.386
B_n	15.2	-18.8	5.29	-0.779

Table 3.1: Fourier coefficients for the activated transition rates $W_{\pm}(t)$ and the periodic factor $\chi_N(\tau)$ of the noise correlation function $C_N(\tau)$ up to third order.

where the Fourier coefficients are

$$\begin{aligned} W_{\pm,0} &= \frac{\omega_s}{2\pi}\int_0^{2\pi/\omega_s} W_{\pm}(t)dt \\ W_{\pm,n} &= \frac{\omega_s}{\pi}\int_0^{2\pi/\omega_s} W_{\pm}(t)\cos(n\omega_s t)dt. \end{aligned} \tag{3.19}$$

We determine $W_{\pm,n}$ numerically using Mathematica for $n = 0, 1, 2, 3$ using $\delta T = 0.3$ and $\omega_s = 0.082085$ as in [48]. The results are shown in Table 3.1.

Substituting the Fourier series in Eq. (3.18) into Eq. (3.16) yields $\langle W\rangle = 2\omega_s W_{\pm,0}$. To evaluate $h(t_1, t_2)$, we plug this result for $\langle W\rangle$ as well as Eq. (3.18) into Eq. (3.17) and evaluate the integrals to obtain:

$$\begin{aligned} h(t_1,t_2) = \exp\big[-2\,(&W_{\pm,1}\,(\sin(\omega_s t_2) - \sin(\omega_s t_1)) + \\ &W_{\pm,2}/2\cdot(\sin(2\omega_s t_2) - \sin(2\omega_s t_1)) + \dots)\big]. \end{aligned} \tag{3.20}$$

We can use this result to evaluate the periodic function $\chi_N(\tau)$ in the noise correlation function $C_N(\tau)$:

$$\chi_N(\tau) = \frac{4}{T_s}\int_0^{T_s} (1 - n_+(t))\, n_+(t) h(t, t+\tau)dt. \tag{3.21}$$

We evaluate $\chi_N(\tau)$ numerically from $\tau = 0$ to $\tau = T_s$ in steps of $\Delta\tau = T_s/200$. Since $\chi_N(\tau)$

is periodic with frequency ω_s, we can fit the numerical solution to a Fourier series:

$$\chi_N(\tau) = \sum_{n=1}^{N} A_n \sin(n\omega_s t) + \sum_{n=0}^{N} B_n \cos(n\omega_s t), \tag{3.22}$$

where we set $N = 3$. The values of the Fourier coefficients are given in Table 3.1.

We want to compare the magnitudes of the Fourier coefficients of the higher harmonics to that of the fundamental frequency to determine whether the noise power approximates that of a Lorentzian. To facilitate this, we fit $\chi_N(\tau)$ to a complex Fourier series:

$$\chi_N(\tau) = \sum_{n=-\infty}^{\infty} \tilde{\chi}_N(n) e^{in\omega_s \tau}, \tag{3.23}$$

where the Fourier coefficients $\tilde{\chi}_N(0) = B_0$, $\tilde{\chi}_N(n) = (1/2)\,(B_n - iA_n)$ for $n \geq 1$, and $\tilde{\chi}_N(n) = (1/2)\,(B_n + iA_n)$ for $n \leq 1$. The magnitudes of the Fourier coefficients are given by $|\tilde{\chi}_N(n)| = (1/2)\sqrt{A_n^2 + B_n^2}$ for $n \geq 1$. If the magnitudes of the first few Fourier coefficients are small compared to $|\tilde{\chi}_N(0)|$, then we expect the noise power to be approximately a Lorentzian. This appears to be the case: $|\tilde{\chi}_N(1)/\tilde{\chi}_N(0)| = 0.62$ and $|\tilde{\chi}_N(2)/\tilde{\chi}_N(0)| = 0.18$.

We can explicitly calculate the noise power spectrum by substituting the analytic form of $\chi_N(\tau)$ in Eq. (3.22) into our expression for $C_N(\tau)$ in Eq. (3.15) and taking the Fourier transform. The result is shown in Fig. 3.3. Since $S_N(\omega) = S_N(-\omega)$, we plot the one-sided power spectral density for $\omega > 0$ by replacing $S_N(\omega)$ with $2S_N(\omega)$. The Lorentzian noise power resulting from keeping only the B_0 term is shown for comparison and we see that this Lorentzian is very close to the noise power obtained from keeping terms up to A_3 and B_3. At high frequencies, both power spectra go as $1/\omega^2$. Thus, we see once again that the noise spectrum is Lorentzian at frequencies lower than the lowest fluctuation frequency.

We perform another analytic calculation but instead of periodic temperature oscillations, we use a sequence of random fluctuation rates.

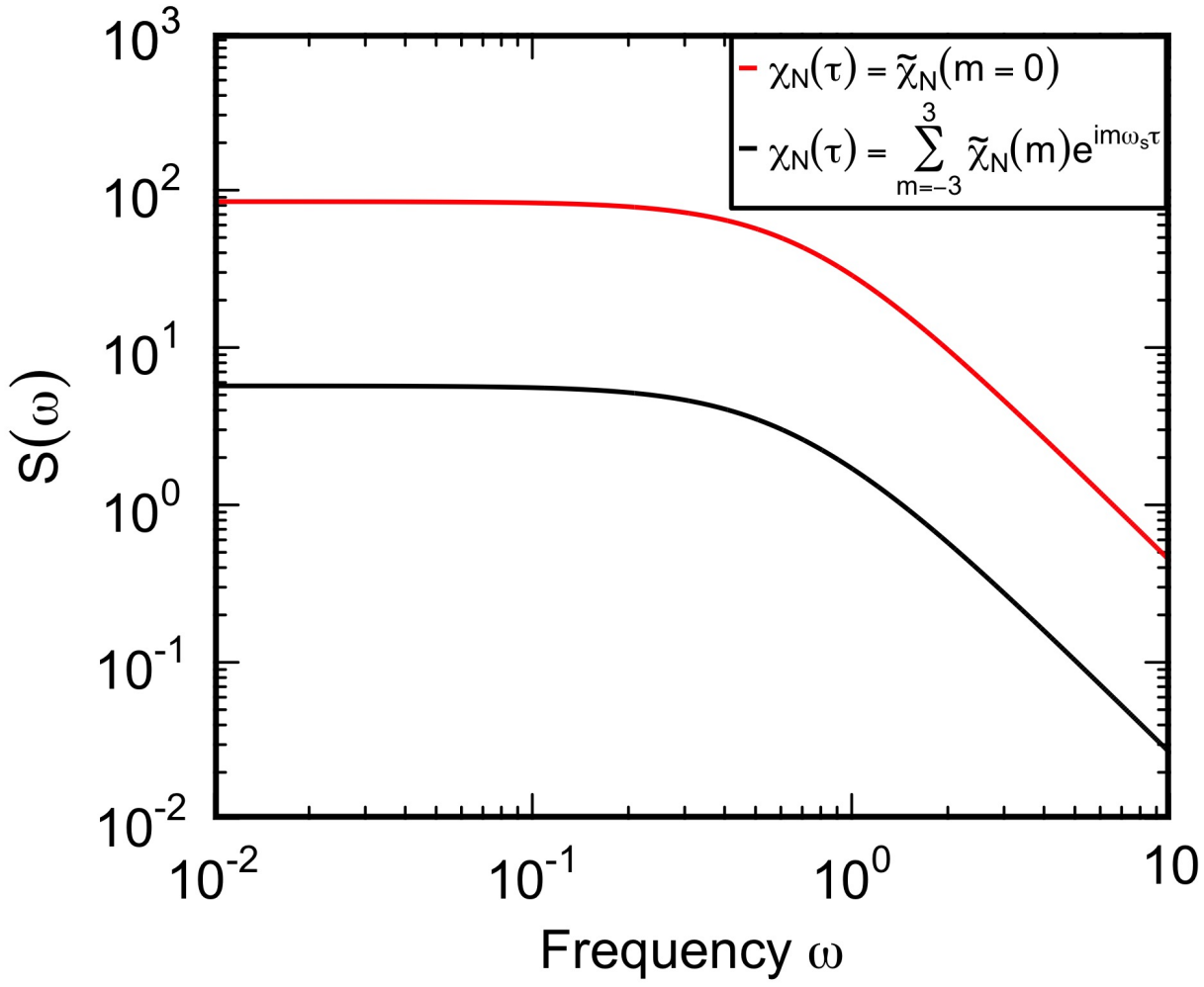

Figure 3.3: Noise power as a function of frequency for a two-level fluctuator with the parameters $U = 1$, $\epsilon = 0$, $T_0 = 1$, and $\delta T = 0.3$.

3.5 Sequence of Random Fluctuation Rates

To confirm our finding that a fluctuating temperature results in a $1/f$-like noise spectrum only when the time scale of the thermal fluctuations are longer than the inverse of the lowest frequency at which $1/f$ noise is observed, we did an analytic calculation where we consider a two state fluctuator with a time-dependent transition rate $\gamma'(t)$ between two degenerate minima at $x = 0$ and $x = 1$. The correlation function $\Psi(t) = \langle x(0)x(t)\rangle$ (where the angular brackets denote an average over realizations selected from the specified distribution) is just half of $p_1(t)$, the probability of the system being in state 1 at time t, given that it was in state 1 at $t = 0$. (The factor of 1/2 is the probability that the system is in state 1 at $t = 0$.) The equation governing the evolution of $p_1(t)$ is:

$$\frac{dp_1(t)}{dt} = -\gamma'(t)p_1(t) + \gamma'(t)p_0(t) = \gamma'(t)(1 - 2p_1(t)), \tag{3.24}$$

where $p_0(t) = 1 - p_1(t)$ is the probability that the system is in state 0 at time t and the initial condition is $p_1(0) = 1$. The solution of this equation is:

$$p_1(t) = \frac{1}{2}(1 + e^{-2\int_0^t \gamma'(t_1)dt_1}). \tag{3.25}$$

Since $\gamma'(t) > 0$, in the limit $t \to \infty$, the probability goes to 1/2 as it should in equilibrium. In the following, we rescale γ' such that $\gamma(t) = 2\gamma'$. Since we are interested in fluctuations about the mean, we define the autocorrelation function accordingly:

$$\begin{aligned} \Psi(t) &= \langle (x(0) - \langle x\rangle)(x(t) - \langle x\rangle)\rangle \\ &= \langle x(0)x(t)\rangle - 1/4 \\ &= \frac{1}{4}e^{-\int_0^t \gamma(t_1)dt_1}, \end{aligned} \tag{3.26}$$

where we used $\langle x \rangle = 1/2$.

The Fourier Transform of the correlation function, $p_1(t)/2$ is given by

$$\Psi(\omega) = \frac{1}{2}\int_0^\infty e^{-\int_o^t \gamma(t')dt'} \cos(\omega t)dt, \tag{3.27}$$

where we have used the symmetry $\Psi(t) = \Psi(-t)$. We can replace $\gamma(t)$ by a discrete sequence of constant rates such that the nth transition rate γ_n occurs during the time interval $\Delta_n = t_{n+1} - t_n$. Writing $t_n = \sum_{i=1}^n \Delta_i$, the integral Eq. (3.27) is broken into these time intervals:

$$\begin{aligned}
\Psi(\omega) &= \frac{1}{2}\int_0^\infty e^{-\int_o^t \gamma(t')dt'} \cos(\omega t)dt \\
&= \frac{1}{2}\left(\int_0^{t_1} e^{-\gamma_1 t}\cos(\omega t)dt + \int_{t_1}^{t_2} e^{-\gamma_1\Delta_1 - \gamma_2(t-t_1)}\cos(\omega t)dt + \ldots \right. \\
&\left. + \int_{t_k}^{t_{k+1}} e^{-(\sum_{i=1}^k \gamma_i\Delta_i) - \gamma_{k+1}(t-t_k)}\cos(\omega t)dt + \ldots\right) \\
&= \frac{1}{2}\sum_{k=0}^\infty e^{-(\sum_{i=1}^k \gamma_i\Delta_i)}\int_{t_k}^{t_{k+1}} e^{-\gamma_{k+1}(t-t_k)}\cos(\omega t)dt \\
&= \frac{1}{2}\sum_{k=0}^\infty e^{-(\sum_{i=1}^k \gamma_i\Delta_i)}\int_0^{\Delta_{k+1}} e^{-\gamma_{k+1}t}\cos(\omega t + \omega\sum_{i=1}^k \Delta_i)dt.
\end{aligned} \tag{3.28}$$

This can be further simplified by expressing the cosine in terms of exponentials:

$$\Psi(\omega) = \mathrm{Re}\left\{\sum_{k=0}^\infty e^{-(\sum_{i=1}^k(\gamma_i - i\omega)\Delta_i)}\int_0^{\Delta_{k+1}} e^{-(\gamma_{k+1}-i\omega)t}dt\right\}. \tag{3.29}$$

The time integral can then be performed:

$$\Psi(\omega) = \frac{1}{2}\mathrm{Re}\left\{\sum_{k=0}^\infty e^{-(\sum_{i=1}^k(\gamma_i - i\omega)\Delta_i)}\frac{1 - e^{-(\gamma_{k+1}-i\omega)\Delta_{k+1}}}{\gamma_{k+1} - i\omega}\right\}. \tag{3.30}$$

This expression for the frequency dependence of the noise must then be averaged over all possible realizations of Δ_i and γ_i which we assume to be independent, i.e., $P(\Delta_1 \ldots \Delta_n\gamma_1 \ldots \gamma_n) = P_d(\Delta_1)\cdot\ldots\cdot P_d(\Delta_n)P_g(\gamma_1)\cdot\ldots\cdot P_g(\gamma_n)$ where $P_d(\Delta_i)$ and $P_g(\gamma_i)$ are the respective distri-

butions of individual Δ_i and γ_i. We model $P_d(\Delta_i)$ as the arrival time in a queue, i.e. an exponential distribution:

$$P_d(\Delta) = \frac{1}{t_o} e^{-\Delta/t_o}, \tag{3.31}$$

where t_o is the mean duration of a given value of the relaxation rate, i.e., it is the mean time between changes in the relaxation rate. With this distribution, the average over the Δ_i's in Eq. (3.30) can be done. The average over the distribution of γ_i is left as a formal average $\langle .. \rangle_\gamma$ for now. We can rewrite $\Psi(\omega)$ in Eq. (3.29) as

$$\Psi(\omega) = \frac{1}{2} \mathrm{Re} \left\{ \sum_{k=0}^{\infty} \mu_0^k(\omega) \mu_1(\omega) \right\}, \tag{3.32}$$

where μ_o is independent of i since P_d is the same for all i as can be seen in the following expression:

$$\begin{aligned} \mu_o(\omega) &= \left\langle \frac{1}{t_o} \int_0^\infty e^{-(\gamma_i - i\omega)\Delta_i - \Delta_i/t_o} d\Delta_i \right\rangle_\gamma \\ &= \left\langle \frac{1}{1 + \gamma t_o - i\omega t_o} \right\rangle_\gamma . \end{aligned} \tag{3.33}$$

Note also that $|\mu_0(\omega)| < 1$. The average in $\mu_1(\omega)$ is given by:

$$\begin{aligned} \mu_1(\omega) &= \left\langle \frac{1}{\gamma_{k+1} - i\omega} \left(1 - \frac{1}{t_o} \int_0^\infty e^{-(\gamma_{k+1} - i\omega)\Delta_{k+1} - \Delta_{k+1}/t_o} d\Delta_{k+1} \right) \right\rangle_\gamma \\ &= \left\langle \frac{1}{\gamma - i\omega} \left(1 - \frac{1}{1 + \gamma t_o - i\omega t_o} \right) \right\rangle_\gamma \\ &= \left\langle \frac{t_o}{1 + \gamma t_o - i\omega t_o} \right\rangle_\gamma \\ &= t_o \mu_0(\omega) \end{aligned} \tag{3.34}$$

which is independent of k. The geometric sum can now be carried out:

$$\begin{aligned}\Psi(\omega) &= \frac{t_o}{2}\mathrm{Re}\left\{\sum_{k=0}^{\infty}\mu_0^k(\omega)\mu_0(\omega)\right\} \\ &= \frac{t_o}{2}\mathrm{Re}\left\{\frac{\mu_0(\omega)}{1-\mu_o(\omega)}\right\} \\ &= \frac{t_o}{2}\cdot\frac{\mu_0^{'}(\omega)-(\mu_0^{'}(\omega))^2-(\mu_0^{''}(\omega))^2}{1-2\mu_0^{'}(\omega)+(\mu_0^{'}(\omega))^2+(\mu_0^{''}(\omega))^2},\end{aligned} \tag{3.35}$$

where we have used the definition $\mu_i(\omega) = \mu_i^{'}(\omega) + i\mu_i^{''}(\omega)$. Explicit formulas for μ_0 from Eq. (3.33) for a discrete distribution of relaxation rates specified by m values $\gamma_1 \ldots \gamma_m$, equally weighted for simplicity, are:

$$\mu_0^{'}(\omega) = \frac{1}{m}\sum_l \frac{1+\gamma_l t_o}{(1+\gamma_l t_o)^2+(\omega t_o)^2} \tag{3.36}$$

and

$$\mu_0^{''}(\omega) = \omega t_o \frac{1}{m}\sum_l \frac{1}{(1+\gamma_l t_o)^2+(\omega t_o)^2}, \tag{3.37}$$

where the sum over l runs from 1 to m. Eq. (3.35) together with Eqs. (3.36) and (3.37) is the main result of this section. It is a bit difficult to see the overall behavior in this expression since it depends on the values chosen for the γ_l in the formulas for the averages entering the power spectra. However, the limit $t_o \to \infty$ is easy to obtain and gives

$$\Psi(\omega) = \frac{1}{2m}\sum_l \frac{\gamma_l}{\omega^2+\gamma_l^2} \tag{3.38}$$

which is the quenched limit. With appropriate values for γ_l, this easily produces a $1/\omega$ noise spectrum spanning decades in frequency.

More insight requires the specification of values for γ_l. Choosing γ_l to be $\gamma_l = 2^l$ where $l = -10, -9, \ldots, 7, 8$, gives a fairly good approximation to a $1/\omega$ noise power spectrum over

several decades in frequency when averaging over the Lorentzian noise spectra for each γ_l; this is the quenched limit. Fig. 3.4 shows the resulting spectra for a large $t_o = 10^4$ (black line) which is indistinguishable from the quenched average and can be seen to follow a $1/\omega$ power law (red line). At a much shorter switching time of $t_o = 20$ (blue line), the power spectra turns flat at low frequencies sooner, when going from high to low frequencies, than in the quenched limit. One can see a short range of frequencies where the power spectra goes roughly as $1/\omega$ before going over to $1/\omega^2$ when ω exceeds the largest rate.

A continuous distribution for γ can also be considered. For instance, $p_1(\gamma) = \lambda^{-1}/\gamma$ with $\lambda = \ln(\gamma_{\max}/\gamma_{\min})$ and $\gamma_{\min} < \gamma < \gamma_{\max}$ will give a $1/\omega$ spectrum in the quenched limit. Using this distribution instead of the sums in Eqs. (3.36) and (3.37) yields:

$$\begin{aligned} \mu_0^{'}(\omega) &= D(\omega) - \omega t_o E(\omega) \\ \mu_0^{''} &= \omega t_o D(\omega) + E(\omega) \end{aligned} \tag{3.39}$$

with

$$\begin{aligned} D(\omega) &= \frac{2\lambda - B(\omega)}{2\lambda C(\omega)} \\ E(\omega) &= \frac{A(\omega)}{2\lambda C(\omega)} \end{aligned} \tag{3.40}$$

$$A(\omega) = 2\left(\arctan\left(\frac{\gamma_{\min} t_o + 1}{\omega t_o}\right) - \arctan\left(\frac{\gamma_{\max} t_o + 1}{\omega t_o}\right)\right) \tag{3.41}$$

$$B(\omega) = \ln\left(\frac{\omega^2 t_o^2 + \gamma_{\max}^2 t_o^2 + 2\gamma_{\max} t_o + 1}{\omega^2 t_o^2 + \gamma_{\min}^2 t_o^2 + 2\gamma_{\min} t_o + 1}\right) \tag{3.42}$$

and

$$C(\omega) = \omega^2 t_o^2 + 1. \tag{3.43}$$

A plot of the power spectra is shown in Fig. 3.5 for $\gamma_{\min} = 10^{-6}$ and $\gamma_{\max} = 10^6$. The black curve corresponds to a mean time of $t_o = 10^8$ between rate changes. At frequencies below the lowest rate in the system, 10^{-6}, the noise becomes flat. At frequencies higher than the largest rate, the response goes over to $1/\omega^2$. The magenta curve shows the effect of a faster mean switching time of 1000, flattening at frequencies below $\omega \cdot 1000 \sim 1$, instead of at the slowest rate of 10^{-6}. At the still lower mean switching time of 1, shown by the blue curve, the crossover occurs at higher frequencies, again dictated by $\omega t_o \sim 1$.

The overall behavior of the system is best seen with the limit $\gamma_{\max} t_o \gg 1$ and $\gamma_{\min} t_0 \ll 1$. This eliminates the $1/\omega^2$ behavior at high frequencies as well as the low frequency flattening of the noise. In that limit, $A(\omega)$ reduces to $-2\arctan(t_o\omega)$. $B(\omega)$ has a logarithmic dependence on ω and is small so it can be neglected entirely. This removes minor details of the frequency dependence of the noise. The expression for the power spectra is then greatly simplified:

$$\Psi(\omega) \sim \frac{1}{2}\frac{t_o \arctan(\omega t_o)/\lambda}{\omega t_o - \arctan(\omega t_o)/\lambda} \sim \frac{\arctan(\omega t_o)}{2\lambda\omega}. \tag{3.44}$$

Now in the limit $\omega t_o \gg 1$, $\Psi(\omega) \to \pi/(4\lambda\omega)$. In this regime, the power spectra goes as $1/\omega$. In the limit $\omega t_o \ll 1$, the noise becomes independent of frequency, i.e., $\Psi(\omega) \to t_o/(2\lambda)$. The crossover between these two behaviors occurs around $\omega t_o \sim 1$ as expected. $\Psi(\omega)$, as approximated by Eq. (3.44), is shown in Fig. 3.6 for a few values of t_o.

Thus we see that in order to observe $1/f$ noise in a given frequency range, the average duration t_o of a fluctuation rate must exceed the inverse frequency of the lower limit of that range.

As a point of reference, we can put the rates used by Ahn *et al.* [2] into our formulation Eq. (3.35). Ahn *et al.* assumed thermally activated rates:

$$\gamma = \frac{1}{\tau} e^{-\frac{E}{k_b T_{\rm sb}}} \tag{3.45}$$

with a sub-bath temperature distribution $T_{\rm sb}$ given by a Gaussian that was truncated to remove negative temperatures:

$$f(T_{\rm sb}, T_{\rm avg}, \sigma_{\rm sb}) = \xi \frac{e^{-(T_{\rm sb}-T_{\rm avg})^2/2\sigma_{\rm sb}^2}}{\sqrt{2\pi}\sigma_{\rm sb}}, \tag{3.46}$$

where $T_{\rm avg}$ is the average sub-bath temperature, $\sigma_{\rm sb}^2$ the variance, and ξ is a normalization factor that accounts for the truncation of the Gaussian. With the parameters used in this section, $\xi \sim 1$. Here we adopt Ahn's notation (except that we use $T_{\rm avg}$ rather than T). Eq. (3) of Ahn *et al.* [2], written in terms of rates, is

$$\frac{S(\omega)}{\Delta^2 \tau} = \int_0^\infty f(T_{\rm sb}, T_{\rm avg}, \sigma_{\rm sb}) \frac{2\tilde{\gamma}}{\omega^2\tau^2 + \tilde{\gamma}^2} dT_{\rm sb}, \tag{3.47}$$

where $\tilde{\gamma} = \exp(-E/k_b T_{\rm sb})$. Δ is the total variance of the signal produced by the switching events. Since our fluctuator jumps between $x = 0$ and $x = 1$, $\Delta^2 = 1/4$. Note that Δ is not the time interval that the system is at a given temperature; this use of Δ differs from that used earlier. Our Eq. (3.47) differs from Ahn's Eq. (3) by a factor of 2 which is likely due to Ahn's folding of the power spectra, i.e., Ahn assumes that the frequency is positive and includes the negative frequencies by multiplying the power spectrum by 2. We can explicitly

include these quantities in Eq. (3.47):

$$\frac{S(\omega)}{\Delta^2\tau} = \int_0^\infty \xi \frac{e^{-(T_{\rm sb}/T_{\rm avg}-1)^2/2(\sigma_{\rm sb}/T_{\rm avg})^2}}{\sqrt{\pi/2}\sigma_{\rm sb}} \cdot \frac{2e^{-\frac{E}{k_b T_{\rm avg}}\frac{T_{\rm avg}}{T_{\rm sb}}}}{\omega^2\tau^2 + (e^{-\frac{E}{k_b T_{\rm avg}}\frac{T_{\rm avg}}{T_{\rm sb}}})^2} dT_{\rm sb}. \tag{3.48}$$

A change of integration variable from $T_{\rm sb}$ to $y = T_{\rm sb}/T_{\rm avg}$ gives:

$$\frac{S(\omega)}{\Delta^2\tau} = 4\int_0^\infty f(y,1,\tilde{\sigma}_{\rm sb}) \frac{2e^{-a/y}}{\omega^2\tau^2 + \left(e^{-a/y}\right)^2} dy, \tag{3.49}$$

where $\tilde{\sigma}_{\rm sb} = \sigma_{\rm sb}/T_{\rm avg}$ and $a \equiv E/k_b T_{\rm avg}$. This expression from Ahn *et al.* [2] differs from our definition of the noise used in Eq. (3.35) by a factor 2 due to a difference in normalization factors between Ahn *et al.* and us. Ahn *et al.* assumed that each temperature lasts for an infinite amount of time, i.e., $t_o = \infty$. We can generalize Eq. (3.49) to include a finite duration for temperature fluctuations by using Eq. (3.35) which includes the factor $\Delta^2 = 1/4$:

$$\frac{S(\omega)}{\Delta^2\tau} = 2t_o \cdot \frac{\mu_0^{'}(\omega) - (\mu_0^{'}(\omega))^2 - (\mu_0^{''}(\omega))^2}{1 - 2\mu_0^{'}(\omega) + (\mu_0^{'}(\omega))^2 + (\mu_0^{''}(\omega))^2} \tag{3.50}$$

with:

$$\mu_0^{'}(\omega) = \int_0^\infty f(y,1,\tilde{\sigma}_{\rm sb}) \frac{1 + t_o e^{-a/y}}{(1 + t_o e^{-a/y})^2 + (\omega t_o)^2} dy \tag{3.51}$$

$$\mu_0^{''}(\omega) = \omega t_o \int_0^\infty f(y,1,\tilde{\sigma}_{\rm sb}) \frac{1}{(1 + t_o e^{-a/y})^2 + (\omega t_o)^2} dy \tag{3.52}$$

with t_o and $1/\omega$ measured in units of τ. Using the above equations with the values of Ahn *et al.*, namely, $a = E/k_b T_{\rm avg} = 1$ and $\tilde{\sigma}_{\rm sb} = 0.3$, the effect of finite temperature fluctuations lifetimes is shown in Fig. 3.7. The noise for $t_o = 10^{12}$ is indistinguishable from the quenched limit $t_o \to \infty$ shown in Fig. 1 of Ahn *et al.* [2] in the frequency range displayed. We see that shorter average durations of the temperature cause the curves to flatten off at higher

frequencies where $\omega t_o \sim 1$. This reiterates our finding that low frequency $1/f$ noise requires very slow fluctuations. In the next section, we make estimates to see if this is physically reasonable in a 2DEG where Ahn *et al.* [2] assumed there would be temperature fluctuations in a sub-bath.

3.6 Estimate of Thermal Relaxation Time Due to Diffusion

Experimentally measured charge noise exhibits $1/f$ behavior down to 1 Hz and even lower frequencies [18], implying that if thermal fluctuations play an important role, the relaxation time of these thermal fluctuations must be significantly longer than the relaxation time of the fluctuators coupled to the quantum dots, i.e., the thermal fluctuations must last at least a few seconds or longer. To see whether this is reasonable, we can estimate the duration of temperature fluctuations in the 2DEG. Temperature fluctuations in a sub-bath imply spatial inhomogeneities in the temperature of 2DEG. Thermal diffusion would smooth out these inhomogeneities. Long-lived fluctuations are difficult to achieve in typical electronic systems without some kind of activated behavior. An exception exists when a quantity satisfies a conservation law. Then long relaxation times can exist for large scale fluctuations. This possibility was investigated by Voss and Clark [50] for energy fluctuations (equivalently temperature fluctuations via $\Delta E = C_v \Delta T$ where C_v is the heat capacity in metal films). Since the slowest relaxation occurs for the largest spatial fluctuations, the dimensions of the system introduce key frequencies in the problem: $f_i = D/(\pi l_i^2)$ where D is the thermal diffusion constant and l_i, with $i = x, y, z$, are the dimensions of the system. There are no fluctuations that will last longer than $1/f_i$ and therefore all that is needed is to evaluate f_i for the largest dimension which is about 1 μm for the 2DEG in the work of Connors et al. [18]. (In [50], the dimensions of the conductor were quite large, of the order of millimeters, and

together with a diffusion constant equal to $D \sim 2 \cdot 10^{-5}$ m^2/s, produced minimal frequencies of the order of 1 Hz or less.) To estimate the lowest frequency in the present system, the diffusion constant D must be evaluated at low temperatures for the 2DEG. In what follows, the diffusion constant is expressed in terms of quantities measured in the Si/SiGe 2DEG of ref. [18].

In a diffusive regime (which is assumed to be the case here), the diffusion constant D is related to the thermal conductivity κ via

$$D = \frac{\kappa}{C}, \tag{3.53}$$

where κ is the thermal conductivity in W/K (in two dimensions) and C is the specific heat in J/(K $\cdot$ m^2). For the 2DEG, the specific heat is given by [2]

$$C = \frac{\pi m k_b^2 T}{3\hbar^2}, \tag{3.54}$$

where the carrier's mass is $m = 0.19 m_e$ and m_e is the mass of the electron.

The thermal conductivity is rarely available experimentally. Using the Wiedemann–Franz law, it is possible to relate the thermal conductivity to the electric conductivity σ:

$$\frac{\kappa}{\sigma T} = \frac{\pi^2}{3}\left(\frac{k_b}{e}\right)^2, \tag{3.55}$$

where e is the electric charge. The final piece is to compute the electrical conductivity which is given by

$$\sigma = e \cdot n \cdot \mu, \tag{3.56}$$

where n is the carrier number density and μ is the carrier mobility which is usually available.

Combining Eqs. (3.53), (3.54), (3.55), and (3.56) gives the diffusion constant in terms of measured quantities:

$$D = \frac{\pi n \mu \hbar^2}{em}. \tag{3.57}$$

Using the values $n = 2.2 \cdot 10^{15}$ 1/m^2 and $\mu = 16$ m^2/(Volt s) reported in ref. [51], Eq. (3.57) gives $D = 1.4 \cdot 10^{-2}$ m^2/s. Using this value for D, we estimate the lowest frequency in the problem to be

$$f_{\min} = \frac{D}{\pi l^2} = \frac{1.4 \cdot 10^{-2}}{\pi (10^{-6})^2} \text{ Hz} = 4.5 \text{ GHz}. \tag{3.58}$$

It is therefore highly unlikely that a 2DEG bath can satisfy the assumption underlying the calculation of Ahn *et al.* [2].

We can obtain a slightly different estimate in a different 2DEG (AlN/GaN) system where the Wiedemann-Franz law was verified [52]. This paper measured the specific heat as well as thermal and electrical conductivity of the 2DEG. The thermal conductivity has the form $\kappa = 90T/275$ W/(K m) (where T is temperature) while the specific heat is $C = 0.05T$ in J/(kg K). (Note that the units are appropriate for 3D quantities; the paper [52] measured the thickness of the electron gas for the conversion.) The diffusion constant is then $D = \kappa/\rho C$ where ρ is the density of the material (GaN) and is equal to 6150 kg/m^3. The temperature dependences cancel out and the diffusion constant is found to be approximately 10^{-3} m^2/s. This value is slightly smaller than what has been estimated for the Si/SiGe case but does not change the conclusion.

Finally, the diffusion constants obtained above are significantly larger than those used by Voss and Clarke in the context of metal thin films ($D \sim 2 \cdot 10^{-5}$ m^2/s). However, even with such a diffusion constant, the conclusion remains unchanged (the lowest frequency drops to 6 MHz).

3.7 Conclusions

We have considered a quantum dot whose charge noise is determined by a fluctuator coupled to a thermal bath with a fluctuating temperature. To determine the noise spectrum of this two-level fluctuator, we have performed Monte Carlo simulations of an anisotropic Heisenberg spin and an Ising spin in a fluctuating temperature bath. We have also used analytic calculations of a two-state fluctuator with periodic temperature oscillations and calculations of a two-state fluctuator with random switching rates. We find that a $1/f$ noise spectrum at a given frequency f_0 requires that the frequencies of the thermal fluctuations must be comparable to f_0. However, our estimate of the lowest temperature fluctuation frequency is a few GHz in a 2DEG which is inconsistent with $1/f$ noise observed at frequencies below 1 Hz. In short, to obtain $1/f$ noise that extends over several decades in frequency from a model based on temperature fluctuations requires fluctuations with an unphysically long duration.

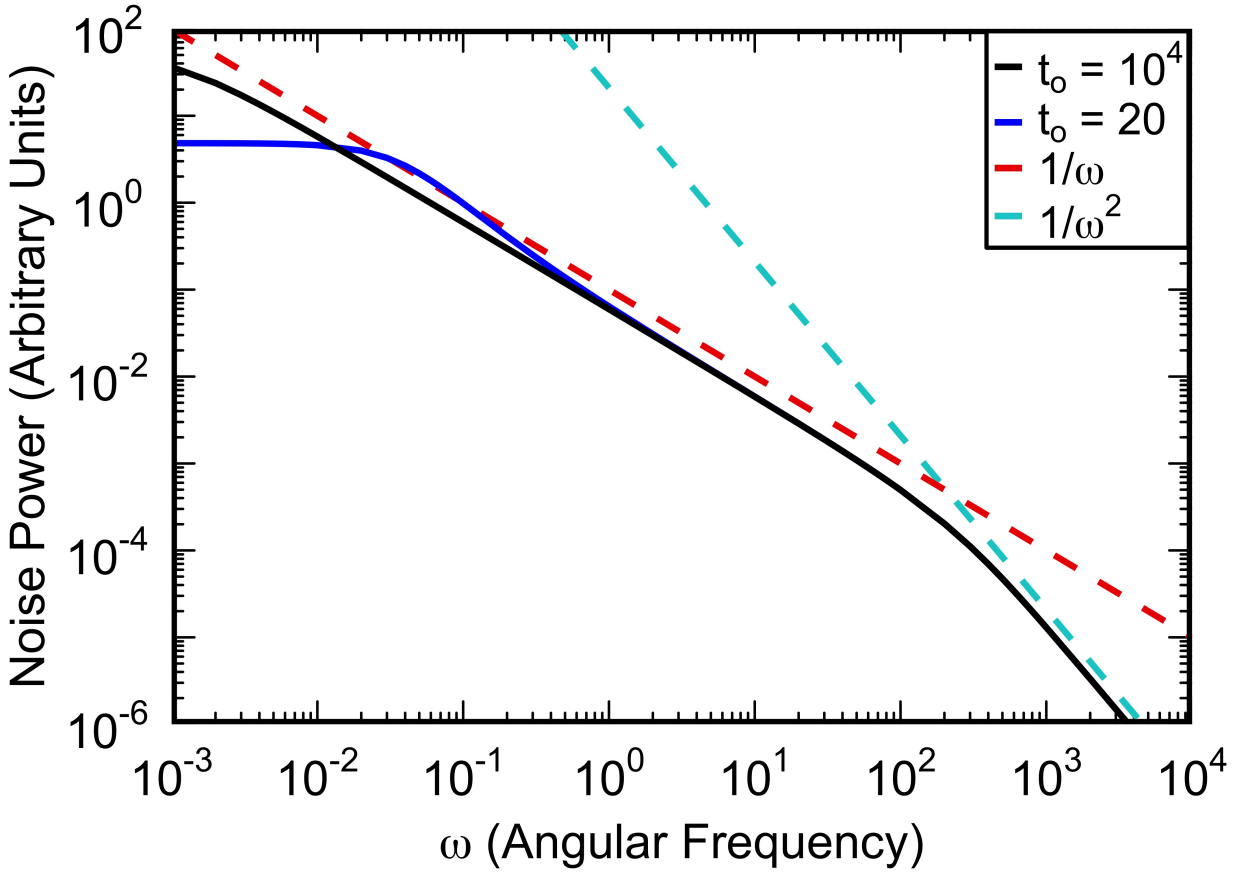

Figure 3.4: Comparison of noise spectra on the time scale on which the transition rates vary, obtained using the analytic theory. The plot shows the noise power vs. angular frequency on a log-log plot with a rate change on average every $t_o = 20$ (blue solid line) and every $t_o = 10^4$ (black solid line). Straight dashed lines are guides to the eye. The red dashed line corresponds to $1/\omega$ and the cyan dashed line corresponds to $1/\omega^2$. The discrete distribution of γ is discussed in the text. The $1/f$-like behavior of the spectrum is cut off at frequencies below $1/t_0$.

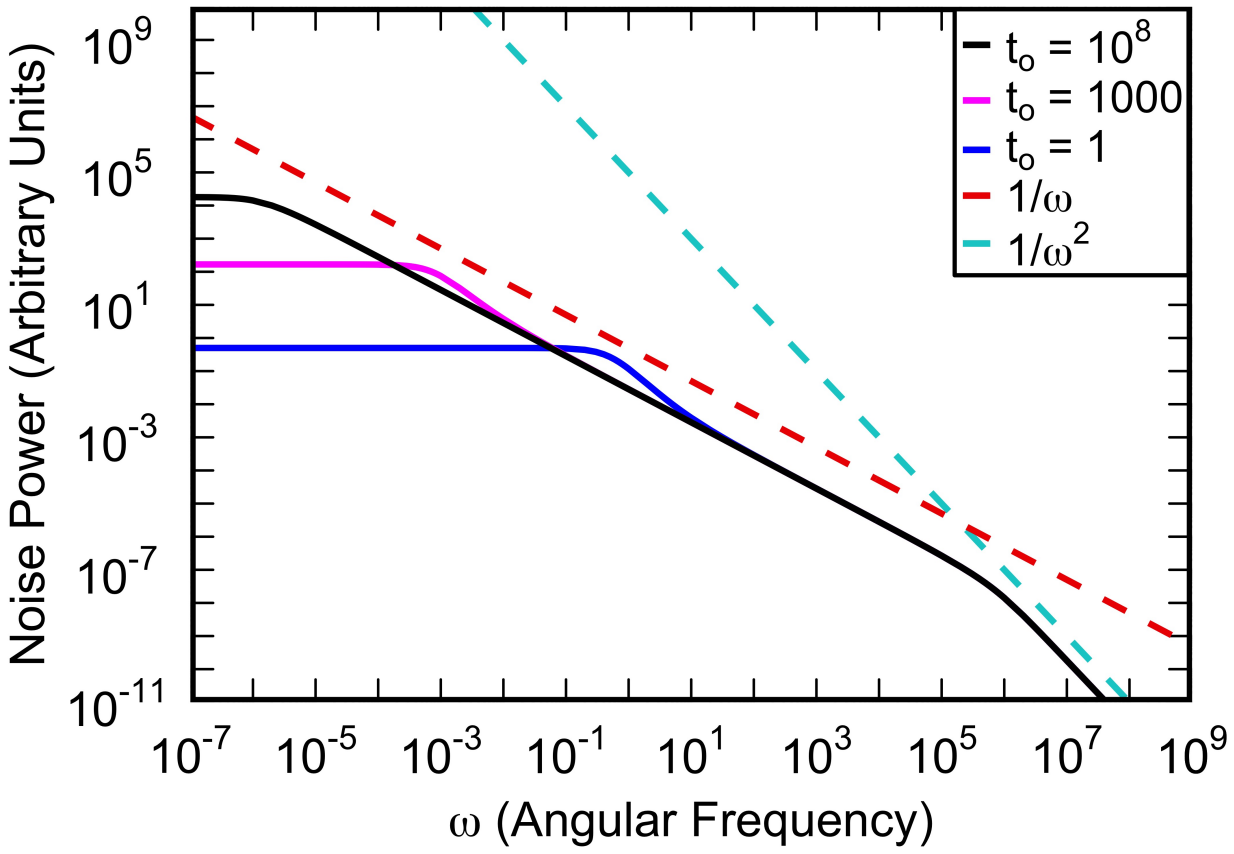

Figure 3.5: Noise power spectra vs. angular frequency on a log-log plot for a continuous distribution of rates with a rate change on average every $t_o = 10^8$ (black), $t_o = 1000$ (magenta), and $t_o = 1$ (blue) respectively. $\gamma_{\min}$ is 10^{-6} and $\gamma_{\max}$ is 10^6. Straight dashed lines are guides to the eye. The red dashed line goes as $1/\omega$ and the cyan dashed line goes as $1/\omega^2$. The spectrum is $1/f$-like at intermediate frequencies when the characteristic time t_0 describing the rate variations is long, so that $\max[\gamma_{\min}, 1/t_0] \ll \omega \ll \gamma_{\max}$.

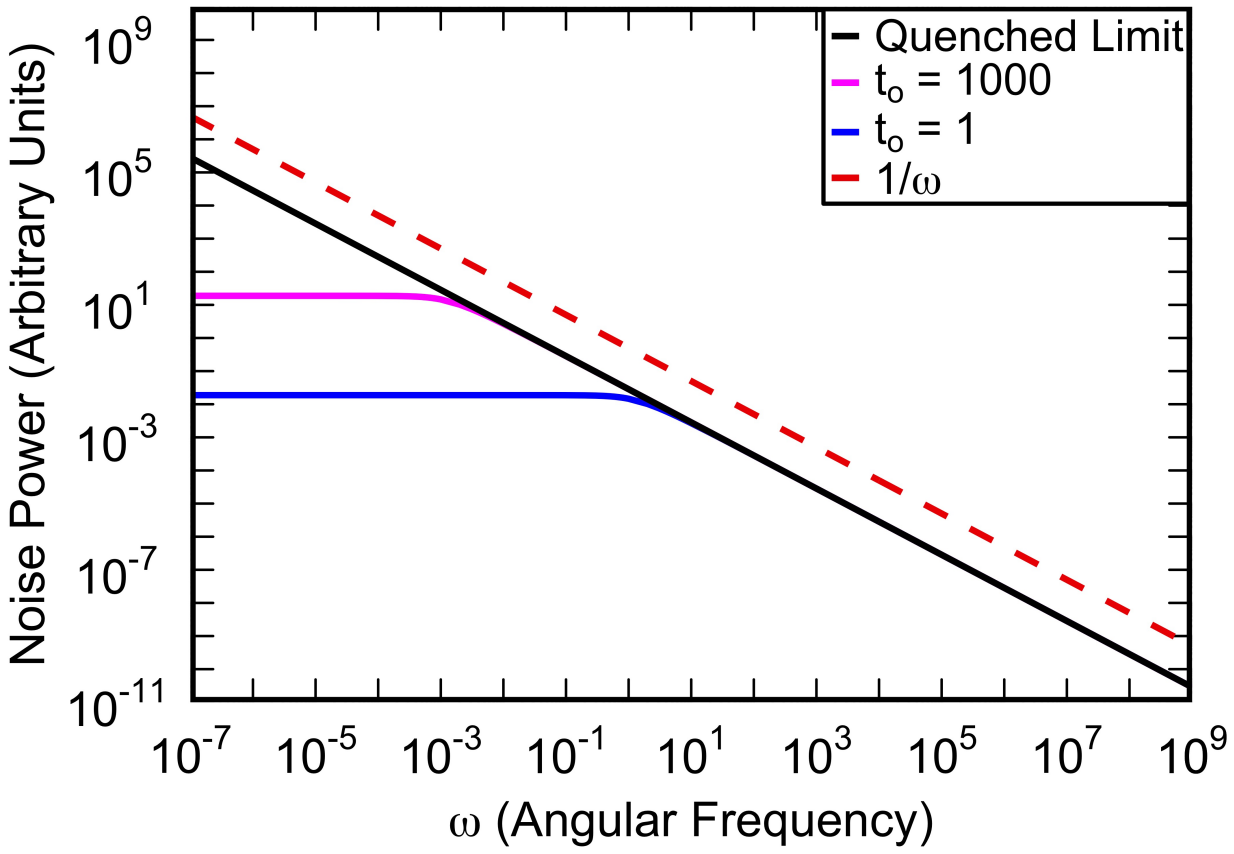

Figure 3.6: Approximate noise spectra for a continuous distribution of rates, obtained from Eq. (3.44). The quenched limit ($t_o \to \infty$) is shown in black, the magenta line corresponds to a rate change on average every $t_o = 1000$, and the blue line corresponds to $t_o = 1$. $\lambda = \log(\gamma_{\max}/\gamma_{\min}) = \log(10^{12})$. The straight red dashed line is proportional to $1/\omega$.

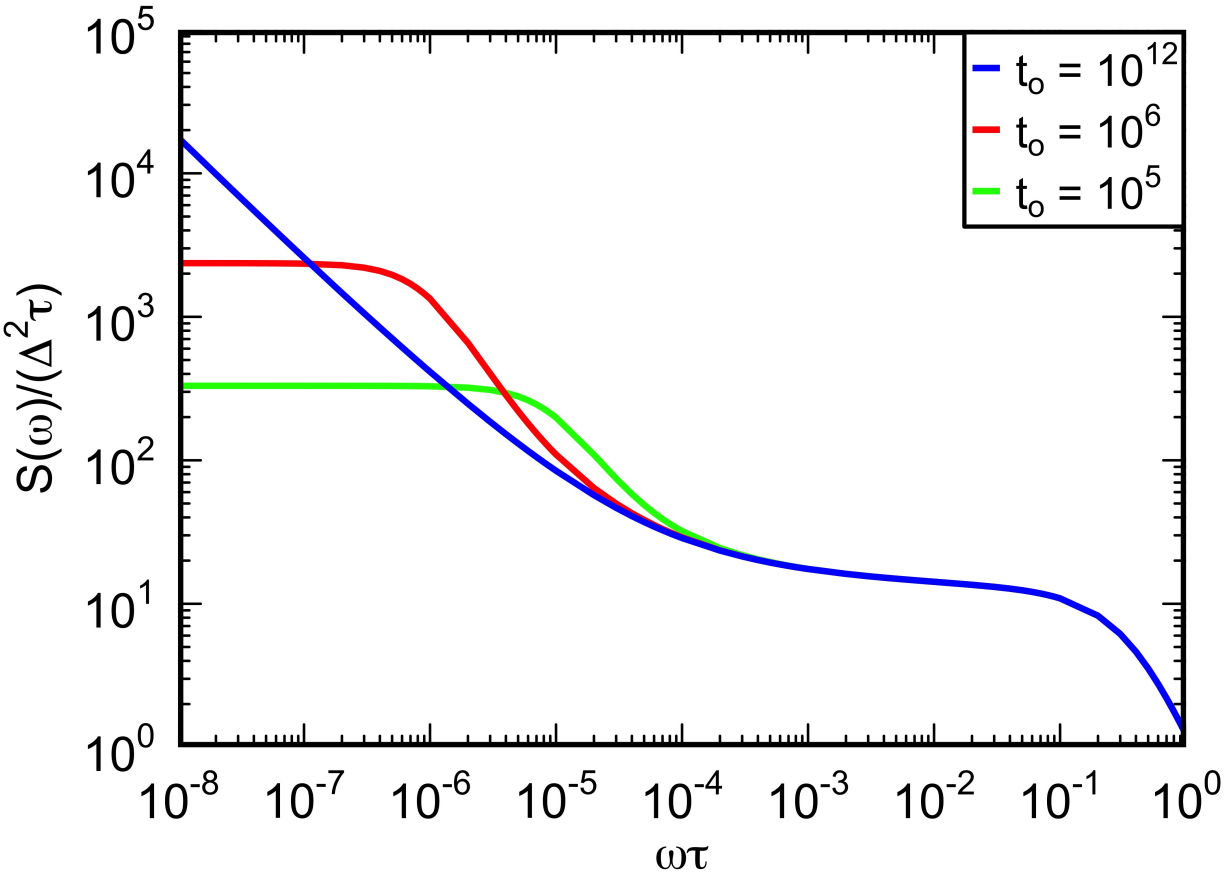

Figure 3.7: Noise power spectra vs. $\omega\tau$ on a log-log plot for three different average switching times: $t_o = 10^{12}$ (blue), $t_o = 10^6$ (red), and $t_o = 10^5$ (green). These plots show the effect of finite temperature fluctuations lifetimes on the noise spectra of Ahn *et al.*.

Chapter 4

Interacting Two-Level Systems as a Source of $1/f$ Noise in Silicon Quantum Dot Qubits

4.1 Introduction

Electron spins in Si/SiGe quantum dots (QDs) show promise as quantum bits, but are plagued by charge noise that goes as $1/f^{\alpha}$ over more than thirteen decades in frequency [42], where f is the frequency and α is the noise exponent. $1/f$ noise is typically attributed to a bath of two-level fluctuators with a broad distribution of switching rates. If each fluctuator is associated with a double well potential, then thermal activation over a uniform distribution of barrier heights produces $1/f$ noise [29, 46]. With such a bath of two level systems (TLS), one would expect the charge noise to increase linearly with increasing temperature [44]. However, the measured temperature dependence increasingly deviates from linearity with increasing thickness of the gate oxide layer [18, 53] and, in another study, was found to be

quadratic [54].

The small size of the quantum dot and the lack of temperature dependence between 0.45 K and 1.2 K in the decoherence time T_2^* [44] have led some to argue that each quantum dot is only coupled to a few fluctuators [2, 55]. This view was supported by the lack of correlation in the charge noise of neighboring quantum dots [18, 53], though more direct, subsequent measurements find that there are correlations between the charge noise in quantum dots that are about 100 nm apart [45]. With only a few two-level fluctuators, a Lorentzian power spectra is expected instead of the observed $1/f$ noise.

It has been suggested that a few two-level fluctuators can produce $1/f$ noise if they are coupled to a microscopic subsection of the larger thermal bath. Temperature fluctuations in the subsection of the 2D electron gas (2DEG) cause $1/f$ noise over several decades of frequency, but this model requires that the temperature fluctuations be extremely slow, i.e., the sub-bath would need to remain at a single temperature for unphysically long periods of time [2].

Here, we propose that the charge noise arises from a bath of TLS with fluctuating electric dipole moments that reside outside the 2DEG, e.g., in the oxide layer [56]. These TLS interact with one another via elastic and electric dipole moments, though the elastic interactions dominate. (Elastic dipole-dipole inteactions are about an order of magnitude larger than electric dipole-dipole interactions [57].) The TLS energy level splittings change with time due to interactions with their fluctuating TLS neighbors. This bath of fluctuating electric dipole moments, together with their image charges in the ground plane lying below the metal gates, produces $1/f$ noise in the electric potential seen by the quantum dots (QDs) consistent with the observed $1/f$ charge noise [42]. We find that the noise on the quantum dots is mildly correlated in agreement with experiment [45].

In the next section we describe our model of two quantum dots in a quantum well located

below an oxide layer containing a 2D bath of TLS that have both elastic and electric dipole moments. A Monte Carlo simulation of a 2D nearest-neighbor Ising spin glass is used to represent the TLS interacting via the elastic strain field. When an Ising spin flips, this represents a flip of the elastic dipole moment and the associated electric dipole moment follows along by also flipping. The metallic gates that cover the surface of the device are treated as a ground plane with image charges corresponding to the images of the TLS electric dipole moments. The fluctuating dipole moments and their images produce a fluctuating electric potential at the quantum dots that results in $1/f$ charge noise. We go on to calculate the correlations in the noise at the two quantum dots. These results are presented in section 4.3.

4.2 Model

In this section, we describe our model that reflects the experimental setup of a pair of quantum dots that are about 100 nm apart in a quantum well coupled to a bath of TLS with both elastic and electric dipole moments residing in the oxide layer about 30 nm above the quantum well. A set of metal gates lies on top of the oxide layer and are represented by a metal ground plane. The TLS electric dipole moments have image charges in the ground plane; both the electric dipole moments and the image charges contribute to the fluctuating electric potential at the quantum dots.

Two-level systems have long been used to describe the thermal and acoustic properties of amorphous materials at low temperatures [58, 59]. The standard TLS model postulates the existence of independent entities that tunnel between the two minima of a double well potential with a flat distribution of tunnel barrier heights and energy asymmetries [60, 61]. Using a right-well left-well basis, the Hamiltonian representing a given TLS is

$$H_{\mathrm{TLS}} = \frac{1}{2}\left(\Delta\sigma_z + \Delta_o\sigma_x\right), \tag{4.1}$$

where σ_x and σ_z are Pauli matrices, Δ is the TLS asymmetry energy, i.e., the energy difference between the right and left wells, and Δ_o is the tunneling matrix element. The values of these parameters are assumed to vary from TLS to TLS according to the probability distribution:

$$P(\Delta, \Delta_o) = \frac{\overline{P}}{\Delta_o} \tag{4.2}$$

with $0 < \Delta < \Delta_{\max}$ and $\Delta_{o,\min} < \Delta_o < \Delta_{o,\max}$. $\overline{P}$ is the constant density of states of tunneling entities. The energy eigenvalues of a given TLS are

$$\pm\frac{1}{2}E = \pm\frac{1}{2}\sqrt{\Delta^2 + \Delta_o^2}. \tag{4.3}$$

Thus the energy splitting between the two levels is E.

TLS interact with electric and elastic fields. The Hamiltonian describing the interactions of a TLS with these fields is given by

$$H_{int} = \vec{p} \cdot \vec{E}\sigma_z + \gamma\epsilon\sigma_z, \tag{4.4}$$

where $\vec{p}$ is the electric dipole moment of the TLS, $\vec{E}$ is the electric field, and γ is the coupling of the TLS to the elastic strain field ϵ.

Experimental and theoretical work indicate that TLS interact with each other via the elastic strain field [62–64]. If the TLS have electric dipole moments, then they can also interact via electric fields. However, for reasonable values of the electric dipole moments, the electric dipole-dipole interaction is about an order of magnitude smaller than the elastic dipole-dipole interactions [57]. For example, for $(KBr)_{1-x}(KCN)_x$, the elastic coupling between two CN^- ions is approximately 8×10^3 K $\mathring{A}^3$ compared to $p^2 \sim 7 \times 10^2$ K $\mathring{A}^3$, where the CN^- dipole moment is $p \sim 0.3$ D [57]. (By coupling, we are referring to the prefactor for the $1/r^3$ dipole

term in the Hamiltonian.)

By integrating out the strain field, one can write the interacting Hamiltonian as [65, 66]:

$$H = \frac{1}{2}\sum_{i\neq j}\sigma_i^z \Lambda_{ij}\sigma_j^z. \tag{4.5}$$

Here Λ_{ij} is given (in simplified form) by:

$$\Lambda_{ij} = \left(\frac{\gamma^2}{\rho v^2}\right)\frac{s_i s_j}{r_{ij}^3}, \tag{4.6}$$

where ρ is the density of the material, v is the speed of sound, r_{ij} is the distance between TLS i and j, and $s_i = \pm 1$ is a spin representation of the orientation of the elastic dipoles (see [65] for the full expressions). We can rewrite the Hamiltonian in terms of local fields produced by the neighboring TLS:

$$H = \sum_i h_i \sigma_i^z, \tag{4.7}$$

where

$$h_i = \sum_{j\neq i}\Lambda_{ij}s_j^z. \tag{4.8}$$

Fluctuations in the neighboring TLS, i.e., flips in s_j, produce fluctuations the local field and hence in the energy splitting of the ith TLS. This leads to relaxation times that vary in time since the TLS relaxation rate is given by [58, 59]:

$$\tau^{-1} = \frac{\gamma^2}{\rho}\left[\frac{3}{v^5}\right]\frac{E^3}{2\pi\hbar^4}\left[\frac{\Delta_o}{E}\right]^2 \coth\left(\frac{\beta E}{2}\right), \tag{4.9}$$

where $\beta = 1/k_B T$ is the inverse temperature. As a result, there will be a broad distribution of relaxation times that can produce $1/f$ noise.

However, it is the electric dipole moments, not the elastic dipole moments, that couple to quantum dots and give rise to charge noise. We assume that when a TLS tunnels from one well to the other, both its elastic and electric dipole moments flip. This results in fluctuations in the elecric potential $V(t)$ seen by the QDs. Since there is a metal ground plane, both the electric dipole moments $\vec{p}$ and their image charges will contribute to $V(t)$ which is given by

$$V_\zeta(t) = \sum_{\eta=1}^{2} \sum_{i=1}^{N} \frac{\vec{p}_{\eta,i}(t) \cdot \hat{R}_{\eta,i,\zeta}}{R^2_{\eta,i,\zeta}}, \tag{4.10}$$

where $\zeta = 1, 2$ denotes the QD, the sum over i corresponds to summing over TLS (denoted by $\eta = 1$) and their images (denoted by $\eta = 2$). $R_{\eta,i,\zeta}$ is the distance between the electric dipole and the ζth quantum dot and $\hat{R}_{\eta,i,\zeta}$ is a unit vector that points from the dipole to the ζth quantum dot.

We represent the TLS electric dipoles by a 2D square lattice of dipoles that are randomly oriented. We set the magnitudes of each dipole moment to unity. The mirror images of these electric dipoles in the ground plane form a second 2D square lattice. The dynamics of the TLS is governed by their elastic interactions which we model very simply with a 2D nearest neighbor Ising spin glass on a square lattice. Each Ising spin represents a TLS elastic dipole. When the Ising spin (elastic dipole) flips, its corresponding electric dipole moment, as well as its image electric dipole moment, flips 180^o. In some sense the Ising spin is an avatar or proxy for the electric dipole moment. Flips of electric dipoles and their images will change the electric potential $V_i(t)$ seen by the ith quantum dot and given by Eq. (4.10). The time series of $V_i(t)$ is Fourier transformed to produce the charge noise power spectrum.

For the purposes of our simulation, it does not matter whether the transitions between the two states of a TLS occur via tunneling or thermal activation because we assume there is no coherence between successive transitions. Thus we represent a TLS elastic dipole by an Ising spin. Since TLS occur at random locations, their interactions are random. So we will

use a nearest-neighbor Ising spin glass to model the interacting TLS bath.

4.2.1 Simulation Details

We performed Monte Carlo simulations of a 2D Ising spin glass on a square 16 × 16 lattice with periodic boundary conditions. Each Ising spin corresponds to a TLS with an elastic dipole moment. The Hamiltonian is given by

$$H = -\sum_{\langle i,j \rangle} J_{ij} S_i S_j, \tag{4.11}$$

where S_i and S_j are Ising spins with values ± 1 on nearest neighbor sites i and j, respectively. J_{ij} is the nearest neighbor coupling. It represents the elastic coupling between TLS. We use a spin glass distribution of couplings chosen from a normal distribution centered at $J_{ij} = 0$ with a variance $\sigma^2_{J_{ij}} = 1$. A positive value for J_{ij} indicates a ferromagnetic interaction.

We can rewrite the Hamiltonian in terms of local fields h_i:

$$H = -\frac{1}{2} \sum_i h_i S_i, \tag{4.12}$$

where the local field of S_i is produced by the neighboring spins:

$$h_i = \sum_j J_{ij} S_j. \tag{4.13}$$

The Ising spins are initialized at infinite temperature with randomly oriented spins. A spin is allowed to reorient itself according to the Metropolis algorithm [36]. In this algorithm, a trial move consists of first choosing a spin on the lattice at random. For a given temperature T, the initial energy E_i of this site is calculated using Eq. (4.13) from the local field produced by its nearest neighbors. The orientation of the spin is reversed in a trial move, and the final

energy E_f of this site with the new spin orientation is calculated. If the final energy is less than the initial energy, then the spin flip is accepted. However, if the final energy is greater than the initial energy, then the Boltzmann factor $\exp[-(E_f - E_i)/(k_B T)]$ is calculated. If a random number generated from a uniform distribution between 0 and 1 is less than this Boltzmann factor, then the new orientation is accepted. This process continues for the remaining sites within the lattice until all the spins in the lattice have been given an opportunity to flip. The time it takes for one sweep through the lattice is one Monte Carlo step (MCS).

The Ising spin glass is cooled from its initial infinite temperature spin configuration at $T = 10$ to $T = 0.6$. At each temperature, after an initial equilibration time of 10^5 MCS, we check to see if the system is equilibrated using the method of Bhatt and Young [67]. Details of the equilibration are given in Appendix B.1.

Each TLS has an electric dipole moment. These electric dipoles are initialized with random orientations. Since the electric dipole-dipole interaction is an order of magnitude smaller than the elastic dipole-dipole interaction, it is the elastic interactions between TLS that governs their dynamics. We represent these dynamics by the Ising spin glass described above. Thus, each electric dipole has a corresponding Ising spin. If the Ising spin flips, then the corresponding electric dipole and its image dipole flip 180^o. We consider two cases of electric dipole orientations. In both cases, the magnitude of the dipole moment is unity. In the first case, the dipoles are randomly oriented with random x, y, and z components. To better understand the contribution of each component, we also consider a second case where the dipole all lie parallel to one another along the x, y, or z axis, though they are randomly oriented in the positive or negative direction.

Let us take a moment to describe the device geometry that we have in mind. TLS that have both an electric and an elastic dipole moment are located on every site of a 16×16 square lattice. We envision these TLS to reside in the oxide layer of a Si/Si-Ge heterostructure with

a quantum well. Since TLS are typically about 10 nm apart, we take the lattice spacing to be 10 nm; this sets the length scale. A second 16×16 square lattice is located half a lattice spacing above the first lattice and is populated by the image dipoles that result from the ground plane formed by metal gates. We consider two QDs about 100 nm apart located in a quantum well about 30-50 nm below the oxide layer. So in our simulation two QDs plane are separated by 10 lattice spacings in a plane located 3 lattice spacings below the first electric dipole lattice. This is illustrated in Figure 4.1.

4.2.2 Noise Power, Exponents, and Correlation Functions

The fluctuating electric dipole moments produce a time dependent electric potential $V_i(t)$ at the ith QD given by Eq. (4.10). After equilibration of the Ising spin glass, the potential is recorded at every Monte Carlo step, resulting in a time series that can be Fourier transformed to obtain the charge noise power spectrum. The deviation from the average is $\delta V_i(t) = V_i(t) - \overline{V_i(t)}$. The noise power spectral density can be determined from the Fourier transform of the autocorrelation function $C_i(\tau) = \int_{-\infty}^{\infty} \delta V_i(t)\delta V_i(t+\tau)dt$. For a time series of length t_{total}: $S(f) = \frac{1}{t_{\text{total}}} \int_{-\infty}^{\infty} C_i(\tau)e^{-2\pi i f\tau}d\tau$. A useful method for computing the power spectrum is the periodogram estimate [37]:

$$S_i(f) = \frac{1}{t_{\text{total}}}|\delta V_i(f)|^2, \tag{4.14}$$

where t_{total} is the length of the potential time series, and $\delta V(f)$ is the Fourier transform of the electric potential time series. The Fourier transform is computed using the C subroutine library FFTW [38]. At a given temperature, the time series $V_i(t)$ is split into ten segments of equal length. The power spectrum is found for each segment and is averaged over these

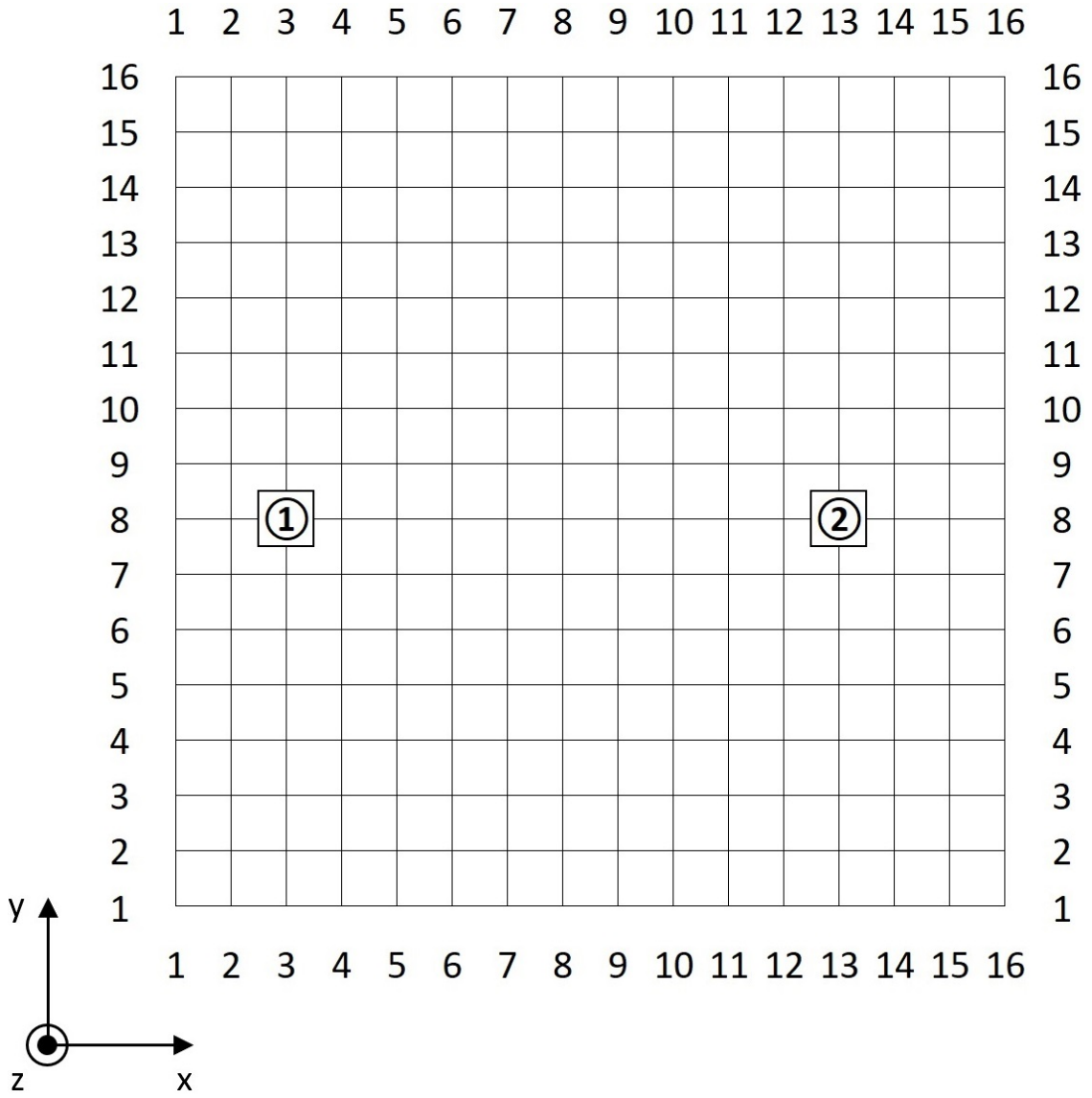

Figure 4.1: 16 x 16 lattice with an electric dipole occupying every site. The circled 1 and 2 represent quantum dots that are three lattice spacings beneath the main lattice.

segments to give a smoother power spectrum. The power spectrum is normalized so that

$$P_{i,\text{total}} = \frac{2}{t_{\text{total}}} \sum_{f=0}^{f_{\max}} S_i(f) = \sigma_{V_i}^2, \tag{4.15}$$

where P_{total} is the total noise power and $\sigma_{V_i}^2$ is the variance in the elecctric potential of the ith QD. To determine the noise exponent α, the function A^2/f^α is fit to power spectra (averaged over 10 segments) in the vicinity of a fixed frequency because experiments typically determine noise exponents at 1 Hz.

To calculate the correlation between the fluctuating dipole potentials $V_1(t)$ and $V_2(t)$, we use the Pearson correlation coefficient that is given by:

$$\rho_{V_1(t),V_2(t)} = \frac{\langle \delta V_1(t) \delta V_2(t) \rangle_t}{\sigma_{V_1(t)} \sigma_{V_2(t)}}, \tag{4.16}$$

where $\delta V_1(t)$ and $\delta V_2(t)$ are the fluctuations in the potentials about their average. $\sigma_{V_1(t)}$ and $\sigma_{V_2(t)}$ are the standard deviations of the potentials. To calculate the correlations, the time series $V_1(t)$ and $V_2(t)$ are divided into ten blocks of equal size. The correlation is calculated for each of the ten blocks using Eq. (4.16), and the standard deviation is calculated from the ten correlations. The correlations and standard deviations are then averaged over 200 independent runs.

We also calculate the noise correlation between the two QDs as a function of frequency as was done in [45]. We use:

$$\rho_{V_1(t),V_2(t)}(f) = \frac{\langle \delta \tilde{V}_1(f) \delta \tilde{V}_2^*(f) \rangle_{\text{blocks,runs}}}{\sqrt{\langle S_{V_1}(f) \rangle_{\text{blocks,runs}} \langle S_{V_2}(f) \rangle_{\text{blocks,runs}}}}, \tag{4.17}$$

where $\delta \tilde{V}_1(f)$ and $\delta \tilde{V}_2(f)$ are the Fourier transforms of the fluctuations in the potentials about their average. $S_{V_1}(f)$ and $S_{V_2}(f)$ are the noise power of the dipole potentials at quantum dots 1 and 2. To calculate the numerator of Eq. (4.17), the time series $V_1(t)$ and

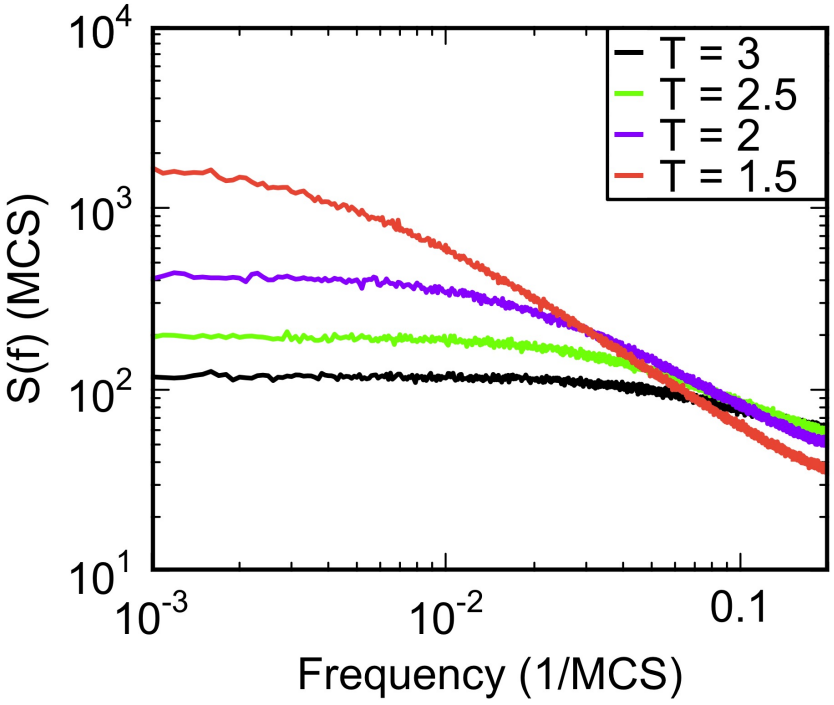

Figure 4.2: Plots of the electric dipole potential noise power at QD 1 vs. frequency for $1.5 \leq T \leq 3$ averaged over 200 runs. The noise is produced by fluctuating electric dipoles with random orientations.

$V_2(t)$ are divided into 100 blocks of equal size. For each block, the Fourier transforms of the fluctuations are calculated. The product $\delta\tilde{V}_1(f)\delta\tilde{V}_2^*(f)$ is averaged over the 100 blocks and 200 runs to give $\langle\delta\tilde{V}_1(f)\delta\tilde{V}_2^*(f)\rangle_{\text{blocks,runs}}$. To calculate the denominator of Eq. (4.17), the power spectra $S_1(f)$ and $S_2(f)$ are calculated for each block. Then $S_1(f)$ and $S_2(f)$ are each averaged over the 100 blocks and 200 runs to give $\langle S_{V_1}(f)\rangle_{\text{blocks,runs}}$ and $\langle S_{V_2}(f)\rangle_{\text{blocks,runs}}$. The denominator of the correlation is then calculated and used in Eq. (4.17). Since the frequency-dependent correlation function in Eq. (4.17) is a complex number, we plot its magnitude and phase as a function of frequency.

4.3 Results

Figure 4.2 shows the noise power at QD 1 at various temperatures for randomly oriented dipoles averaged over 200 runs. To determine the amplitude $A^2(T)$ and the noise exponent $\alpha(T)$, the function $A^2(T)/f^{\alpha(T)}$ is fit to the region of the power spectra that is linear on a log-log plot. The noise exponent $\alpha(T)$ as a function of temperature is shown in Fig. 4.3. Experimentally, the noise exponents within one standard deviation of the mean at 1 Hz ranged from about 0.6 to 1.25 [18, 53, 68]. In our simulations the noise exponents increase from zero at high temperatures to approximately 1.15 at low temperatures which is roughly consistent with experiment.

The noise amplitude $A^2(T)$ shown in the inset of Fig. 4.3 goes as $T^{2.4}$. For an ensemble of fluctuators with thermally activated switching rates and a flat distribution of activation energies, one would expect the noise amplitude to increase linearly with temperature [44]. However, as we mentioned in the introduction, experiments find the temperature dependence of the noise at 1 Hz increasingly deviates from linearity with increasing thickness of the gate oxide layer [18, 53] and, in another study, was found to be quadratic [54]. So our simulation results are qualitatively consistent with experiment but the reason why is not clear. Ising spins do not have activation barriers per se; they simply flip based on the energy difference between the initial and final states.

If one considers the contributions of the different components of the dipoles to the charge noise, one realizes that the z-component dominates because the z-component of the image dipole in the ground plane (that lies perpendicular to the z-axis) points in the same direction as the z-component of the original dipole. However, the x and y components of the image dipole point in the opposite direction of the x and y components, respectively, of the original dipole. To confirm this, we have performed simulations for dipoles that lie along either the x, y, or z axis (see Appendix B.2 for details of the simulations). The results are shown in

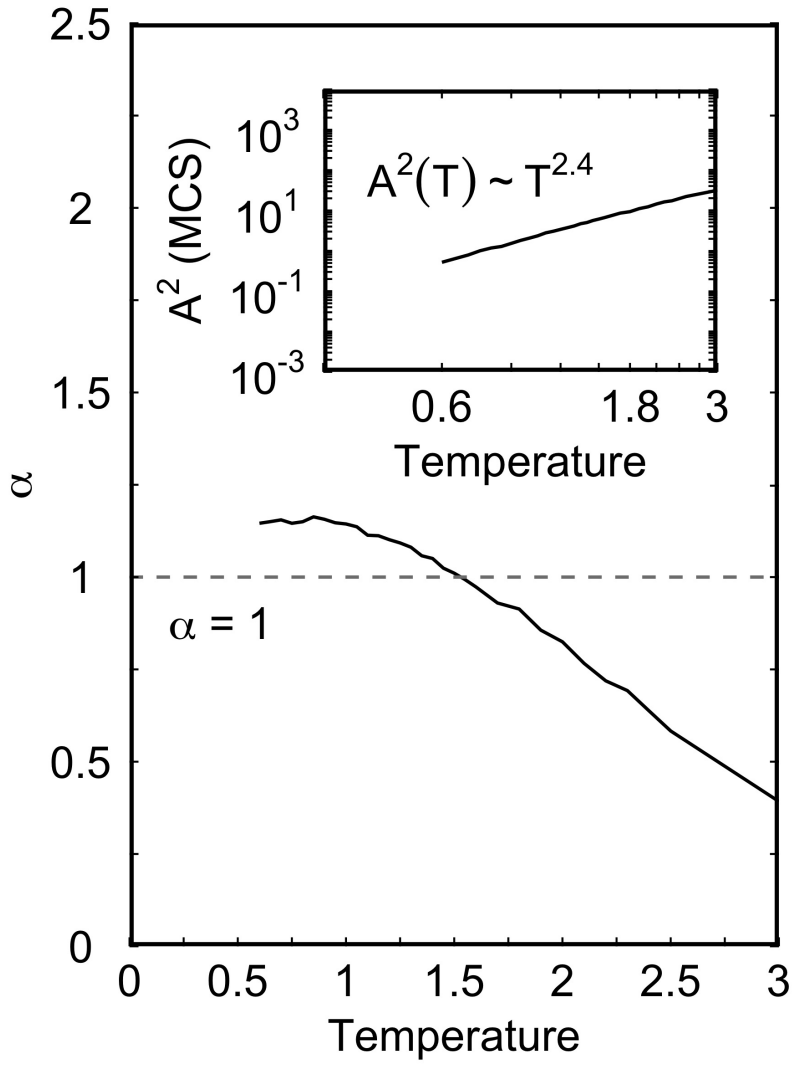

Figure 4.3: Plot of the temperature dependence of the exponent, $\alpha(T)$, of the electric potential noise power spectra at QD 1 resulting from fluctuating electric dipoles with random orientations for $0.6 \leq T \leq 3$. Inset: Log-log plot of the temperature dependence of the electric potential noise power amplitude, $A^2(T)$, at QD 1 resulting from fluctuating electric dipoles with random orientations for $0.6 \leq T \leq 3$.

Figures B.4 and B.5. One can see that the noise produced by the dipoles along the z-axis is about two orders of magnitude larger than that associated with dipoles along the x or y axes. Comparing the plots in Fig. B.4 with the corresponding plots (Figs. 4.2, 4.3, and 4.6) for randomly oriented dipoles, we see the marked similarity between the results for the dipoles along the z-axis and the randomly oriented dipoles. However, the noise power and noise amplitudes resulting from electric dipoles aligned along the z-axis are three times larger than that of the randomly oriented dipoles because the z-axis dipoles have unit length, while the z components of the randomly-oriented dipoles have a typical length of $1/\sqrt{3}$.

Using Eq. (4.16), we calculated the correlation in the noise between QD 1 and QD 2 as shown in Fig. 4.6. We can see from Fig. 4.6 that there is some correlation between QDs 1 and 2 which is consistent with experiment. As we mentioned earlier, recent measurements find that there are correlations in the charge noise between quantum dots that are about 100 nm apart [45].

To better understand the correlations in the noise at the two QDs, we used Eq. (4.17) to calculate the frequency dependence of the magnitude and phase produced by randomly oriented fluctuating electric dipoles as well as dipoles aligned along various axes (see Figure 4.7). Fig. 4.7(a) shows that there is some correlation in the noise between the two dots as we saw in the Pearson correlation. These correlations are due largely to the geometry of the location of the dipoles with respect to the QDs. There is no noticeable frequency dependence in either the magnitude or the phase of the correlations because unlike the experimental case [45], our QDs have no dynamics.

The magnitude of the noise correlation is larger for the x-axis and z-axis dipoles compared to the y-axis dipoles, and comparable to that for randomly oriented dipoles (see Figs. B.4(f) and 4.7(a)). Even though the numerator of Eq. (4.17) is about two orders of magnitude larger for dipoles aligned along the z-axis compared to those aligned along the x-axis, the normalization by the noise amplitude in the denominator makes the noise correlation of the

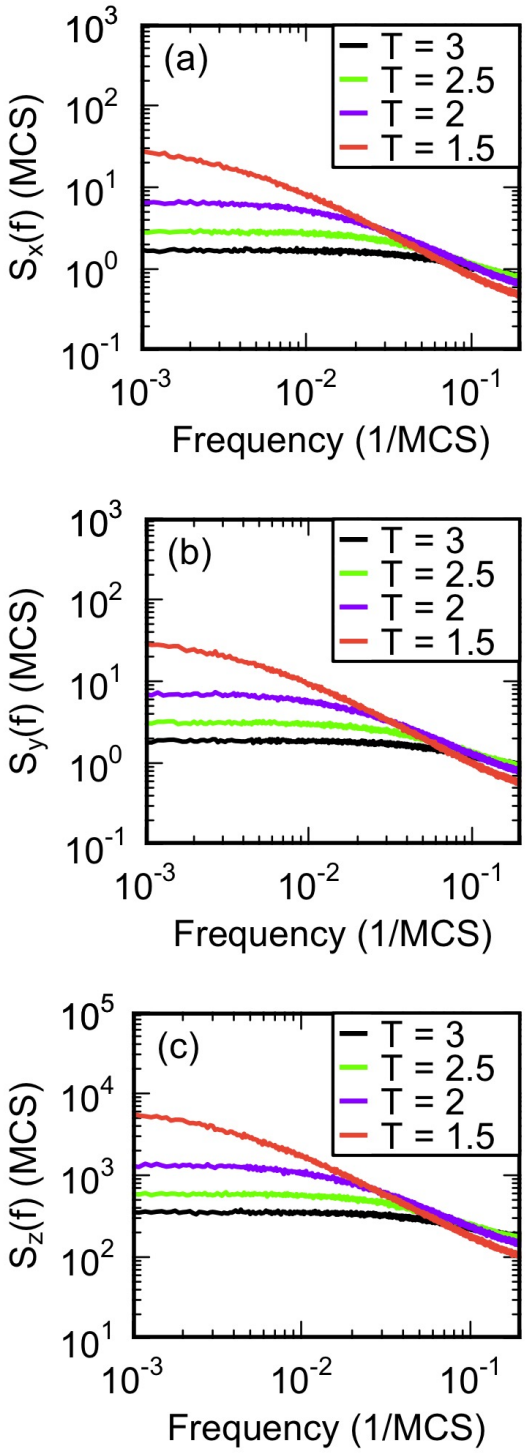

Figure 4.4: Log-log plots of the electric potential noise power versus frequency at QD 1 for fluctuating dipoles that lie along the (a) x-axis, (b) y-axis, and (c) z-axis. All plots are the result of averaging over 200 runs.

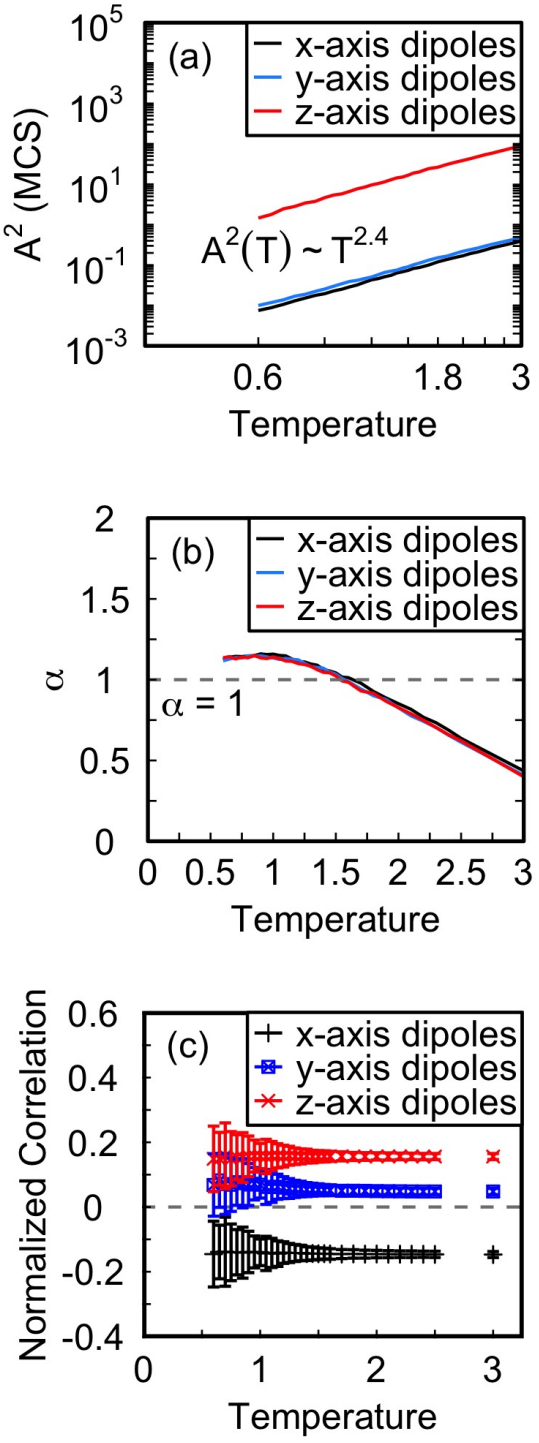

Figure 4.5: (a) Log-log plot of temperature dependence of the noise amplitude, $A^2(T)$, obtained from fits to the noise power. (b) Plot of the temperature dependence of the noise exponent, $\alpha(T)$, obtained from fits to the noise power. (c) Plots of noise correlation between QDs 1 and 2 vs. temperature calculated using Eq. (4.16). Plots (a)-(c) show results for dipoles lying along the x, y, and z axes. All plots are the result of averaging over 200 runs.

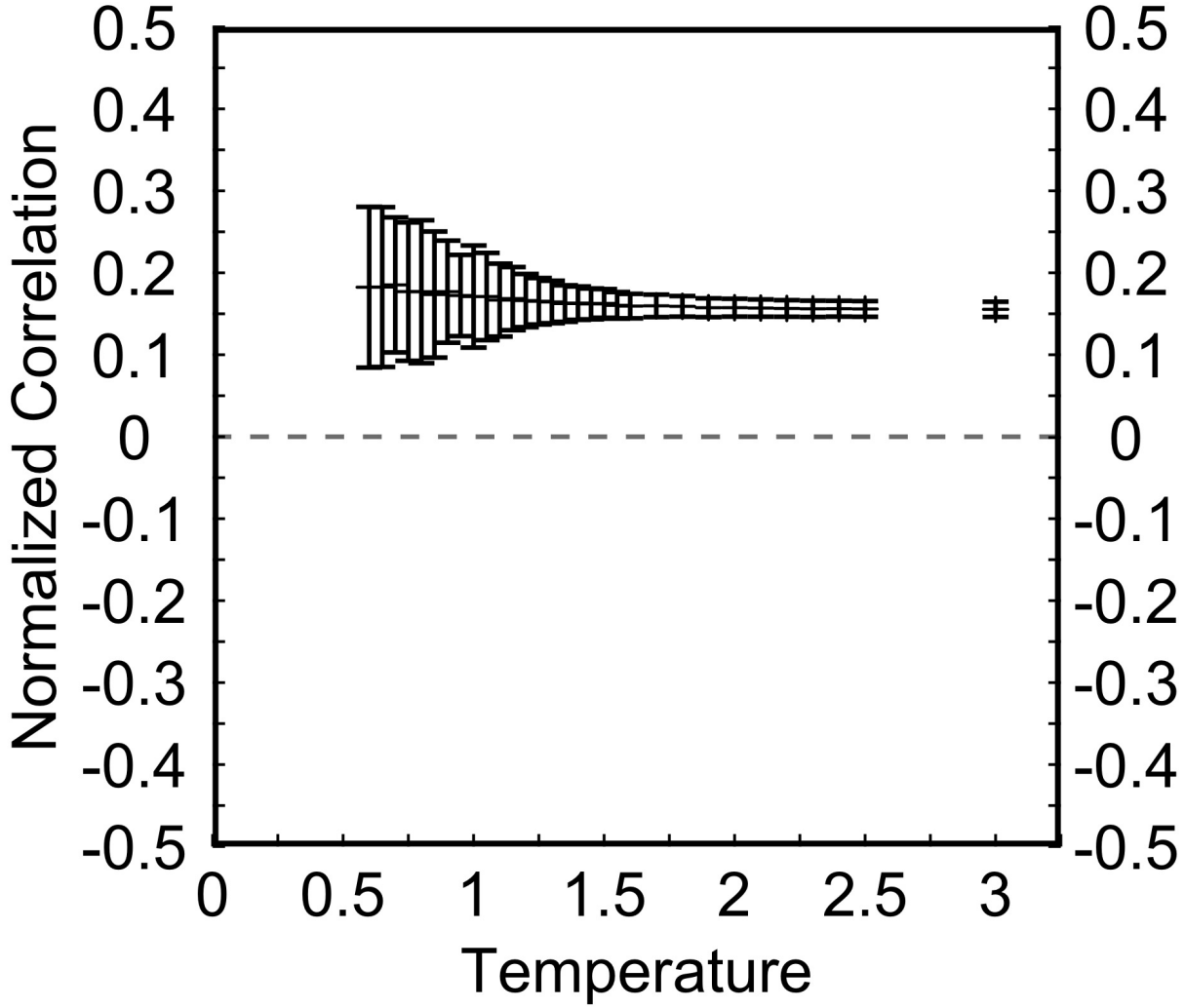

Figure 4.6: Plot of electric potential noise correlations between QDs 1 and 2 vs. temperature for $0.8 \leq T \leq 3$ resulting from fluctuating electric dipoles with random orientations.

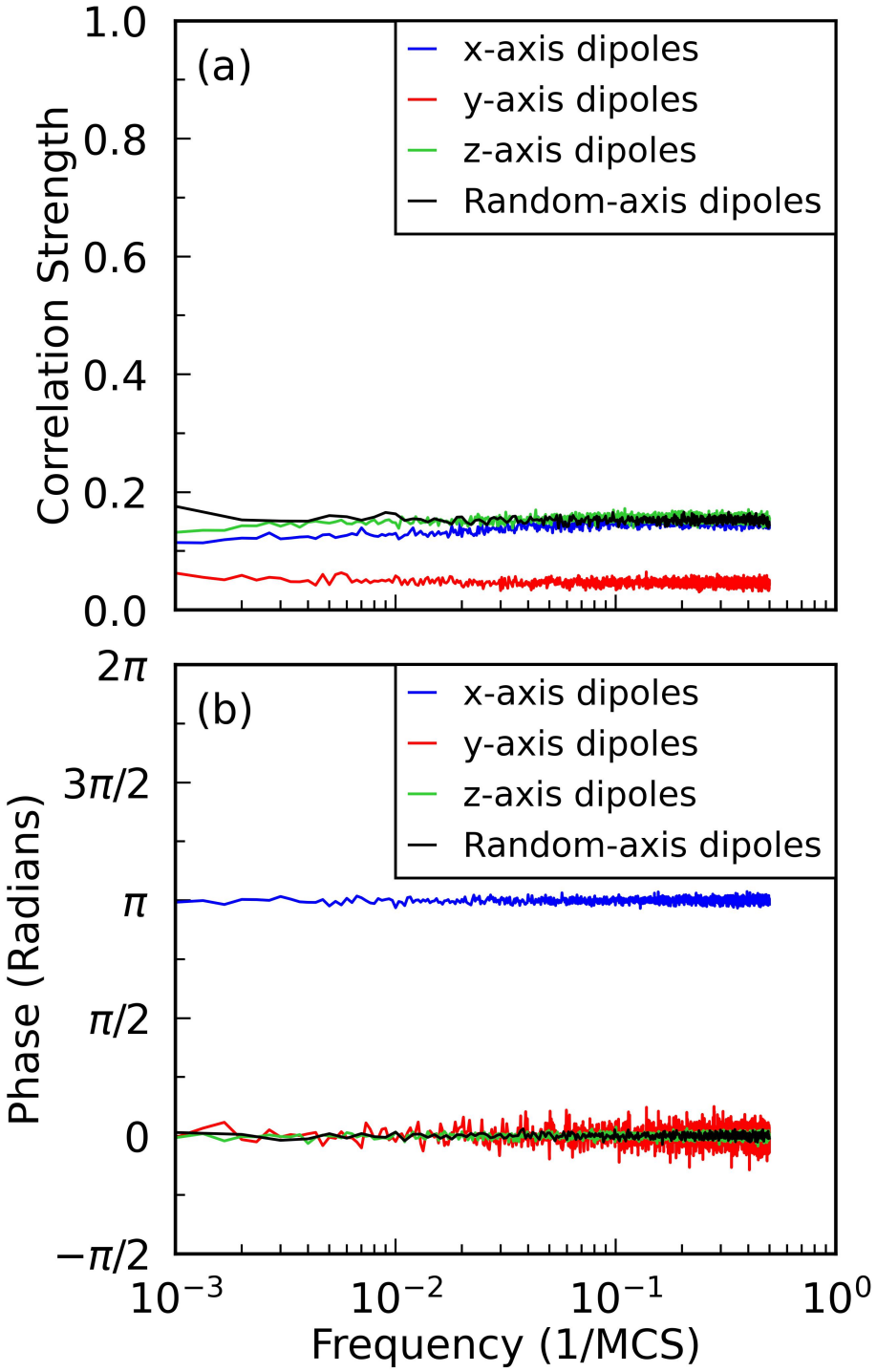

Figure 4.7: Plots of the (a) magnitude and (b) phase of electric potential noise correlations between QDs 1 and 2 as a function of frequency for fluctuating electric dipoles with fixed (x, y, and z) and random orientations at $T = 1$. Plots are the result of averaging over 200 runs.

x and z axis dipoles comparable. The sizeable contribution of the x-axis dipoles, especially those located at or near the same y-coordinate as the QDs, is due to the large value of

$(\vec{p}_{\eta,i}(t) \cdot \hat{R}_\eta)$, the numerator of Eq. (4.10), coupled with the small value of the denominator $R^2_{\eta,i}$. $(\vec{p}_{\eta,i}(t) \cdot \hat{R}_\eta)$ is large because $\vec{p}_{\eta,i}(t)$ is collinear with $\hat{R}_\eta$. On the other hand, the y-axis dipoles have small values of $(\vec{p}_{\eta,i}(t) \cdot \hat{R}_\eta)$ when the y-coordinate of their location is comparable to that of the QDs because the y-axis dipole is almost perpendicular to the unit vector $\hat{R}_\eta$ pointing from the dipole to the QD. Again z-axis dipoles give large contributions because their image charges lie in the same direction as the z-axis dipoles themselves.

Figure 4.7(b) shows that the correlations produced by the x-axis dipoles are 180° out of phase. This is due to the fact that since the QDs lie along the x-axis, flips in the x-axis dipoles located between the QDs will have the opposite effect on each dot due to the factor $(\vec{p}_{\eta,i}(t) \cdot \hat{R}_\eta)$ in the numerator of Eq. (4.10).

4.4 Summary

We propose a model in which the $1/f$ charge noise in quantum dots is due to a bath of electric dipole fluctuators that interact with each other primarily via the elastic strain field. We use a 2D nearest-neighbor Ising spin glass to represent these elastic interactions and to simulate the dynamics the bath of electric dipole fluctuators in the presence of a ground plane representing metal gates above the oxide layer containing the fluctuators. We find $1/f$ noise spectra with a temperature dependent amplitude that are in qualitative agreement with experiment. Likewise, the noise correlations between quantum dots are also in qualitative agreement with experiment.

Bibliography

[1] S. M. Anton, J. S. Birenbaum, S. R. O'Kelley, V. Bolkhovsky, D. A. Braje, G. Fitch, M. Neeley, G. C. Hilton, H.-M. Cho, K. D. Irwin, F. C. Wellstood, W. D. Oliver, A. Shnirman, and J. Clarke, Phys. Rev. Lett. **110**, 147002 (2013).

[2] S. Ahn, S. Das Sarma, and J. P. Kestner, Phys. Rev. B **103**, L041304 (2021).

[3] M. A. Nielsen and I. L. Chuang, *Quantum computation and quantum information*, 10th ed., Cambridge Series on Information and the Natural Sciences (Cambridge University Press, 2010).

[4] N. C. Jones, R. Van Meter, A. G. Fowler, P. L. McMahon, J. Kim, T. D. Ladd, and Y. Yamamoto, Phys. Rev. X **2**, 031007 (2012).

[5] M. Brooks, *Quantum computing and communications* (Springer, New York, 1999).

[6] F. Tennie and T. Palmer, Quantum computers for weather and climate prediction: The good, the bad and the noisy (2022).

[7] R. Orús, S. Mugel, and E. Lizaso, Reviews in Physics **4**, 100028 (2019).

[8] M. Schuld, I. Sinayskiy, and F. Petruccione, Quantum Information Processing **13**, 2567–2586 (2014).

[9] V. Dunjko and H. J. Briegel, Reports on Progress in Physics **81**, 074001 (2018).

[10] J. Clarke and F. K. Wilhelm, Nature **453** (2008).

[11] J. Bardeen, L. N. Cooper, and J. R. Schrieffer, Phys. Rev. **108**, 1175 (1957).

[12] J. Clarke and A. I. Braginski, *The SQUID handbook*, Vol. 1 (Wiley-VCH, 2004).

[13] C. H. van der Wal, A. C. J. ter Haar, F. K. Wilhelm, R. N. Schouten, C. J. P. M. Harmans, T. P. Orlando, S. Lloyd, and J. E. Mooij, Science **290**, 773 (2000).

[14] J. R. Friedman, V. Patel, W. Chen, S. K. Tolpygo, and J. E. Lukens, Nature **406**, 43–46 (2000).

[15] Y. Nakamura, C. D. Chen, and J. S. Tsai, Phys. Rev. Lett. **79**, 2328 (1997).

[16] J. M. Martinis, M. H. Devoret, and J. Clarke, Phys. Rev. Lett. **55**, 1543 (1985).

[17] D. Loss and D. P. DiVincenzo, Phys. Rev. A **57**, 120 (1998).

[18] E. J. Connors, J. Nelson, H. Qiao, L. F. Edge, and J. M. Nichol, Phys. Rev. B **100**, 165305 (2019).

[19] F. A. Zwanenburg, A. S. Dzurak, A. Morello, M. Y. Simmons, L. C. L. Hollenberg, G. Klimeck, S. Rogge, S. N. Coppersmith, and M. A. Eriksson, Rev. Mod. Phys. **85**, 961 (2013).

[20] X. Hu and S. Das Sarma, Phys. Rev. Lett. **96**, 100501 (2006).

[21] J. R. Petta, A. C. Johnson, J. M. Taylor, E. A. Laird, A. Yacoby, M. D. Lukin, C. M. Marcus, M. P. Hanson, and A. C. Gossard, Science **309**, 2180 (2005).

[22] R. C. Bialczak, R. McDermott, M. Ansmann, M. Hofheinz, N. Katz, E. Lucero, M. Neeley, A. D. O'Connell, H. Wang, A. N. Cleland, and J. M. Martinis, Phys. Rev. Lett. **99**, 187006 (2007).

[23] F. C. Wellstood, C. Urbina, and J. Clarke, Applied Physics Letters **50**, 772 (1987).

[24] S. Sendelbach, D. Hover, A. Kittel, M. Mück, J. M. Martinis, and R. McDermott, Phys. Rev. Lett. **100**, 227006 (2008).

[25] H. Wang, C. Shi, J. Hu, S. Han, C. C. Yu, and R. Q. Wu, Phys. Rev. Lett. **115**, 077002 (2015).

[26] P. Kumar, S. Sendelbach, M. A. Beck, J. W. Freeland, Z. Wang, H. Wang, C. C. Yu, R. Q. Wu, D. P. Pappas, and R. McDermott, Phys. Rev. Applied **6**, 041001 (2016).

[27] S. Kempf, A. Ferring, and C. Enss, Appl. Phys. Lett. **109**, 162601 (2016).

[28] H. Bluhm, J. A. Bert, N. C. Koshnick, M. E. Huber, and K. A. Moler, Phys. Rev. Lett. **103**, 026805 (2009).

[29] P. Dutta and P. M. Horn, Rev. Mod. Phys. **53**, 497 (1981).

[30] R. H. Koch, D. P. DiVincenzo, and J. Clarke, Phys. Rev. Lett. **98**, 267003 (2007).

[31] R. de Sousa, Phys. Rev. B **76**, 245306 (2007).

[32] Z. Chen and C. C. Yu, Phys. Rev. Lett. **104**, 247204 (2010).

[33] T. Lanting, M. H. Amin, A. J. Berkley, C. Rich, S.-F. Chen, S. LaForest, and R. de Sousa, Phys. Rev. B **89**, 014503 (2014).

[34] B. F. Davis and R. V. Chamberlin, Journal of Statistical Mechanics: Theory and Experiment **2018**, 103206 (2018).

[35] R. Harris, M. Plischke, and M. J. Zuckermann, Phys. Rev. Lett. **31**, 160 (1973).

[36] N. Metropolis, A. W. Rosenbluth, M. N. Rosenbluth, A. H. Teller, and E. Teller, J. Chem. Phys. **21**, 1087 (1953).

[37] W. H. Press, S. A. Teukolsky, W. T. Vetterling, and B. P. Flannery, *Numerical Recipes in C: The Art of Scientific Computing* (Cambridge University Press, New York, 1992).

[38] M. Frigo and S. G. Johnson, Proceedings of the IEEE **93**, 216 (2005), special issue on "Program Generation, Optimization, and Platform Adaptation".

[39] Z. Chen and C. C. Yu, Phys. Rev. Lett. **98**, 057204 (2007).

[40] N. D. Mermin and H. Wagner, Phys. Rev. Lett. **17**, 1133 (1966).

[41] P. C. Hohenberg, Phys. Rev. **158**, 383 (1967).

[42] E. J. Connors, J. Nelson, and J. M. Nichol, Charge-noise spectroscopy of si/sige quantum dots via dynamically-decoupled exchange oscillations (2021), arXiv:2103.02448 [cond-mat.mes-hall] .

[43] R. M. Jock, N. T. Jacobson, M. Rudolph, D. R. Ward, M. S. Carroll, and D. R. Luhman, A silicon singlet-triplet qubit driven by spin-valley coupling (2021), arXiv:2102.12068 [cond-mat.mes-hall] .

[44] L. Petit, H. G. J. Eenink, M. Russ, W. I. L. Lawrie, N. W. Hendrickx, S. G. J. Philips, J. S. Clarke, L. M. K. Vandersypen, and M. Veldhorst, Nature **580**, 355 (2020).

[45] J. Yoneda, J. S. Rojas-Arias, P. Stano, K. Takeda, A. Noiri, T. Nakajima, D. Loss, and S. Tarucha, Noise-correlation spectrum for a pair of spin qubits in silicon (2022), arXiv:2208.14150 [quant-ph] .

[46] P. Dutta, P. Dimon, and P. M. Horn, Phys. Rev. Lett. **43**, 646 (1979).

[47] H. Gould and J. Tobochnik, *Statistical and Thermal Physics: With Computer Applications* (Princeton University Press, Princeton, 2010).

[48] R. Löfstedt and S. N. Coppersmith, Phys. Rev. E **49**, 4821 (1994).

[49] B. McNamara and K. Wiesenfeld, Phys. Rev. A **39**, 4854 (1989).

[50] R. F. Voss and J. Clarke, Physical Review B **13**, 556 (1976).

[51] D. M. Zajac, T. M. Hazard, X. Mi, K. Wang, and J. R. Petta, Applied Physics Letters **106**, 223507 (2015).

[52] L. Abou-Hamdan, S. Hamyeh, A. Iskandar, R. Tauk, J. Brault, M. Tabbal, P.-M. Adam, and M. Kazan, Nanotechnology **32**, 115703 (2020).

[53] E. J. Connors, J. Nelson, H. Qiao, L. F. Edge, and J. M. Nichol, Phys. Rev. B **102**, 039902 (2020).

[54] L. Petit, J. M. Boter, H. G. J. Eenink, G. Droulers, M. L. V. Tagliaferri, R. Li, D. P. Franke, K. J. Singh, J. S. Clarke, R. N. Schouten, V. V. Dobrovitski, L. M. K. Vandersypen, and M. Veldhorst, Phys. Rev. Lett. **121**, 076801 (2018).

[55] D. Mickelsen, H. M. Carruzzo, S. N. Coppersmith, and C. C. Yu, Effects of temperature fluctuations on charge noise in quantum dot qubits (2023), arXiv:1234.56789 .

[56] C. King, J. S. Schoenfield, M. J. Calderón, B. Koiller, A. Saraiva, X. Hu, H. W. Jiang, M. Friesen, and S. N. Coppersmith, Phys. Rev. B **101**, 155411 (2020).

[57] C. C. Yu, Phys. Rev. B **32**, 4220 (1985).

[58] S. Hunklinger and A. K. Raychaudhuri, Prog. in Low Temp. Phys. **9**, 265 (1986).

[59] W. A. Phillips, Rep. Prog. Phys. **50**, 1657 (1987).

[60] P. W. Anderson, B. I. Halperin, and C. M. Varma, The Philosophical Magazine: A Journal of Theoretical Experimental and Applied Physics **25**, 1 (1972), https://doi.org/10.1080/14786437208229210 .

[61] W. A. Phillips, Journal of Low Temperature Physics **7**, 351 (1972).

[62] C. C. Yu and A. J. Leggett, Comments Cond. Mat. Phys. **14**, 231 (1988).

[63] D. J. Salvino, S. Rogge, B. Tigner, and D. D. Osheroff, Phys. Rev. Lett. **73**, 268 (1994).

[64] H. M. Carruzzo, E. R. Grannan, and C. C. Yu, Phys. Rev. B **50**, 6685 (1994).

[65] J. Joffrin and A. Levelut, J. Phys. France **36** (1975).

[66] H. M. Carruzzo and C. C. Yu, Phys. Rev. Lett. **124**, 075902 (2020).

[67] R. N. Bhatt and A. P. Young, Phys. Rev. B **37**, 5606 (1988).

[68] R. M. Jock, N. T. Jacobson, M. Rudolph, D. R. Ward, M. S. Carroll, and D. R. Luhman, Nature Comm. **13**, 641 (2022).

[69] C. C. Yu and H. M. Carruzzo, Phys. Rev. E **69**, 051201 (2004).

Appendix A

Monte Carlo Simulations of Magnetic Noise

A.1 Fitting

The process for fitting A^2/f^α to the noise power spectra to determine the noise exponent starts with dividing the noise power spectra into frequency segments as shown in Fig. A.1(a). The segments from f_i to f_{i+1} range from $i = 1$ to $i = N_{\text{segments}} - 1$. The segments follow the condition $f_{i+1}/f_i = 10^{0.1}$. The function A^2/f^α is fit to each segment starting at the lowest frequency segment.

The relative change in the noise exponent between the current segment and the previous one is calculated. An example of the relative change is shown in Fig. A.1(b). If the relative change is less than 1% and the noise exponent is greater than 0.2, then the frequency range of the segment is noted. The lower and upper limits of the new frequency fit range are found by combining all of these segments. In the figure, this is shown by two vertical dotted lines. A fit is performed in this region.

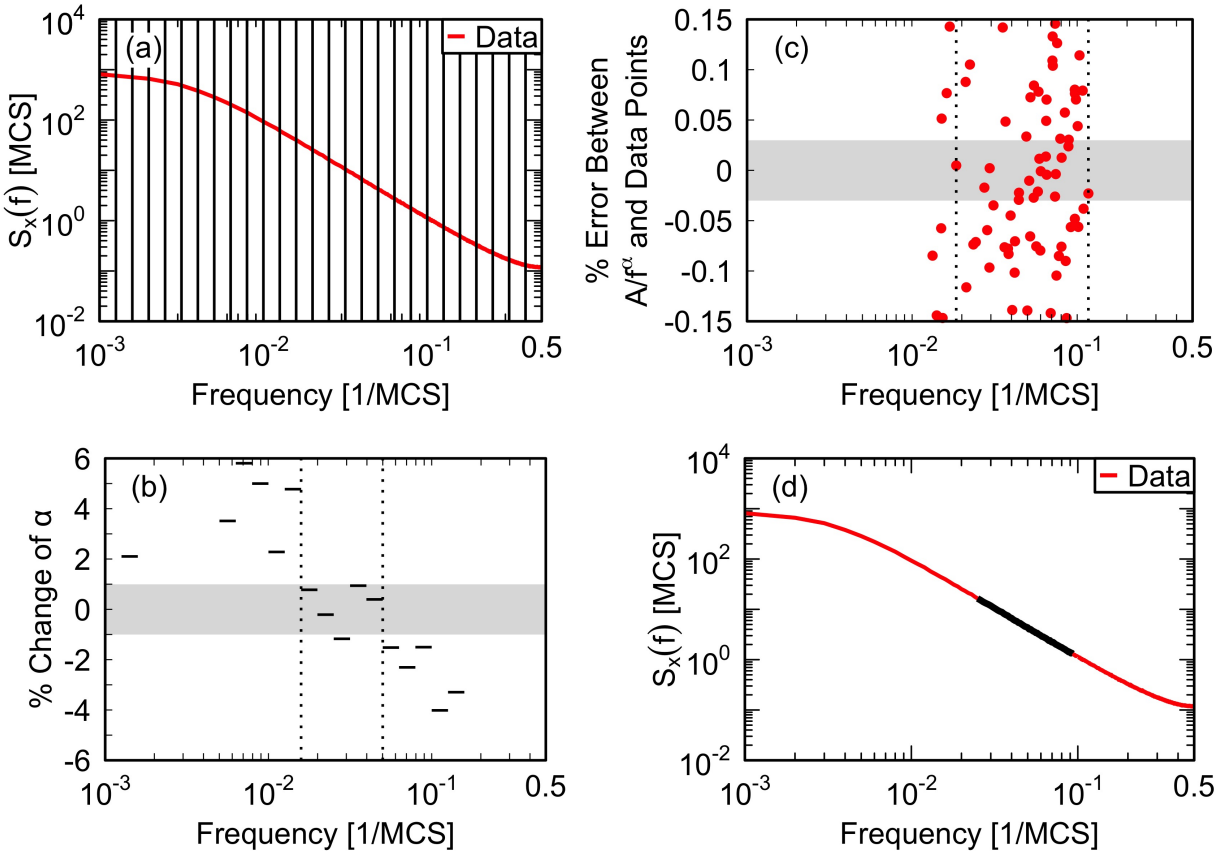

Figure A.1: Fitting method using the power spectrum averaged over 100 segments of the isotropic ($A = 0$) Heisenberg ferromagnet (J_{ij}=1) at $T = 0.9$. (a) Segmented power spectra: noise power $S_x(f)$ of the x-component of the total magnetic moment versus frequency. (b) Relative change in exponent versus frequency for the segmented power spectra. (c) Percent error between the power spectra fit and data versus frequency. (d) Noise power $S_x(f)$ of the x-component of the total magnetic moment versus frequency. The data segment used for fitting is shown in black.

The percent error of the fit is the percent difference between A^2/f^α evaluated at a particular f and the noise power at f from the data. The percent error is evaluated for all frequency data points within the fitted frequency range and is shown in Fig. A.1(c). A new frequency range is defined by the maximum and minimum frequencies corresponding to percent differences of less than 0.03% as shown by vertical dotted lines.

This frequency range is shortened by increasing the lower limit by 30% and decreasing the upper limit by 20%. By reducing the frequency range, the fit region will not be within the knee and aliasing regions. These percentages that were found by trial and error work well for all models presented. The final fit of A^2/f^α is performed within this new frequency range. The power spectra and final fit region of the power spectra are shown in Fig. A.1(d).

A.2 High-Temperature Pivot of the Ising Spin Glass

As seen in Figs. 2.8 and 2.9 in Sec. 2.3.4, the noise power spectra tend to pivot at high temperature. The noise power as a function of frequency at high temperature for the 2D Ising spin glass is shown in Fig. A.2. Although the power spectra pivots, the noise exponent is negative. This is because Ising spin flips are always 180° rotations. At high temperature, Ising spins have a high probability of flipping at every time step which increases the noise at $f = 0.5$ MCS^{-1}. In the infinite-temperature limit, the power spectrum would be a delta function peaked at $f = 0.5$ MCS^{-1}.

A.3 Crossing Condition

The experimental results of Anton *et al.* indicate that at high temperatures, the temperature dependence of the noise amplitude can be described by $A^2(T) = A_0^2 T^\gamma$ and the noise exponent

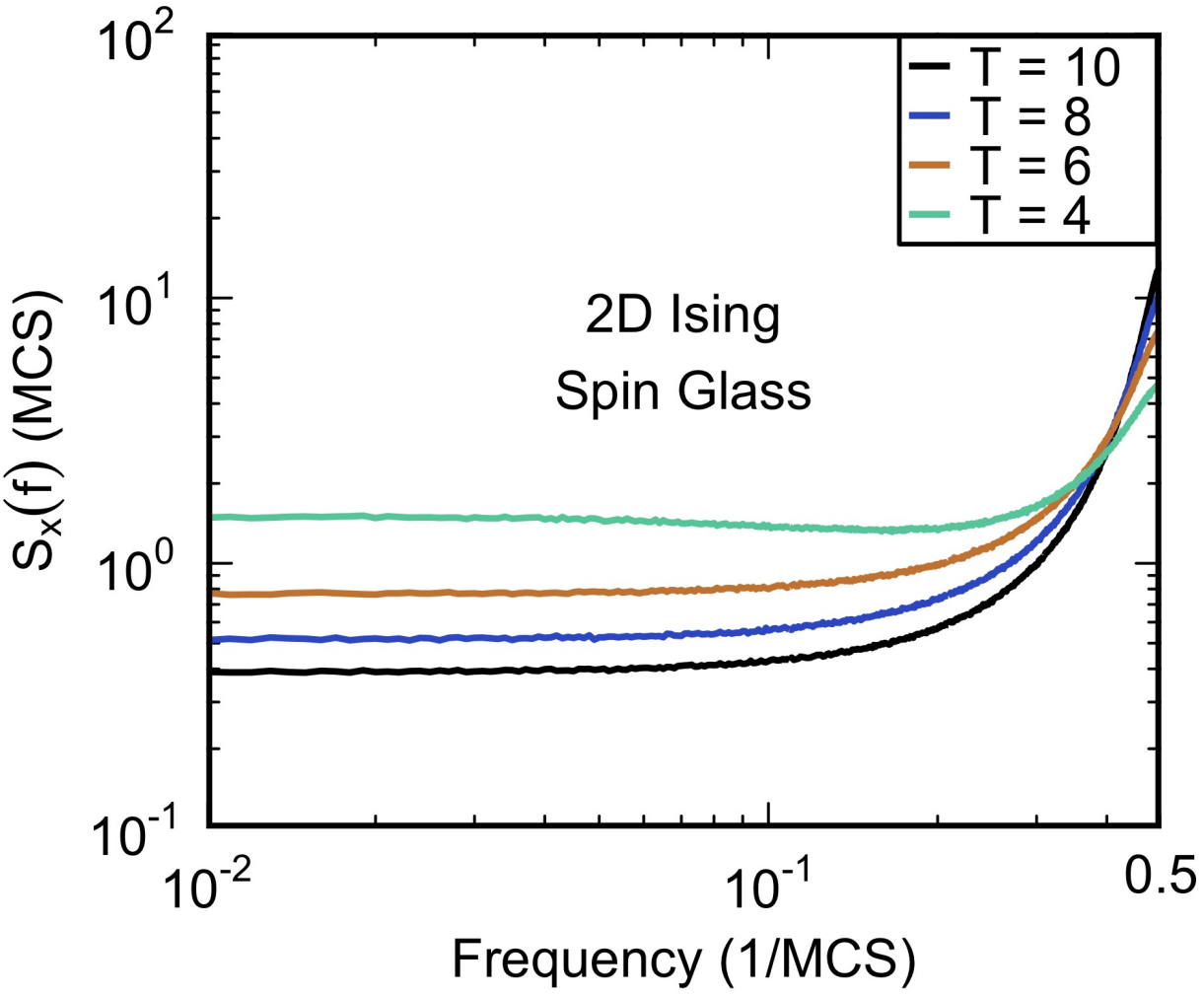

Figure A.2: Noise power $S(f)$ of the total magnetic moment of a 2D Ising spin glass ($\langle J_{ij} \rangle = 0, \sigma_{J_{ij}} = 1$) versus frequency. Spectral pivoting of power spectra averaged over 100 segments for $4 \leq T \leq 10$.

can be described by $\alpha(T) = \alpha_0 \ln(T) + \alpha_1$ [1]. Monte Carlo simulations also find that these relations hold at high temperature. In addition, in both theory and experiment, the crossing frequency f_c as a function of temperature does not change significantly. This can be expressed as

$$\left.\frac{dS(f,T)}{dT}\right|_{f=f_c} = 0. \tag{A.1}$$

Using $S(f,T) = A^2(T)/f^{\alpha(T)}$, we can relate the noise amplitudes to noise exponents:

$$\begin{aligned}
\left.\frac{dS(f,T)}{dT}\right|_{f=f_c} &= \left.\frac{d}{dT}\left(\frac{A^2(T)}{f^{\alpha(T)}}\right)\right|_{f=f_c} \\
&= \left.\left(A^2(T)\frac{d}{dT}\frac{1}{f^{\alpha(T)}} + \frac{1}{f^{\alpha(T)}}\frac{d}{dT}A^2(T)\right)\right|_{f=f_c} \\
&= \left.\left(A^2(T)\left(-\frac{\ln(f)}{f^{\alpha(T)}}\frac{d\alpha(T)}{dT}\right) + \frac{A_0^2}{f^{\alpha(T)}}T^{\gamma-1}\gamma\right)\right|_{f=f_c} \\
&= -S(f_c)\ln(f_c)\frac{\alpha_0}{T} + \frac{S(f_c)}{T}\gamma \\
&= 0.
\end{aligned} \tag{A.2}$$

This gives the crossing condition

$$\gamma = \alpha_0 \ln(f_c). \tag{A.3}$$

Appendix B

Interacting Two-Level Systems as a Source of $1/f$ Noise in Silicon Quantum Dot Qubits

B.1 Equilibration

B.1.1 Equilibration and Recording Times

The Ising spin glass systems are equilibrated for 10^5 MCS at $T = 10$. As the system is cooled, the equilibration and recording times are increased if the system is not in equilibrium. These times as a function of temperature are shown in Table B.1.

Temperature	Equilibration and Recording Times (MCS)
$1 \leq T \leq 10$	10^5
$0.8 \leq T \leq 0.95$	3×10^5
$T = 0.75$	10^6
$0.65 \leq T \leq 0.7$	3×10^6
$T = 0.6$	10^7

Table B.1: Equilibration and recording times for the 2D (16×16) Ising spin glass with random electric dipole orientations for $0.6 \leq T \leq 10$.

B.1.2 Spin Glass Susceptibility

The test for equilibration follows Bhatt and Young's procedure for the equilibration of Ising spin glasses [67]. Two independent replicas of each system with the same exchange couplings are created and run in parallel. The initial spin configurations for the two replicas are different and random. For the set of spins $\{\mathrm{s}_i\}$ with N lattice sites, the spin autocorrelation function for the replica n, after an equilibration time t_0, is

$$Q^{(n)}(t) = \frac{1}{N} \sum_{i=1}^{N} \mathrm{s}_i^{(n)}(t_0) \cdot \mathrm{s}_i^{(n)}(t_0 + t), \tag{B.1}$$

where the summation is over all lattice sites. The spin glass susceptibility for replica n is calculated as the second moment of this overlap and then averaged over 200 different realizations of bonds and anisotropy axes. This disorder average is denoted by $[\ldots]_{\mathrm{av}}$:

$$\chi_{\mathrm{SG}}^{(n)}(t) = \frac{1}{N} \left[\left(\sum_{i=1}^{N} \mathrm{s}_i^{(n)}(t_0) \cdot \mathrm{s}_i^{(n)}(t_0 + t) \right)^2 \right]_{\mathrm{av}}. \tag{B.2}$$

The equilibration time t_0 is chosen from the sequence $1, 3, 10, 30, 100, 300, \ldots$, etc. The idea is to compare $\mathrm{s}_i^{(n)}(t_0)$ to $\mathrm{s}_i^{(n)}(t_0+t)$ as $t \to \infty$ to see whether $\mathrm{s}_i^{(n)}(t_0+t)$ has lost its "memory" of $\mathrm{s}_i^{(n)}(t_0)$. In practice, the comparison is done as $t \to 2t_0$. The spin glass susceptibility in

Eq. (B.2) is averaged over a length of time t_0:

$$\chi_{\rm SG}^{(n)} = \frac{1}{Nt_0}\left[\sum_{t=t_0}^{2t_0-1}\left(\sum_{i=1}^{N} \mathrm{s}_i^{(n)}(t_0)\cdot \mathrm{s}_i^{(n)}(t_0+t)\right)^2\right]_{\rm av}. \tag{B.3}$$

The summation over t starts at t_0 so that the distribution of $Q^n(t)$ is Gaussian. The correlation of the spins at shorter times makes the distribution deviate from a Gaussian. For small values of t_0 and when the system is at low temperatures, there are few spin fluctuations, so $Q^{(n)}(t) \sim 1$ and $\chi_{\rm SG}^{(n)}(t) \sim N$. This is in agreement with simulations.

We can also calculate $\chi_{\rm SG}^{(n)}$ in the high-temperature limit. We start with two Ising spins s_1 and s_2 that represent $\mathrm{s}_i^{(n)}(t_0)$ and $\mathrm{s}_i^{(n)}(t_0+t)$, respectively, in Eq. (B.3). The average square of the dot product is calculated as

$$\begin{aligned}\langle(\mathrm{s}_1\cdot\mathrm{s}_2)^2\rangle_{\rm Ising} &= \langle(\pm s_1 s_2)^2\rangle \\ &= \langle s_1^2 s_2^2\rangle \\ &= 1.\end{aligned} \tag{B.4}$$

Combining Eq. (B.4) with Eq. (B.3), for high temperatures, we get $\chi_{\rm SG}^{(n)} = 1$ which is seen in simulations. We then define the average of the two single replica susceptibilities

$$\overline{\chi}_{\rm SG} = \frac{1}{2}\left(\chi_{\rm SG}^{(1)} + \chi_{\rm SG}^{(2)}\right) \tag{B.5}$$

as the two times spin glass susceptibility.

The spin glass susceptibility may also be calculated from the spin overlap of the two different replicas. The mutual overlap between the spins $\mathrm{s}_i^{(1)}$ and $\mathrm{s}_i^{(2)}$ of the two replicas is

$$Q(t) = \frac{1}{N}\sum_{i=1}^{N} \mathrm{s}_i^{(1)}(t_0+t)\cdot \mathrm{s}_i^{(2)}(t_0+t). \tag{B.6}$$

The spin glass susceptibility is calculated from the spin overlap:

$$\chi_{\mathrm{SG}} = \frac{1}{Nt_0}\left[\sum_{t=t_0}^{2t_0-1}\left(\sum_{i=1}^{N} \mathrm{s}_i^{(1)}(t_0+t)\cdot \mathrm{s}_i^{(2)}(t_0+t)\right)^2\right]_{\mathrm{av}}. \tag{B.7}$$

For all temperatures, as the equilibration time is approached, the spin glass susceptibilities converge; the two times susceptibility $\overline{\chi}_{\mathrm{SG}}$ (Eq. (B.5)) approaches the true susceptibility from above and the replica susceptibility χ_{SG} (Eq. (B.7)) from below. This is shown in Fig. B.1 for the Ising spin glass at $T = 2$.

After sufficiently long equilibration times, χ_{SG} and $\overline{\chi}_{\mathrm{SG}}$ agree. We define the system to be equilibrated if

$$\Delta\chi_{SG} = \frac{|\chi_{\mathrm{SG}} - \overline{\chi}_{\mathrm{SG}}|}{\frac{1}{2}\left(\chi_{\mathrm{SG}} + \overline{\chi}_{\mathrm{SG}}\right)} \tag{B.8}$$

is less than 5% for three consecutive times in the t_0 sequence; then we declare it equilibrated at the fourth time. For example, if the last three equilibration times are $t_1 = 3\times10^3$, $t_2 = 10^4$, $t_3 = 3\times10^4$, then the equilibration time $t_4 = 10^5$. At each temperature, the initial equilibration time is 10^5 MCS, and it is increased if the system is not equilibrated.

B.1.3 Specific Heat and Susceptibility

As a check of this equilibration method, we calculate the block-averaged specific heat and magnetic susceptibility in a similar method to Yu and Carruzzo [69]. We use the form of specific heat

$$\begin{aligned} C_V &= \frac{1}{k_B T^2}\left(\langle E^2\rangle - \langle E\rangle^2\right) \\ &= \frac{N_{\mathrm{sites}}^2}{k_B T^2}\left(\langle e^2\rangle - \langle e\rangle^2\right), \end{aligned} \tag{B.9}$$

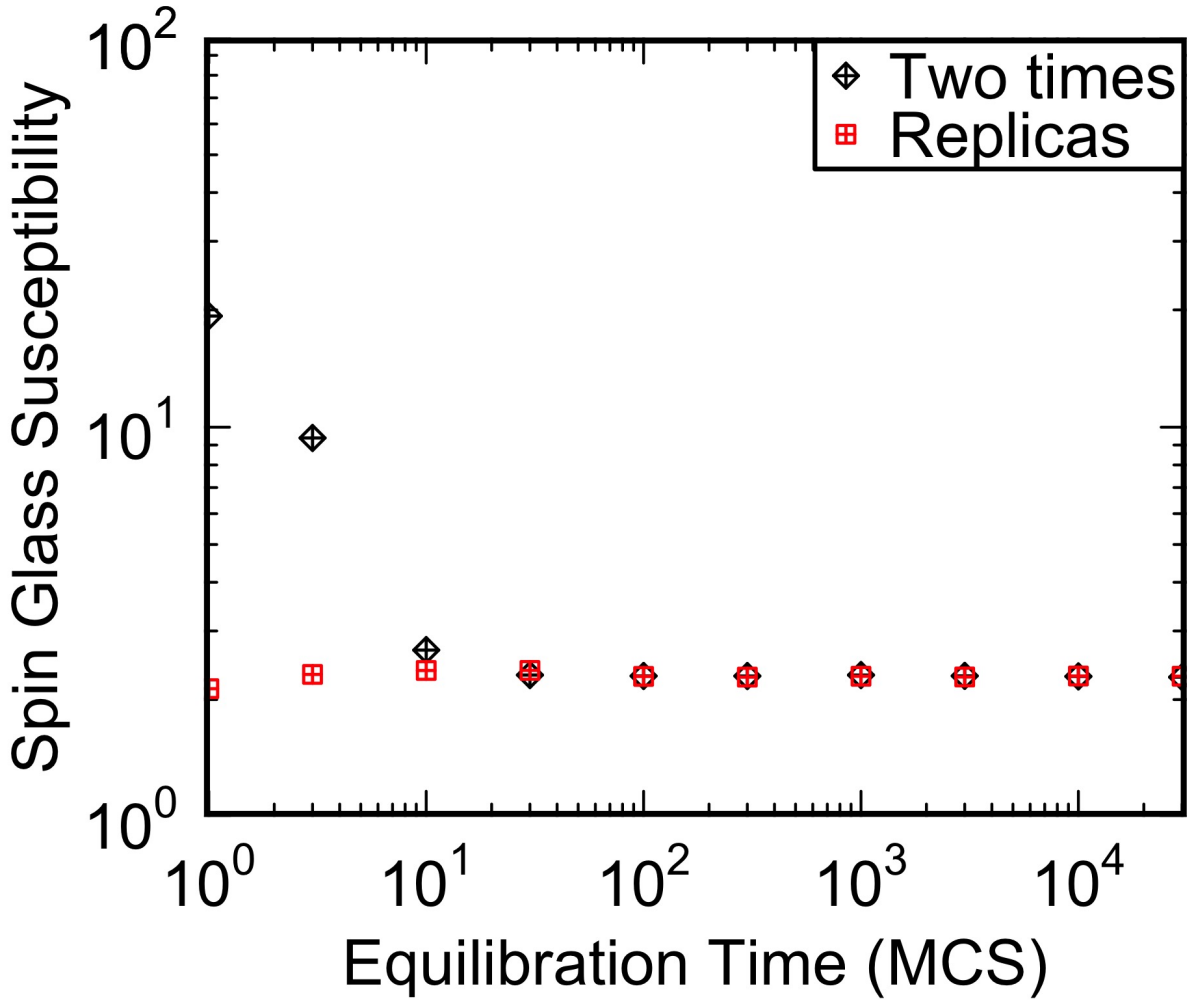

Figure B.1: Two times and replica susceptibility for the 2D (16×16) Ising spin glass for $T = 2$ averaged over 200 runs. For sufficiently long equilibration times, the two susceptibilities agree, and the system is in equilibrium.

where $k_B = 1$, T is temperature, E is the total energy of the lattice, N_{sites} is the total number of sites, and e is the total energy of the lattice divided by the number of sites. In a similar form, we have the magnetic susceptibility

$$\begin{aligned} \chi &= \frac{1}{k_B T} \left(\langle M^2 \rangle - \langle M \rangle^2 \right) \\ &= \frac{N_{\text{sites}}^2}{k_B T} \left(\langle m^2 \rangle - \langle m \rangle^2 \right), \end{aligned} \tag{B.10}$$

where $k_B = 1$, T is temperature, M is the total magnetization of the lattice, N_{sites} is the total number of sites, and m is the total magnetization of the lattice divided by the number of sites.

To calculate the block-averaged specific heat, the energy time series of the system is divided into equally-sized blocks. The specific heat is calculated for each block using Eq. (B.9), and then the blocks are averaged together. For larger block sizes, the specific heat increases and eventually levels off. The block-averaged specific heat is shown in Fig. B.2. The temperature is in units of the standard deviation of the exchange couplings. In our simulations of the Ising spin glass, $\sigma_J = 1$.

To calculate the block-averaged magnetic susceptibility, we follow a similar procedure, but we use Eq. (B.10) with the magnetization time series. The block-averaged magnetic susceptibility is shown in Fig. B.3.

We can see qualitatively that the results of Figs. B.2 and B.3 are consistent with the spin glass equilibration results of Fig. B.1. They indicate that the system is in equilibrium after $\approx 10^3$ MCS.

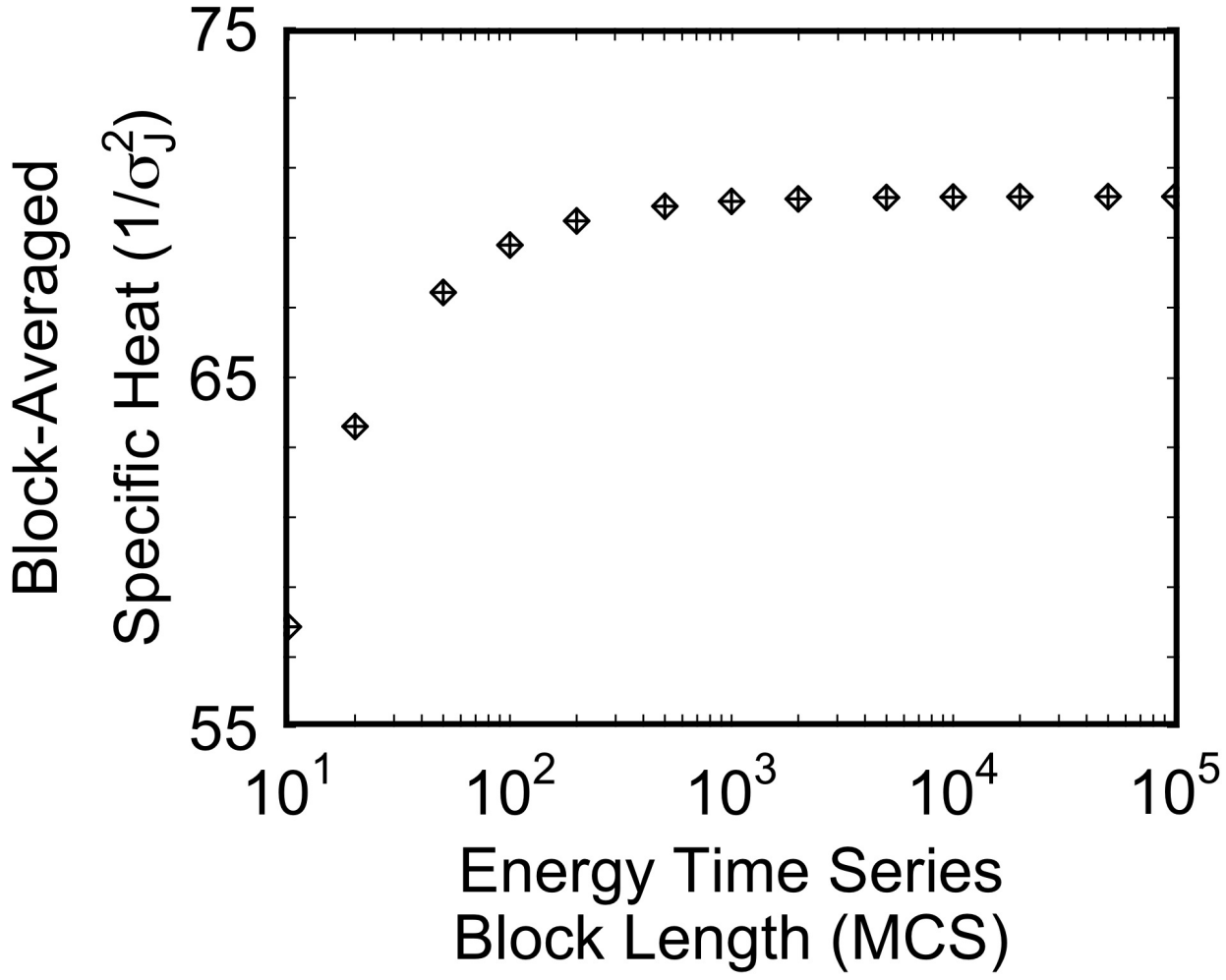

Figure B.2: Block-averaged specific heat versus energy time series block length for the 2D (16×16) Ising spin glass at $T = 2$ averaged over 200 runs. For longer time series, the specific heat approaches a constant value.

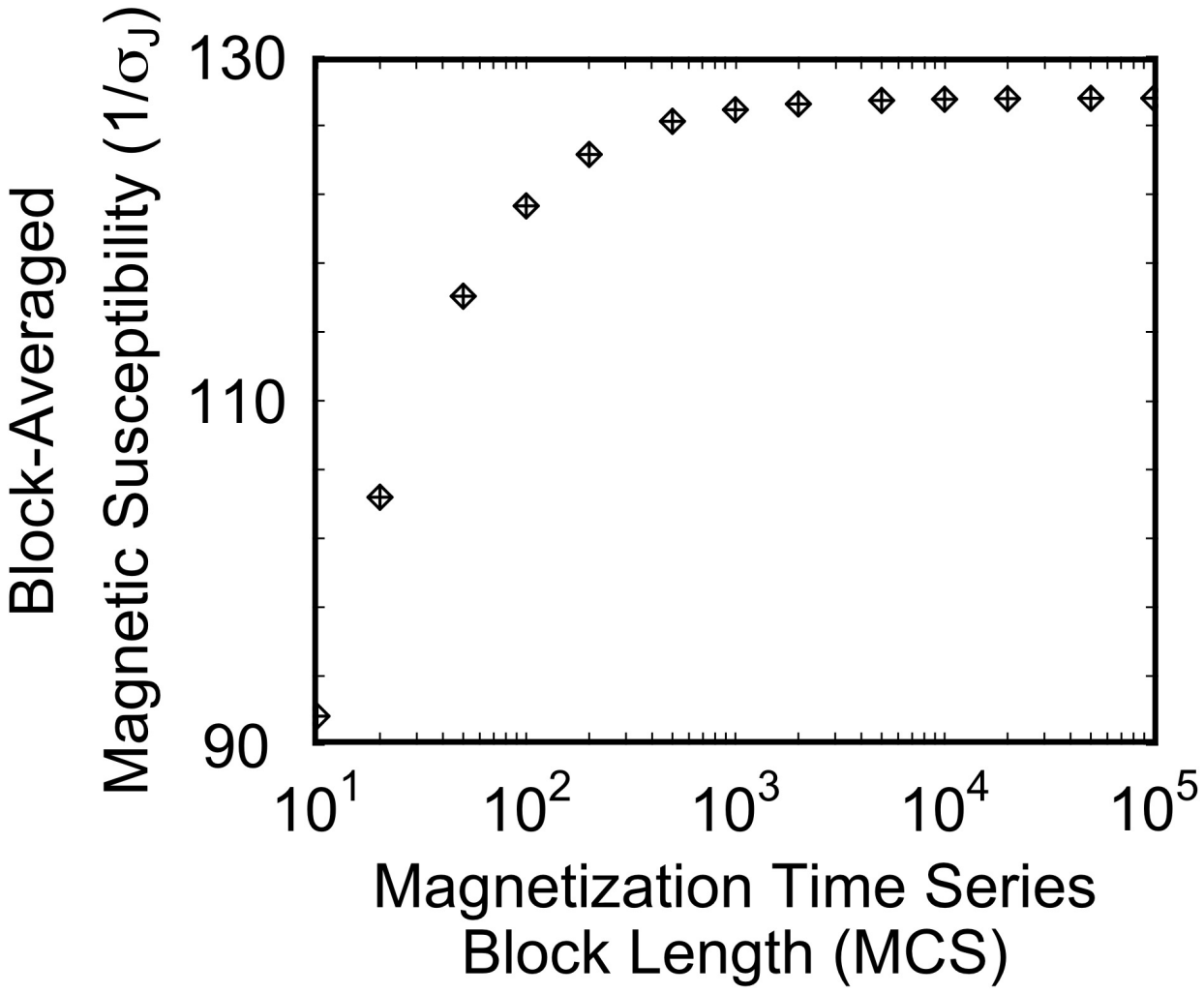

Figure B.3: Block-averaged magnetic susceptibility versus magnetization time series block length for the 2D (16×16) Ising spin glass at $T = 2$ averaged over 200 runs. For longer time series, the magnetic susceptibility approaches a constant value.

B.2 Dipoles aligned along the x, y, or z axes

We perform another 200-run set of Monte Carlo simulations of 2D (16×16) Ising spins. In this case, the electric dipoles lie along the x, y, or z axis. The equilibration times are shown in Table B.2.

Temperature	Equilibration and Recording Times (MCS)
$1.05 \leq T \leq 10$	10^5
$0.85 \leq T \leq 1$	3×10^5
$0.7 \leq T \leq 0.8$	10^6
$0.6 \leq T \leq 0.65$	10^7

Table B.2: Equilibration and recording times for the 2D (16×16) Ising spin glass with dipoles that lie along the x, y, or z axis for $0.6 \leq T \leq 10$.

The noise power as a function of frequency are shown in Fig. B.4 for electric dipoles aligned along the (a) x-axis, (b) y-axis, and (c) z-axis.

$A^2(T)/f^{\alpha(T)}$ is fit to the region of the power spectra that is linear on a log-log plot. The noise amplitudes ($A^2(T)$) and exponents ($\alpha(T)$) are shown in Fig. B.5 (a) and (b), respectively. The dipole correlations are calculated for each axis using Eq. (4.16), and they are shown in Fig. B.5 (c).

The frequency-dependent correlation and phase for the fixed-axis dipoles are calculated using Eq. (4.17). The correlation and phase are shown in Fig. 4.7. For y-axis dipoles, the factor $\vec{p}_{\eta,i}(t) \cdot \hat{R}_\eta$ from Eq. (4.10) is small for fluctuators close to the line connecting the two quantum dots. $\vec{p}_{\eta,i}(t) \cdot \hat{R}_\eta = 0$ for y-axis dipoles along this line. From this, we would expect the correlation strength to be smallest for y-axis dipoles, and this is seen in Fig. 4.7(a). As seen in Fig. 4.7(b), the dipole potentials at quantum dots 1 and 2 for x-axis dipoles are π radians out of phase. Since the quantum dots lie along the x-axis, any fluctuations in x-axis dipoles between the quantum dots will have the opposite effect on each dot.

The image dipoles are aligned for the component along the z-axis and antialigned for the

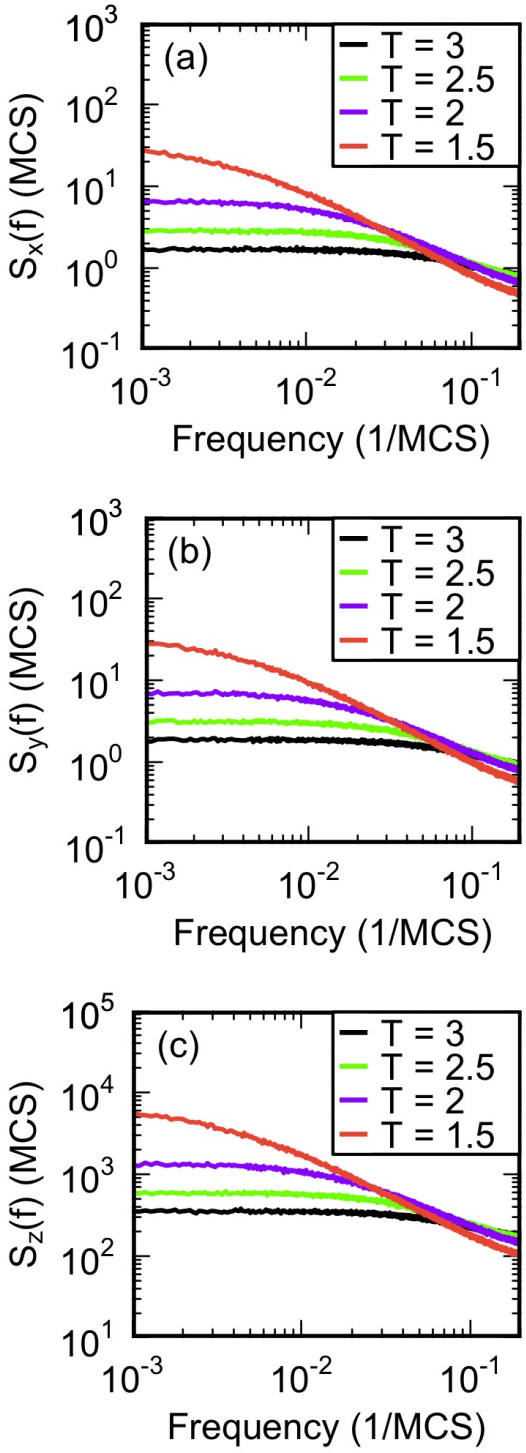

Figure B.4: 200-run average of the noise power versus frequency for the subcases of dipoles that lie along the (a) x-axis, (b) y-axis, and (c) z-axis.

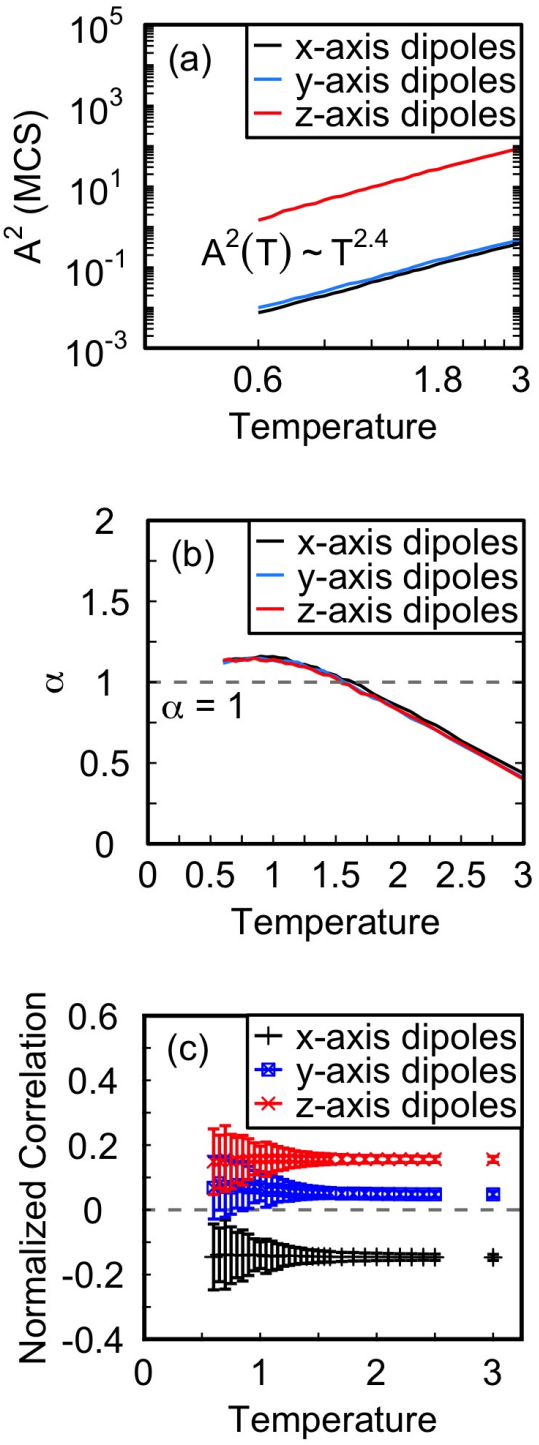

Figure B.5: The (a) noise amplitudes ($A^2(T)$) and (b) noise exponents ($\alpha(T)$) are calculated from fits to the noise power. (c) Dipole correlations for the x-axis, y-axis, and z-axis dipoles.

components along the x and y axes, so we expect the dipole potential calculated from the z-axis component to be the most significant. For the electric dipoles with random orientations, the results should be similar to the case of dipoles aligned along the z-axis. This is certainly true for the dipole correlations and the noise exponents. However, the noise power and noise amplitudes resulting from electric dipoles aligned along the z-axis are three times larger. This is expected, since the z-axis dipoles have unit length, but the z components of the randomly-oriented dipoles have a typical length of $1/\sqrt{3}$. This corresponds to a factor of $1/\sqrt{3}^2 = 1/3$ that reduces the noise amplitude.